Investigation of E-ring interaction with Saturn's Inner Magnetosphere, from the Langmuir Probe observations

Mikael Lundberg

Swedish Institute of Space Physics, Uppsala

September 29, 2007

Abstract

This thesis report deals with the investigation of dust–plasma interaction in Saturn's E-ring. This is done by using data from the Cassini spacecraft.

From previous findings, where there were seemingly *two* ion populations – apparently from the same ion species – moving at different azimuthal speeds around the planet, came the hypothesis of dust–plasma interaction.

This report gives further substance to the claim for the existence of an interaction between the negatively charged dust grains in the E-ring and positively charged ions of mainly hydrogen and water in the surrounding plasma. It also estimates how large a part of the total ion population is being coupled with the dust and in effect is reduced in azimuthal speed around the planet.

Furthermore, a look at certain orbits of interest – among them including flybys of icy moons in the region – revealed significant increases in dust–plasma interaction during the flyby of a moon. The same effect could also be seen in the *trail* left behind along the orbit of the icy moons, suggesting narrow regions of high dust content formed by particles from passing moons.

This study was conducted by analysing data given by the Langmuir probe on board Cassini, and focusing on the ion side part of the current from the voltage sweeps. From the total ion current, I_i, a model for photoelectrons as a function of spacecraft attitude was obtained, in order to deduce an accurate estimation of the ion speed, v_i. Using this, the fraction of the total number of ions which had been coupled to dust, n_dust, was calculated within the E-ring.

In correlation with v_i, n_dust was plotted, showing a clear increase at distances ≤ 5 $\mathrm{R_S}$, with additional increases during flybys of icy moons, as well as in the trail of the moons around their orbital distances. This effect was clearly seen near Enceladus – a moon well known to spew out massive amounts of ice particles into the E-ring – but, most surprisingly, could also be found near Tethys and Dione!

The results of this thesis confirm that two ion populations – one hotter and one colder – are consistent with the Langmuir probe data in the inner magnetosphere of Saturn. The results also show that dust–plasma interaction is indeed taking place in the E-ring. A ratio, n_dust, of 20 % or more is commonly found in the inner magnetosphere, and around the orbits of the icy moons it can be as high as 50 % to 100 % (which is mindboggling)!

It is very likely that several of the icy moons are feeding the E-ring with icy dust particles, which then become charged and interact with the surrounding plasma. While Enceladus most certainly is a major source, it is probably not the *only* source of particles for the E-ring. From the results presented here it is shown that the contribution from the moons leads to an increase in dust–plasma coupling, which is unrelated to the coupling already present in the inner part of the ring and magnetosphere.

Sammanfattning

Det här examensarbetet handlar om undersökningen av växelverkan mellan plasma och stoft i Saturnus E-ring. Detta görs genom att använda data från rymdfarkosten Cassini.

Från tidigare upptäckter, där det tycktes finnas *två* jonpopulationer – till synes av samma jontyp – som rörde sig med olika azimutala farter runt planeten, kom hypotesen om växelverkan mellan plasma och stoft.

Denna rapport ger ytterligare substans till påståendet att det existerar en växelverkan mellan negativt laddade stoftkorn i E-ringen och positivt laddade joner av främst väte och vatten i det omgivande plasmat. Det uppskattar också hur stor del av den totala jonpopulationen som är kopplad till stoftet och i realiteten reduceras i azimutal fart runt planeten.

Dessutom, en studie av vissa intressanta banor – bland dem inkluderade förbiflygningar av isiga månar i regionen – avslöjade signifikanta ökningar i stoft–plasmaväxelverkan under förbiflygningen av en måne. Samma effekt kunde även ses i det *spår* som lämnats kvar längs banan av den isiga månen, antydandes smala regioner av högt stoftinnehåll bildat av partiklar från passerande månar.

Den här undersökningen genomfördes genom att analysera data givna från Langmuirproben ombord på Cassini, fokuserandes på strömmen på jonsidan av spänningssvepen. Från den totala jonströmmen, I_{i}, togs en modell för fotoelektroner som en funktion av rymdfarkostattityd fram, för att härleda en noggrann uppskattning av jonhastigheten, v_{i}. Denna användes till att beräkna den andel av totala mängden joner som var kopplad till stoft, n_{dust}, inom E-ringen.

Tillsammans med v_{i} plottades n_{dust}, påvisandes en klar ökning vid avstånd ≤ 5 $\mathrm{R_S}$, med ytterligare ökningar under förbiflygningar av isiga månar, liksom i spåret från månarna kring deras banavstånd. Denna effekt syntes tydligt nära Enceladus – en måne välkänd för att spy ut massiva mängder av ispartiklar i E-ringen – men, högst förvånansvärt, kunde även hittas nära Tethys och Dione!

Resultaten av detta examensarbete bekräftar att två jonpopulationer – en hetare och en kallare – stämmer överrens med Langmuirprobens data i Saturnus inre magnetosfär. Resultaten visar även att stoft–plasma -växelverkan faktiskt försiggår i E-ringen. Ett förhållande, n_{dust}, på 20 % eller mer är vanligt förekommande i den inre magnetosfären, och kring banorna av de isiga månarna kan det bli så högt som 50 % till 100 % (vilket är häpnadsväckande)!

Det är högst sannolikt att flera av de isiga månarna förser E-ringen med isiga stoftpartiklar, vilka sedan blir laddade och interagerar med det omgivande plasmat. Medan Enceladus utan tvekan är en betydande källa, är den troligen inte den *enda* källan för partiklar till E-ringen. Från resultaten presenterade här är det visat att bidraget från månarna leder till en ökning i stoft–plasmakoppling, vilken är orelaterad till den koppling som redan är närvarande i den inre delen av ringen och magnetosfären.

To Gene Roddenberry; a true visionary, whose hopes and dreams of a better planet and future for all mankind, are things to which we should all strive to achieve. His vision has long since been the greatest inspiration of my life and has – more than anything else – influenced where I am today and, by so doing, made this report possible.

Requiescat in pace, Vir humanitatis!

Contents

1

Introduction

In 1966 the Allegheny Observatory photographs a feature around Saturn which would be called the E-ring, but it is not until 1967 that Walter Feibelman actually discovers the E-ring from the images taken the year before. Later, in 1979, Pioneer 11 flies past Saturn and confirms the existence of the E-ring.

In 1980, William Baum and Stephen Larson observe that the E-ring extends from the orbit of Mimas[1] to, as far as they can tell, end at 8 Saturn radii, near the orbit of Rhea. The peak brightness of the E-ring corresponded with the orbit of Enceladus, and when Voyager 1 flew past the region in 1980 it found that Enceladus orbited in the densest part of the E-ring. Both of these findings indicated a possible association between the E-ring and Enceladus; that this moon was the likely source of particles for the E-ring. This view seemed to be confirmed in the second half of 2004, when the Cassini spacecraft arrived at the Saturnian system and found that Enceladus was spewing out massive amounts of particles into the E-ring, from a region near its south pole. However, that was not to be the final word on the mystery of the E-ring...

This thesis focuses on the investigation of possible interaction between dust and plasma in the E-ring of Saturn. Plasma is simply neutral gas that has been ionised by radiation, and so consists of positively charged ions and free electrons. The dust in the E-ring is composed of tiny ice grains – microscopic particles – that are negatively charged, and thus attracts ions from the surrounding plasma, causing an interaction between dust and plasma. This physical process of dust—plasma coupling was first suggested in 2005 (see [Wahlund et al., 2005]).

This report is divided into several parts. The first few chapters are an introductory part covering important concepts and knowledge that are prerequisite for the following parts, as well as the background that spawned this thesis. The

---

[1] Later determined to be at 3.1 R_S distance (See section 2.4.2).

next couple of chapters deal with the needed theory and models underlying the work.

The following part is the actual work that was carried out in this project; itself split into three parts: the correction of the current for photoelectrons dependent on spacecraft attitude, the calculation of an estimated plasma ion speed, and studying of the dust—plasma interaction as a function of space. The last few chapters are a summary part, with a discussion of results and conclusions, and an outlook on future extensions of this study.

The work done within this project is based on data obtained from the Langmuir probe on board the Cassini spacecraft. The main aims of the project has been to confirm the existence of dust—plasma interaction in Saturn's E-ring and, following that, to estimate the fraction of the total number of ions that are coupled to dust and map this fraction as a function of distance from Saturn; to see *where* this coupling can be found; *what factors* are involved in this coupling; and *how much* interaction there is going on in different regions.

For this project I have analysed, studied and used data from more than 30 orbits of Cassini around Saturn. This data spans a time period from mid 2004 (Rev00) to late 2006 (Rev33), and among other things includes flybys of moons in the Saturnian system; among them 3 flybys of the moon Enceladus in the E-ring, and more than 20 flybys of the moon Titan.

2

The Saturnian System

This chapter is an introduction to the Saturnian system. It covers a brief general overview of Saturn itself, its ring system and moons, as well as Saturn's magnetosphere. Also, a more focused overview of certain concepts and terminology – such as the E-ring and the icy moons therein – are given in more detail, since they are of great relevance for this project and needed in order to understand the rest of this thesis.

Should the reader feel him- or herself confident in the knowledge and understanding of the E-ring, dust and surrounding plasma, feel free to either view this chapter as a refresher and skim through it, or else skip it entirely.

2.1 The Planet Saturn

Saturn is the second largest planet in our solar system (after Jupiter), and is the sixth planet from the Sun. It is a gas giant (a.k.a. Jovian planet, named after Jupiter), meaning it does not have a solid surface like the Earth-like inner planets. Instead, it is more fluid with a small core of rock and ice, surrounded by a thick layer of metallic hydrogen and a gaseous outer layer of primarily hydrogen with small proportions of helium and other trace elements.

Relative to the abundance of the elements in the Sun, the atmosphere of Saturn is significantly deficient in helium. With the abundance of hydrogen being more than 93 % of the atmosphere, this gives rise to the fact that Saturn has an average specific density of 0.69 g/cm^3 – less than the density of water!

Despite having a gaseous atmosphere, Saturn is not a sphere; it is an oblate spheroid. It is flattened at the poles and bulges at the equator. This is a result of its large size but much lower mass than Jupiter combined with low density, a rapid rotation and a fluid state, causing gravitational forces to deform the sphere. At the equator, the radius of Saturn (denoted R_S) is 60 268 km and the rotation period, τ_{rot}, is 10 hours 39 minutes 26 seconds[1].

---

[1] Calculated; consistent with: http://nssdc.gsfc.nasa.gov/planetary/factsheet/saturnfact.html

2.2 Magnetosphere

Like the other Jovian planets – as well as Earth – Saturn is surrounded by a giant magnetic field. In Saturn's case, the internal magnetic field is closely (within 1 degree) lined up with the rotation axis of the planet. The magnetic field is also very uniform; in essence a strong dipole field (resembling the field from a bar magnet) whose field lines stretch out far from the planet. See Figure 2.1.

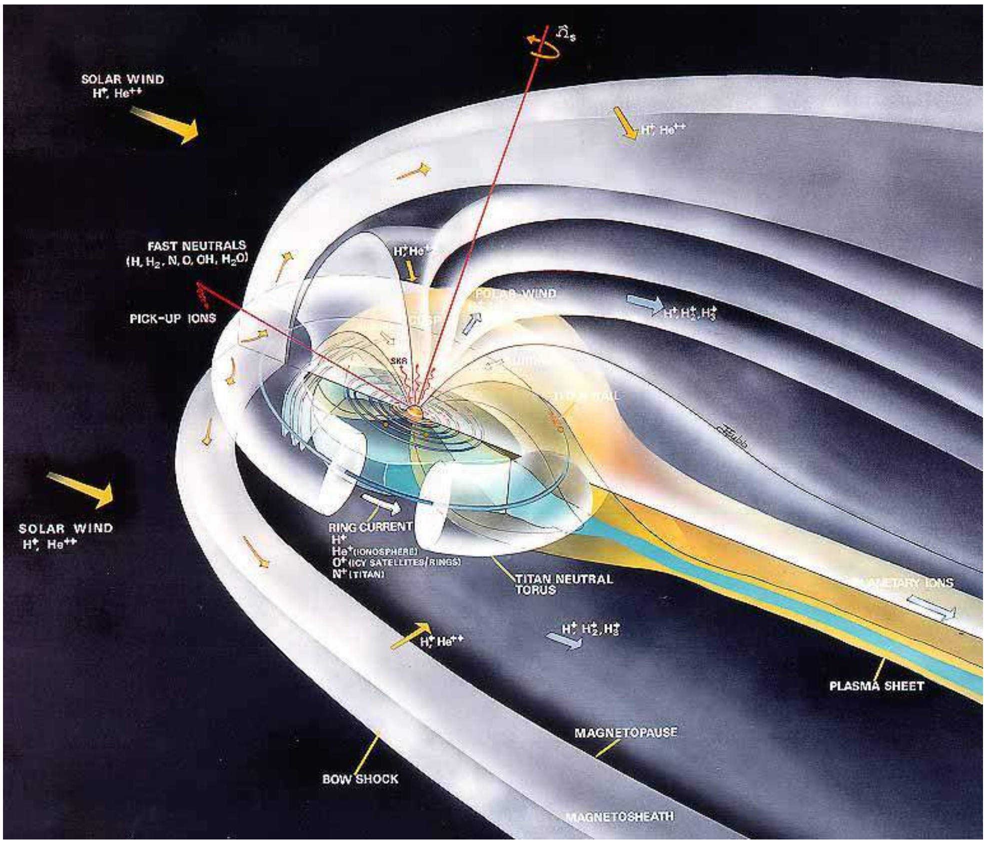

Figure 2.1: A 3-D schematic of Saturn's magnetosphere

Associated with the magnetic field of a planet is something known as a *magnetosphere*. A magnetosphere forms around a body with a magnetic field strong enough to trap *plasma*; i.e. gas that has been ionised by radiation and thus consists of ions and electrons in roughly equal numbers. In essence, this trapping encases a region of plasma within it which separates it from the plasma in the solar wind outside. The separating boundary is known as the *magnetopause*.

Strictly speaking, the magnetosphere is the region in space around an astronomical object in which phenomena are dominated, or organised, by the object's magnetic field. In the magnetosphere, a mix of free ions and electrons from the body's ionosphere as well as moon sources – and also in a small part the solar wind – is confined by magnetic and electric forces that are much stronger than gravity and collisions.

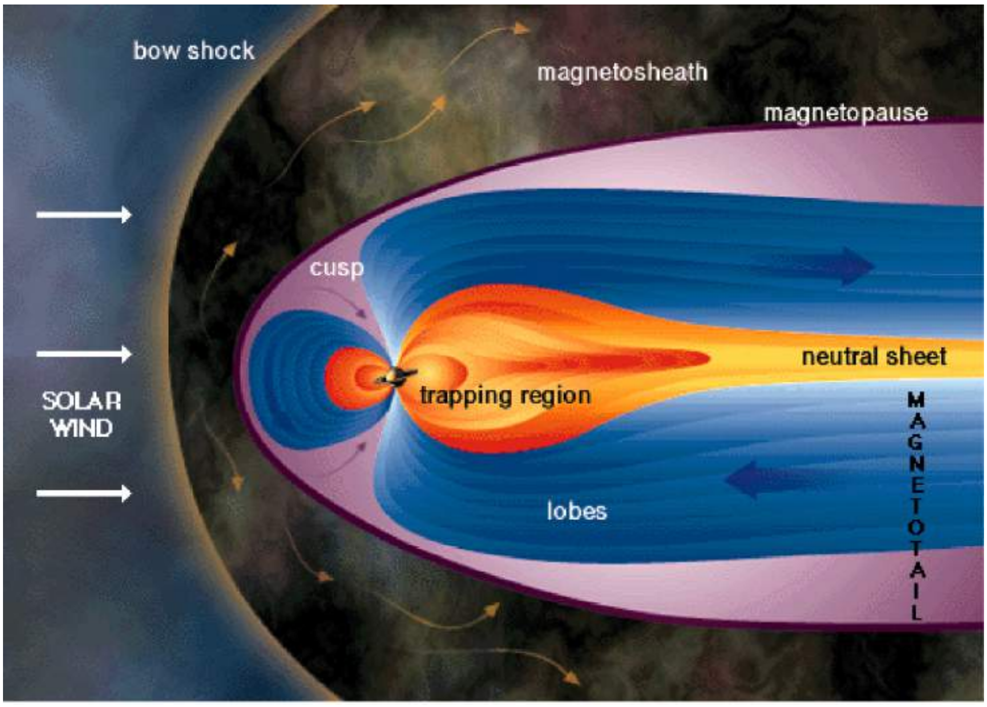

Figure 2.2: A 2-D cross-section of Saturn's magnetosphere. The bow shock is the thin yellowish line, and the magnetopause is the thin deep purple line.

The shape, and size, of the magnetosphere is determined by the extent of the body's internal magnetic field, the solar wind plasma, and the interplanetary magnetic field (IMF)[2]. The solar wind causes the magnetosphere to be compressed on the *dayside* (the side of Saturn facing the Sun), and drawn out on the *nightside* into a very long tail (see Figure 2.2). On the dayside, where the solar wind plasma starts to deviate around Saturn's magnetic field, a so called *bow shock* is formed, some 2000 km thick. In the region between the bow shock and the magnetopause – a region known as the *magnetosheath* – the velocity of the solar wind drops from super-sonic[3] to sub-sonic speeds.

Since Saturn possesses a strong magnetic field – stronger than Earth's but not as strong as the powerful field around Jupiter – the associated magneto-

---

[2] The IMF is the term for the Sun's magnetic field whose lines are frozen-into the solar wind plasma, and carried by the solar wind in a so called *Parker spiral* – a spiral pattern created by the Sun's rotation and the radially outflowing solar wind – among the planets of the solar system.

[3] Meaning faster-than-sound speed.

sphere stretches out far from the planet, and has been measured out to at least 20 R_S (Saturn radii) at the subsolar point[4]. However, this position is strongly influenced by external parameters such as the solar wind pressure. This distance is around the orbit of Saturn's largest moon, Titan, which sometimes causes Titan to be exposed to the solar wind directly, outside the protection of the magnetosphere (this happened during flyby T32).

2.3 The Ring System

Saturn is a planet that is, in many ways, much defined by the ring system around it and the intricate structure of those rings. Most people know that Saturn has rings around it, and although all the other gas giants in our solar system also have ring structures, only around Saturn are they so rich and complex. See Figure 2.3 for a real photo of the ring system.

The ring system is not just one or two rings, but a whole series of planetary rings that orbit Saturn. The rings themselves consist largely of ice and stony material, in the form of particles ranging in size from very tiny to several meters or some even up to a kilometer or over.

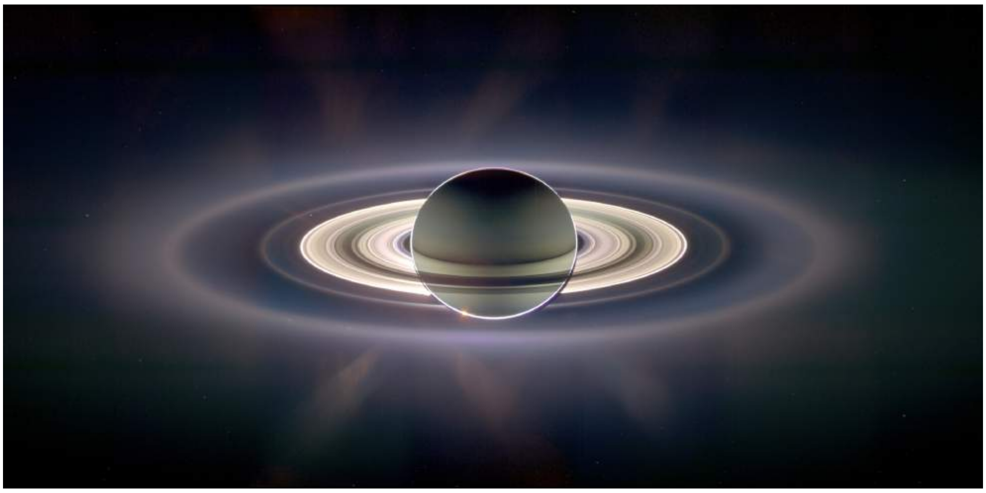

Figure 2.3: The full set of Saturn's rings, taken in eclipse by the Cassini spacecraft. (Note: The brightness in this image has been exaggerated!)

The rings themselves are split into at least seven groupings, labelled A to G in the approximate order they were discovered, and also a few more which have newly been discovered and may not have been properly named as yet. Some of the rings are made up of a number of ringlets; some from just a few ringlets and others to an innumerable amount. Figure 2.5 illustrates an overview of Saturn's ring system.

---

[4] The point of the magnetopause that is closest to the Sun.

There are also several gaps between the rings, as well as divisions within some of the rings. Some of these are caused by orbital resonances between the tiny particles that compose the rings, and one or more of Saturn's moons. What this means is that the particles in a certain region have an orbital period which is an integer ratio with that of one or more of the moons (e.g. 2:3 or 1:4), and because of this there will be a gravitational pull from the moon(s) which will clear one region of particles while contributing to a concentration of ring particles in another region.

Up until 1660, when Jean Chapelain suggested that Saturn's rings were made up of a large number of very small satellites, most people (Giovanni Cassini not among them) believed that Saturn's rings were solid. This suggestion went mostly unnoticed, and it was not until 1856 that James Maxwell deduced that the rings cannot be solid but must be made up of "*an indefinite number of unconnected particles*", or they would otherwise break apart.

2.3.1 Inner Rings

The rings that are considered to belong to this group are the A, B, C and D rings. These make up the bright and the big rings, and are illustrated in Figure 2.4 below.

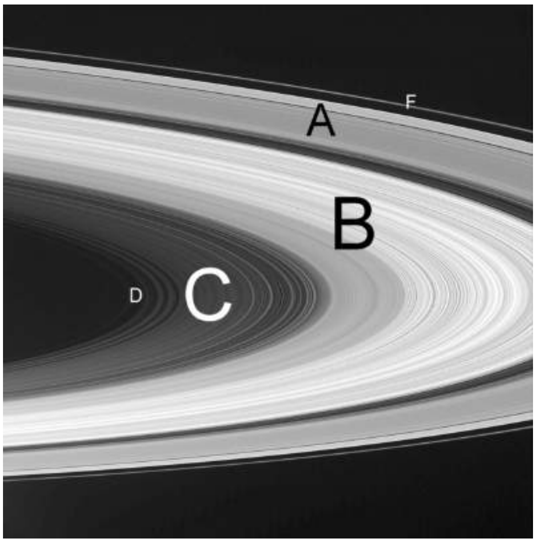

Figure 2.4: A picture of the major rings of Saturn, taken by the Cassini spacecraft.

The D ring is the innermost ring of Saturn, located inward of the C ring and is extremely faint. The C ring is a fairly wide ring located between the D and B rings. Although it is brighter than the D ring, it is still very faint, composed of much darker material than the brighter A and B rings.

In the middle of the C ring lies the Colombo Gap which contains the narrow and bright Titan Ringlet; an eccentric ringlet, whose name comes from it being in a resonance with the moon Titan. Within the C ring, one can also find the Maxwell gap.

Out of the two largest, brightest rings, the B ring is the innermost one and actually the first ring discovered. At that time, however, the A and B rings were believed to be one and the same. The B ring, unlike the A ring, is made up of innumerable ringlets. It also has spoke features in it, which have become quite famous for still being unexplained.

In 1675, the Cassini Division between the A and B rings was discovered, which appears as a thin black gap. The Voyager flybys in 1980 and 1981 discovered that the gap is actually full of tiny rings. There is also the Huygens Gap, which separates the B ring from the Cassini Division.

The A ring is the outermost of the two largest and brightest rings, and has the Cassini Division as its inner boundary. Within the ring both the Encke Division formed by the moon Pan orbiting within it, and the Keeler Gap formed by the moon Daphnis orbiting within it, are found.

All of the inner rings are very flat. Their thickness only varies between 5 and 30 meters[5].

2.3.2 Outer Rings

The F, G and E rings, as well as two rings created by particles blasted off the surface of moons – the "Janus/Epimetheus" ring and the "Pallene" ring – are counted among the group of outer rings.

The F ring is very thin and located just outside the larger, inner rings (see Figure 2.4). It is held together by two shepherd moons, Prometheus and Pandora, which orbit just inside and outside it, respectively.

The "Janus/Epimetheus" ring is a faint dust ring occupied by the orbits of the moons Janus and Epimetheus. It is formed by particles blasted off the surfaces of the moons by meteoroid impacts.

The G ring is very thin and faint, located about halfway between the F ring and the beginning of the E ring. Being some 5000 km wide and on the order of 100 km thick, the G ring is more like a torus than a ring.

Between the G and E rings, the "Pallene" ring is found. It is a faint dust ring which shares the orbit of the moon Pallene, and also formed by surface particles from the moon.

2.3.3 The E-ring

The outermost ring of Saturn is the E-ring, and this ring is the region of focus for this entire thesis. It is by far the widest ring, stretching from a distance

---

[5] See http://nssdc.gsfc.nasa.gov/planetary/factsheet/satringfact.html (Saturnian Rings Fact Sheet @ NASA, 20070713)

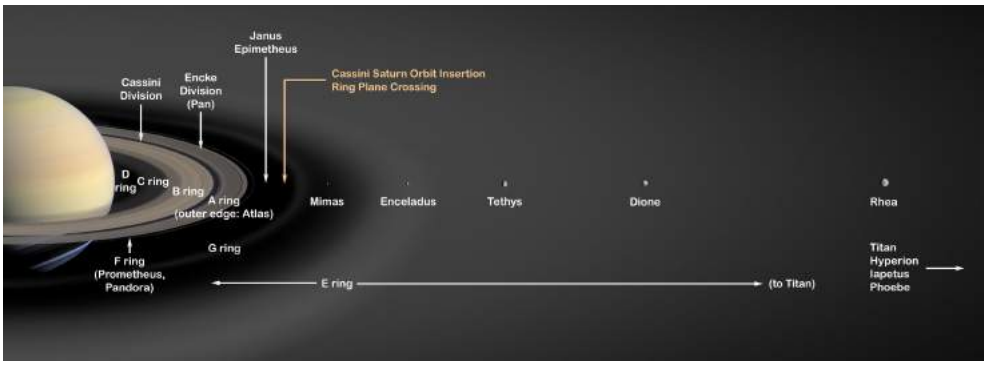

Figure 2.5: An illustration of the ring system of Saturn and the large moons within.

of 3 R$_S$, just before the orbit of the moon Mimas, and ending somewhere at a distance of 8-10 R$_S$. The E-ring is a diffuse disk of icy or dusty material and, unlike any of the other rings around Saturn, it is composed of *microscopic* rather than macroscopic particles. The source of the micron-sized ice grains in the ring are (some of) the moons within it.

Where the actual outer limit of this ring should be drawn is still being debated. However, most agree that the moon Rhea – which is located at a distance of 8.7 R$_S$ – should be included in the E-ring.

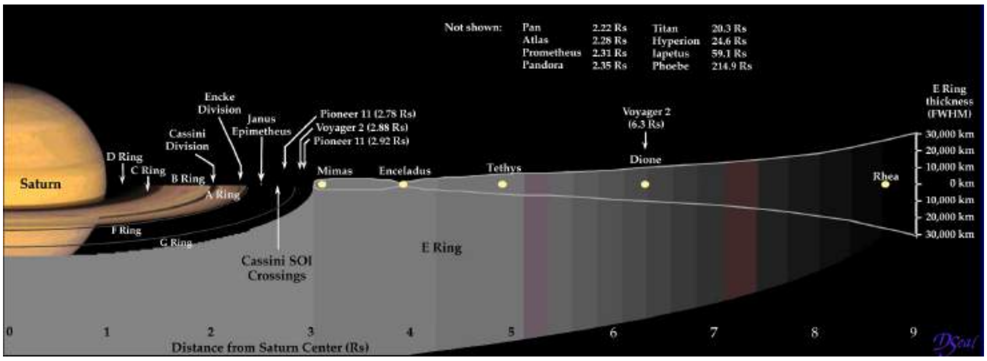

Figure 2.6: Illustration of Saturn's rings and moons, with the thickness of the E ring included.

As can be seen in Figure 2.6, the E-ring increases in thickness further out, and although it then becomes more diffuse and difficult to observe, it does not end at 8 R$_S$.

For the scope of this thesis and the work done within, the E-ring has been defined as the region between 3 R$_S$ and 10 R$_S$ radial distance from the center of Saturn, in the equatorial plane.

2.4 Moons of Saturn

Like all the other outer planets, Saturn has moons – a lot of them in fact. Exactly how many moons Saturn actually has is uncertain, because it is not (really) possible to give a precise number. Once again this is due to the fact that Saturn has such an elaborate ring system.

It can be argued that every particle orbiting a planet is a moon, and since Saturn's rings are made up of particles, technically *all* the ice chunks and rocks in the rings are moons of Saturn. There is no objective dividing line between the anonymous orbiting fragments that form the ring system and larger objects that have already been named as moons, so it is very difficult to draw a distinction between what is a large ring particle and what is a tiny moon. Saturn is currently thought to have 62 *natural satellites*[6]. A total of 59 individual moons have been identified, out of which 48 have been confirmed as well as named. The remaining 14 objects are all very recent discoveries (2004 or later); 3 of which are particularly unconfirmed hypothetical moons around the F-ring[7], and are especially doubtful!

Out of all Saturn's moons, only seven are massive enough to have collapsed into spheroids under their own gravitation. These are: Mimas, Enceladus, Tethys, Dione, Rhea, Titan and Iapetus. These seven moons – as well as Hyperion, a very irregular moon with a chaotic rotation – were all discovered by direct observations using an optical telescope, between the years 1655 and 1848.

2.4.1 Titan

Although Titan is not directly included within the scope of this thesis, it is still one of the primary objectives of study for the Cassini mission, and deserves special mention for other reasons as well.

Titan is Saturn's largest moon by far; being the second largest moon in our entire solar system, only very slightly smaller than Jupiter's moon Ganymede, and larger than the planet Mercury. It is one of the most interesting objects in the solar system because Titan possesses a thick atmosphere, which is even denser than the atmosphere of Earth.

Titan is one of few moons in our solar system with a significant atmosphere[8], and is the one with the most dense atmosphere of them all. The thick orange haze that makes up Titan's atmosphere is impenetrable in the visual spectrum (see Figure 2.7), which prevented understanding of the surface prior to the arrival of the Cassini-Huygens mission.

---

[6] A natural satellite is the term used for an object that orbits a celestial body (for example a planet, a moon or a star) larger than itself, and which is *not* man-made. The most common usage of the term is to describe a moon of a planet.

[7] These are: S/2004 S3, S/2004 S4 and S/2004 S6. See [Spitale et al., 2006]

[8] Other moons include Io and Triton, and depending on the definition of 'significant' could also include such moons as Ganymede, Callisto as well as Europa.

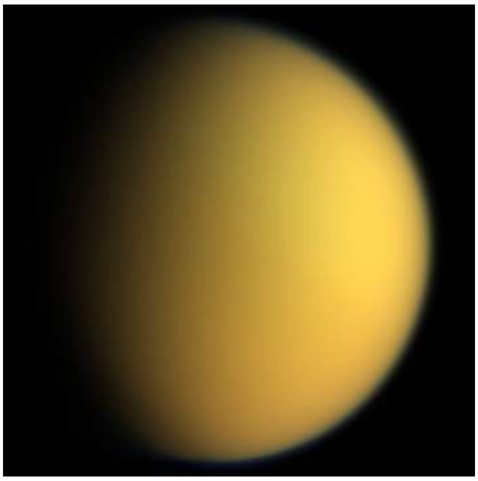

Figure 2.7: A natural color composite of Titan taken by the Cassini spacecraft during a flyby of the moon in April 2005. The image shows approximately what Titan would look like to the human eye.
Credit: NASA/JPL/Space Science Institute

Titan orbits Saturn at approximately 20 R_S distance from the center of Saturn. This is close to Saturn's magnetopause, which means that sometimes Titan is outside the magnetosphere of Saturn; its atmosphere exposed to the solar wind. For the interested reader wanting to know more about Titan, see [Westerberg, 2007].

2.4.2 Icy Moons in the E-ring

With the E-ring herein being defined as stretching between 3 R_S and 10 R_S distance (from the center of Saturn), this region contains five large moons: Mimas, Enceladus, Tethys, Dione and Rhea. They are all icy moons and, as previously mentioned, have the approximate shape of a spheroid.

Mimas

Mimas was discovered in 1789 by William Herschel. It is located at a distance of 3.1 R_S and has an average diameter of 397 km. The average density of Mimas is 1.17 g/cm^3, which indicates that it is composed mostly of water ice with only a small amount of rock. There are tidal forces acting on Mimas, causing it not to be perfectly spherical but more egg-shaped.

The most distinctive feature of Mimas is a huge impact crater named Herschel. It spans 130 km across, which is nearly a third of the total diameter of the moon. The force of the impact that formed the crater Herschel must have nearly shattered Mimas: on the opposite side, fractures can be seen which may

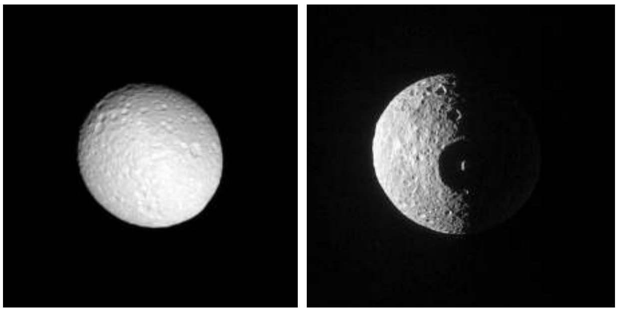

Figure 2.8: Both these images were taken by the Cassini spacecraft.
To the left is a tilted look at Mimas which highlights the many deep craters on the icy moon's trailing side. North on Mimas is here directed up and tilted 44 degrees to the right. Also, the ovoid shape of Mimas is here clearly visible.
To the right is a dead-on look at the crater Herschel with its prominent central peak. The view is predominantly of the leading hemisphere of Mimas, and the image has been rotated so that North on Mimas is pointing upward.
Credit: NASA/JPL/Space Science Institute

have been created by shock waves travelling through the body of the moon. A look at Mimas can be seen in Figure 2.8.

Enceladus

Enceladus was also discovered in 1789 by William Herschel. It is located at a distance of 4.0 R_S and its average diameter is 504 km. The surface of Enceladus is covered in water ice, which reflects almost 100 % of the sunlight striking it. Despite Enceladus' small size, the surface reveals a wide range of different terrains; from old, heavily cratered surfaces to young, tectonically deformed terrain – some regions as young as 100 million years. See Figure 2.9.

Previously it was thought that Enceladus was composed entirely of water ice. However, measurements by the Cassini spacecraft has yielded a density of 1.61 g/cm^3 – higher that the other mid-sized icy satellites of Saturn and much higher than previously thought for Enceladus. This indicates that Enceladus contains a greater percentage of silicates and iron in an inner rocky core, and an outer mantle rich in water ice.

Close flybys of Enceladus made by Cassini in 2005 discovered a water-rich plume (see Figure 2.10), venting particles of water ice and neutral gas from regions near the south pole of Enceladus out into the E-ring, at a rate of 1 metric ton per second! This shows that Enceladus has been for quite some time, and is still today, geologically active; Enceladus being one of only four bodies in our solar system where active eruptions have been observed – the others being Earth, Jupiter's moon Io and Neptune's moon Triton.

One of the main theories to explain the *cryovolcanism* – plumes venting

Figure 2.9: Unprocessed image of Enceladus, taken by the Cassini spacecraft during the close approach of the flyby on July 14, 2005 (Rev11).
In the bottom right of the image, in the south polar region of Enceladus, one can see 4 sub-parallel linear depressions, flanked on each side by low ridges and having a central fracture. These four features are unofficially known as "tiger stripes".
Credit: NASA/JPL/Space Science Institute

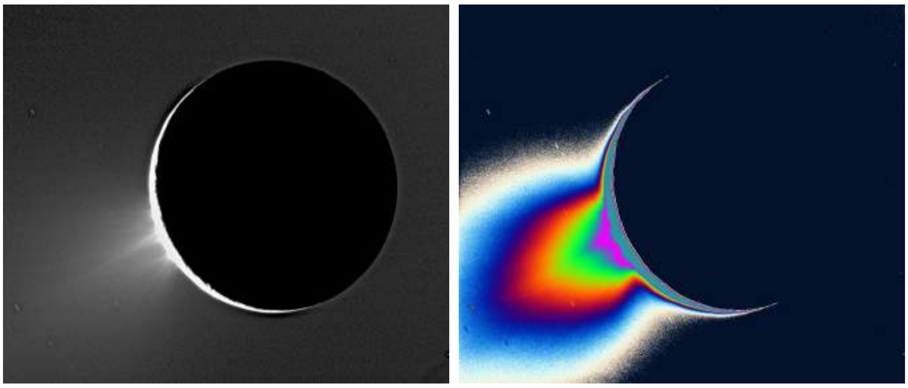

Figure 2.10: A view of the south polar plume of Enceladus, seen from Cassini. Shown to the left is the fine spray of materials coming from the fountain-like sources - such as the "tiger stripe" fractures - in the south polar region. This image shows both discrete and small-scale plumes.
To the right is a colour-coded image that has been processed to enhance faint signals. This makes contours in the plume of material even more apparent, as well as showing the enormous extent of the fainter, larger-scale component of the plume.
Credit: NASA/JPL/Space Science Institute

water, ice and other volatiles instead of silicate rock – from the south pole of Enceladus, is the so called *cold geyser model* (see Figure 2.11). In this model, the plumes emanate from pressurised sub-surface chambers – similar to geysers on Earth – in which liquid water is trapped in a pocket.

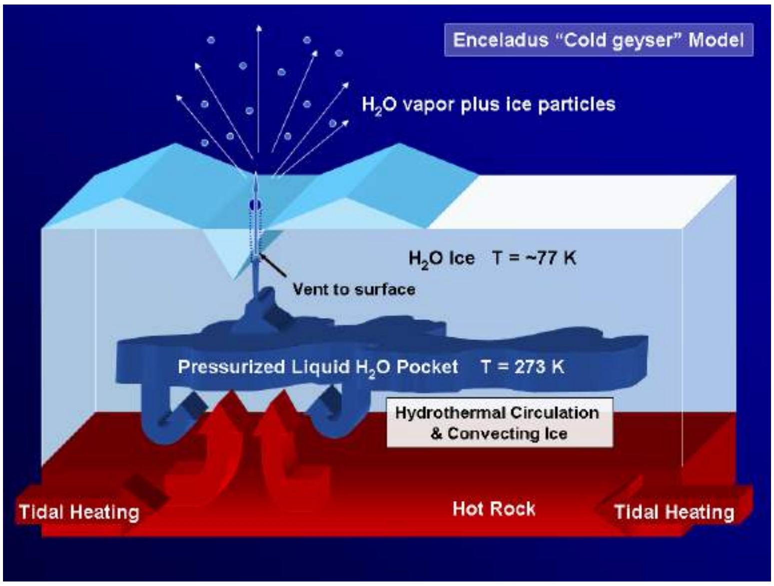

Figure 2.11: An illustration showing the cold geyser model for Enceladus; one possible explanation for the moon's cryovolcanism.

Other theories to explain the cryovolcanism include the *ice sublimation hypothesis* found in Spencer et al. [2006], and the *clathrate reservoir hypothesis* found in Kieffer et al. [2006].

Enceladus is currently in a 2:1 mean motion orbital resonance with Dione, meaning Enceladus completes two orbits around Saturn for every one orbit completed by Dione. Moons in the extensive satellite system of gas giants like Saturn often become trapped in orbital resonances that lead to forced libration or orbital eccentricity – in the case of Enceladus, it helps maintain an orbital eccentricity of 0.0047. Proximity to the planet can then lead to tidal heating of the satellite's interior; providing a heat source which offers a possible explanation for the geological activity of Enceladus.

Tethys

Tethys was discovered in 1684 by Giovanni Domenico Cassini. It is located at 4.9 R_S distance and has an average diameter of 1066 km; twice that of Enceladus and nearly three times that of Mimas. Tethys is an icy body similar in nature to Dione and Rhea. Its average density of 0.97 g/cm^3 indicates that it is composed almost entirely of water ice.

The surface of Tethys is one of the most reflective in the solar system, at visual wavelengths (the visual albedo is 1.229). This is the result of the surface being sandblasted by tiny particles in the E-ring, polishing the ice to a high shine. Tethys is also believed to have been internally active at one point, which has caused parts of the older terrain on the surface to have been resurfaced.

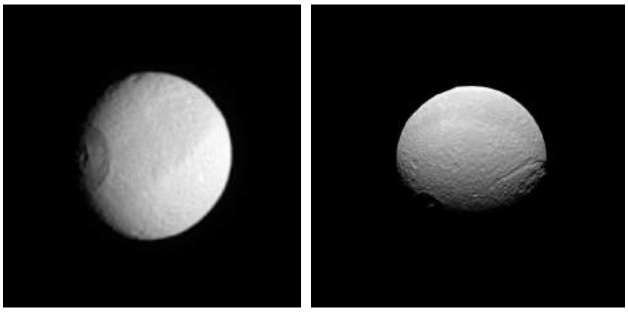

Figure 2.12: Images of Tethys taken by the Cassini spacecraft in visible light. In the image to the left, the large crater Odysseus can be seen. This crater is almost 450 km in diameter.
In the image to the right, the large valley Ithaca Chasma can be seen. On the limb at right, Ithaca Chasma extends northward.
Credit: NASA/JPL/Space Science Institute

Like Mimas, Tethys also has a distinctive huge impact crater, named Odysseus (see Figure 2.12, left). It is 445 km wide, which is approximately 2/5 of the moon's diameter. Unlike Mimas though, the crater on Tethys is quite flat – or, more precisely, it conforms to the spherical shape of Tethys. Another major feature on Tethys is a huge valley named Ithaca Chasma; 100 km wide, 3-5 km deep and 2000 km long – which spans approximately 3/4 of the circumference of Tethys (see Figure 2.12, right). One theory is that Ithaca Chasma could possibly have been created from shock waves travelling through the moon during the impact that formed Odysseus.

Tethys also has two *co-orbital* moons – that is, moons that share the same orbit – named Telesto and Calypso. These are located in the so called *Lagrangian points* L_4 and L_5, which are 60° ahead and behind Tethys in its orbit, respectively; Telesto being the leading moon and Calypso the trailing moon.

Dione

Dione was also discovered in 1684 by Giovanni Cassini. It is located at a distance of 6.3 R_S and has an average diameter of 1123 km; thus only slightly larger than Tethys. Like Tethys, Dione is composed primarily of water ice. However, Dione has an average density of 1.4757 g/cm^3, making it the third densest moon of Saturn (after Enceladus and Titan). This indicates that Dione must have a considerable fraction (about 46 %) of denser material, such as silicate rock, in its interior.

Dione is very similar to Rhea, but is smaller and denser; the albedo features and varied terrain are similar. The leading hemisphere of Dione is heavily cratered and uniformly bright (see Figure 2.13, left). The trailing hemisphere

Figure 2.13: Images of Dione taken in visible light by the Cassini spacecraft. In the image to the left both the leading hemisphere (left) and the trailing hemisphere (right) can be seen. The view is centered on the terminator between the two hemispheres, and north is up.
In the image to the right, the bright ice cliffs that characterise the trailing hemisphere can be seen as wispy streaks gleaming in the sunlight. These icy fingers reach across the surface of Dione.
Credit: NASA/JPL/Space Science Institute

has a network of bright, whispy streaks on a dark background, overlaying the craters (see Figure 2.13, right). These streaks have been confirmed as actually being ice cliffs created by tectonic fractures.

Like Tethys, Dione also has two co-orbiting moons; Helene in the leading Lagrangian point (L_4) and Polydeuces in the trailing Lagrangian point (L_5).

Rhea

Rhea was discovered in 1672, also by Giovanni Cassini. Located at a distance of 8.7 R_S, in the outermost part of the E-ring, it has an average diameter of 1529 km; more than three times that of Enceladus and almost four times that of Mimas.

It is an icy body with an average density of 1.233 g/cm^3, indicating Rhea is composed of about 1/4 rock and about 3/4 water ice. It was earlier assumed that Rhea possessed a rocky core in its center; this theory has later been disproven by measurements of the moment of inertia taken by the Cassini spacecraft, which indicate that the interior of Rhea is homogeneous.

The surface of Rhea is heavily cratered and also displays bright, whispy markings. The features on both the leading and trailing hemispheres of Rhea resemble those found on Dione, which suggests that the composition and histories are similar. Therefore, the whisps on Rhea – also similar to those found on Dione – are most likely ice cliffs too. See Figure 2.14.

*Figure 2.14: Both these images were taken in visible light by the Cassini spacecraft.
To the left is a look at many of the craters on Rhea including both ancient features (e.g. the large and extremely old basin just above the center, called Tirawa), as well as more recent, younger features (e.g. the bright ray crater, and the many craters overprinting Tirawa).
To the right a view of the ancient plains and the bright, whispy streaks featured on both hemispheres of Rhea can be seen. These bright streaks, like those on Dione, have been shown by the Cassini spacecraft to be tectonic features.
Credit: NASA/JPL/Space Science Institute*

2.4.3 Moon Interaction with E-ring

The E-ring is vast, no matter where you draw its outer boundary. At the very least, it is 300 000 km wide; by the definition within this thesis, the figure is about 422 000 km; and some observations suggest that the E-ring even extends beyond the orbit of Titan, making it more than 1 000 000 km wide! However, it is still incredibly wide, and numerous mathematical models show that such a ring is unstable, with a lifespan between 10 000 and 1 000 000 years. Therefore, the particles making up the ring must be replenished constantly, or the ring would cease to exist.

The discovery of Enceladus orbiting within the E-ring at the spot where the ring is both flattest and has the highest density (see Figure 2.15), gave rise to several theories suspecting Enceladus to be the primary source of particle production for the E-ring. This hypothesis also seemed to be proven correct by the flybys of Enceladus made by the Cassini spacecraft.

There are two distinct mechanisms feeding the E-ring with particles. The first – and probably most important – source is from the cryovolcanic plume in the south polar region of Enceladus (see Figures 2.10 and 2.15). While the majority of particles vented fall back to the surface, some of them escape the gravity of Enceladus (which only has an escape velocity of 866 km/h) and enter the E-ring into orbit around Saturn. The second mechanism for particle production comes from meteoric bombardment of a moon, wherein the impact releases dust particles from the moon surface, hurling them out into space.

This mechanism of feeding the E-ring is valid for all Saturn's moons orbiting within the E-ring.

Recent discoveries – made within this thesis as well as by other research teams[9] – seem to suggest that there is more going on with the moons in the E-ring than we currently know. The findings seem to indicate that Enceladus, while certainly being a major source of particle production with its giant water plume, is most likely not the *only* major source for the E-ring; effects from high particle concentrations seen around Enceladus, can also be seen, as presented here, in the vicinity of Tethys and Dione as well as Rhea!

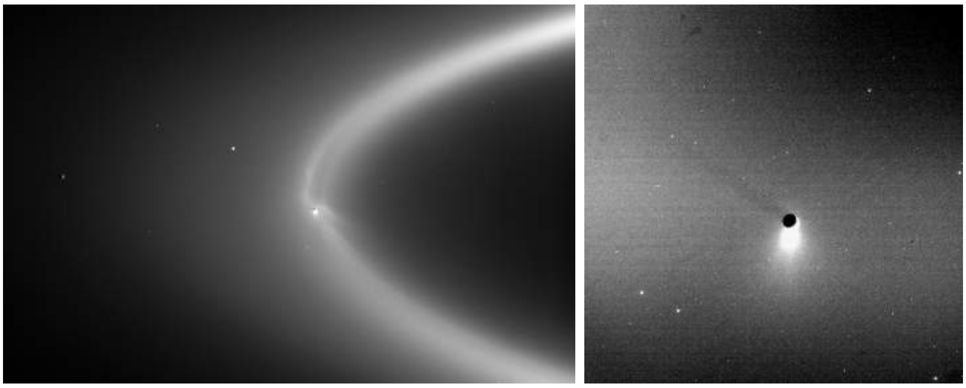

Figure 2.15: Images taken in visible light by the Cassini spacecraft, showing how the cryovolcanism on Enceladus is feeding the E-ring.
To the left the densest part of the E-ring can be seen, with Enceladus in its center (the tiny black dot near the center of the image). The large amount of ice particles ejected from the southern polar region of Enceladus can be seen just below the moon. In addition, wispy fingers of bright icy particles can be seen, whose configuration may hint at an interaction between Saturn's magnetosphere and the ejected particles.
To the right is a closer look at Enceladus in the center of the E-ring. The plume of Enceladus can here be clearly seen, blazing like an icy torch as it shines in the scattered sunlight. The bright dots in the image are background stars or cosmic ray hits on the camera detector, and are not part of the E-ring.
Credit: NASA/JPL/Space Science Institute

---

[9] See e.g. [Jones et al., 2007]

3

The Cassini-Huygens Mission

The Cassini-Huygens mission is the result of a large, international cooperative effort between NASA, ESA, the Italian Space Agency (Agenzia Spaziale Italiana, ASI), and also many contributors from the industry as well as academic institutions in both Europe and the United States. By sharing cost and resources, this partnership makes possible a mission that would otherwise be too big in terms of cost and scope for any single organisation or nation.

Due to the vast distance between Earth and Saturn, sending a spacecraft to the Saturnian system to take only a few measurements with few scientific instruments would be wasteful. But thanks to the collaboration of several thousand scientists all over the world, both the Cassini orbiter and the Huygens lander have been equipped with whole arrays of highly sophisticated instruments.

3.1 Mission Overview

The purpose of the mission is to study the Saturnian system. From the launch in October 1997, the voyage to Saturn took almost seven years, and included four gravity-assist maneuvers in which the spacecraft does a flyby of a planet to use the gravitational pull as a slingshot-effect to gain speed without using fuel. In July 2004, Cassini-Huygens reached Saturn and entered into orbit, thus beginning its primary mission including more than 70 orbits around Saturn spanning over a period of four years. The mission has later since been extended to July 2010.

3.1.1 Cassini

The Cassini orbiter focuses on collecting detailed data about Saturn, its rings and the moons orbiting the gas giant. This region is both fascinating and complex, and scientists hope to gain a further understanding of it from the data collected. Among the main scientific goals for Cassini are: measuring the huge magnetosphere of Saturn; analyse the rings up close; and study the composition and atmosphere of Saturn.

On July 1, 2004 Cassini began its SOI (Saturn Orbit Insertion) manoeuvre, where it approached Saturn from below the ring plane and crossed through the large gap that exists between rings F and G. After that Cassini coasted above the rings and captured data on the extensive ring system of Saturn. This took Cassini to the point closest to Saturn it will reach through its entire mission. During this, a massive amount of high resolution images of the rings and the complex structures in the ring plane were taken.

3.1.2 Huygens

Along on the mission is also the Huygens probe, whose function is to study the lower atmosphere and ground conditions on Saturn's largest moon Titan. By detatching from the Cassini orbiter and sailing down through the dense atmosphere of Titan by means of a parachute, its objective was to land safely on the surface and take images of the landscape as well as take readings and samples from the soil, for as long as the battery power could sustain it.

Huygens detatched from Cassini on Dec 25, 2004 and coasted for 21 days before reaching Titan and entering its atmosphere. For approximately two and a half hours it sailed down through the atmosphere while collecting atmospheric data and taking more than 750 images. When on the surface, it managed to collect data during one hour and twelve minutes and relay it all back to Cassini in orbit, before finally going offline. This was far longer and far more data than anyone expected.

3.2 Instruments on board Cassini

This section focuses on the scientific instruments used in the mission. Since the Huygens probe was only studying Titan, which is outside the scope of this thesis, we will only focus on the instruments that are on board Cassini.

The instruments are divided into smaller groups called instrument packages. Each package is a collection of instruments which are designed to carry out specific scientific studies – some instruments working in concert with the others in the package, and some instruments doing separate measurements. The Cassini orbiter is equipped with a total of twelve instrument packages for scientific measurements.

Here follows a brief introduction to those instrument packages on board Cassini which contain instruments either used during the work presented in this thesis, or otherwise have a bearing on the topic of this thesis.

3.2.1 Cassini Plasma Spectrometer

The Cassini Plasma Spectrometer (CAPS) is a collection of instruments for exploring the plasma in Saturn's magnetosphere. CAPS consists of three instruments: the Electron Spectrometer (ELS), measuring the flux of electrons as a function of energy/charge and aperture direction; the Ion Mass Spectrometer (IMS), measuring the flux of positively charged atomic and molecular ions as separate species, obtaining the ion mass; and the Ion Beam Spectrometer (IBS), measuring the flux of positively charged ions of all species, obtaining the energy and direction.

Together, the CAPS instruments study the composition, density, flow, velocity, charge and temperature of both electrons and ions in the plasma it encounters. For this thesis, only the two ion instruments are of interest, since they were involved in the background that spawned this project (see section 4.1.1).

It is also worthwile to note that, in comparison with other spacecraft with instrument packages dedicated to plasma studies, Cassini is a three-axis stabilised (i.e. non-spinning) spacecraft. What this means for CAPS is that it limits the particle observations in a given field of view, dependent on the spacecraft orientation.

3.2.2 Radio and Plasma Wave Science

The Radio and Plasma Wave Science (RPWS) package has as its main task to receive and measure the radio signals which are coming from Saturn, including the radio waves that are given off by the interaction of the solar wind with Saturn and Titan. RPWS studies the configuration of Saturn's magnetic field, monitoring and mapping Saturn's ionosphere and plasma, and lightning from Saturn's atmosphere. It also determines the distributions of dust and meteoroids throughout the Saturnian system; including between the icy satellites, the rings, and Titan.

The main components of the RPWS package are: an electric field sensor made up of three 10 m long antenna elements; a magnetic search coil sensor assembly (3 magnetic coils); and a 5 cm diameter Langmuir probe mounted on a boom and situated 1.5 m from the spacecraft body. Together, these instruments measure electric and magnetic fields in the plasma of the interplanetary medium and Saturn's magnetosphere, as well as electron density and temperature.

Two of the three antenna elements were involved in doing interferometry measurements which are the background that led to the formation of the main goals for this thesis (see section 4.2.2). However, the work done in this project focuses more or less completely upon data collected using the Langmuir probe. The Langmuir probe itself is covered in great detail in chapter 5; what it is, the underlying theory behind it, and how it is used in this project.

4

Purpose of this Work

4.1 The Plasma Energy Dilemma!?

4.1.1 Different Ram Energies

In the early days of Cassini's science phase, two instruments were measuring plasma ram energies[1] in the inner magnetosphere close to Saturn (3–5 R_S).

The Langmuir Probe (LP) instrument was designed to measure cold plasma and therefore has high resolution for low energies. When measuring the ram energy in the plasma, it got results of < 20 eV, and ion temperatures were below 3 eV.

The Cassini Plasma Spectrometer (CAPS) instrument, on the other hand, is designed for measurement of hotter plasma than LP is, and does not have enough resolution to (easily) see energies of < 10 eV. Also, the spacecraft – being negatively charged (see section 5.1) – will repel low energy electrons and accelerate ions towards the spacecraft, which further limits how low energies CAPS can detect. Therefore, when CAPS was measuring the ion energies, it was seeing 100–200 eV, i.e. significantly larger energies than LP was.

Clearly, there was an inconsistency between the LP and CAPS results that was not easy to resolve. There was a plasma energy dilemma!

4.1.2 Speeds Around Saturn

Keplerian Speed, v_{grav}

From the theory of *central force* an object moving around Saturn is affected by two forces; the centripetal force F_{cp} and the gravitational force F_{grav}. When these forces balance each other, we get

$$F_{cp} = F_{grav} \Leftrightarrow \frac{m\,v^2}{r} = G\frac{m\,M_{\saturn}}{r^2} \Leftrightarrow v_{grav}(r) = \sqrt{\frac{G\,M_{\saturn}}{r}} \tag{4.1}$$

---

[1] Energies in the plasma ram direction, which is the direction that incident plasma particle flow upon the instrument comes from.

and this is the speed with which an object at a given distance from Saturn, and with a given mass, is moving around Saturn under the influence of gravity.

Corotational Speed, v_{rot}

Corotation means to rotate in conjunction with another body, i.e., as if it was attached to the body (e.g. think of the beam from an old fashioned light house). It is defined as

$$v_{rot}(r) = |\mathbf{\Omega} \times \mathbf{r}| = \frac{2\pi}{\tau_{rot}}\, r \tag{4.2}$$

where $\mathbf{\Omega}$ is the rotational axis of Saturn, and $\tau_{rot} \approx 10.7$ h the rotational period. This is the speed with which Saturn's magnetic field lines and, consequently, its magnetosphere rotates.

4.1.3 Difference in Energy $\Longleftrightarrow$ Difference in Speed

Kinetic energy is coupled with velocity as

$$E_k = \frac{m\, v^2}{2}\ [\mathrm{J}] \ = \frac{m[\mathrm{amu}]\, m_H\, v^2}{2e}\ [\mathrm{eV}] \tag{4.3}$$

which means that the difference in ram energy observed by the two instruments in section 4.1.1 translates into an inconsistency with regard to *ion speed* in the inner magnetosphere.

By using equations (4.1), (4.2) and (4.3), assuming water ions ($m_i = 18$ amu), we find that CAPS gives an ion speed that is in agreement with corotation (or $\mathbf{v} \times \mathbf{B}$ acceleration). LP on the other hand gives results where the ion speeds are in agreement with Keplerian motion of ions that, possibly, are coupled with charged dust or neutral gas.

The inconsistency in the ion speed from these two measurement sources posed the dilemma: Is the plasma corotating or not? CAPS says yes, LP says no. It turns out from this study that both can be correct!

4.2 Settling the Dispute

4.2.1 Which One Was Correct?

Initially, there was a discrepancy between CAPS ion measurements and LP ion observations. This led to a disagreement between the two teams about the interpretation of results or, rather, there was a disagreement in measurements. However, the LP team was convinced that their measurements were correct and thus published their results in [Wahlund et al., 2005]. The reasoning behind the disagreement was probably something like this:

The plasma, being a cloud of ionised gas and therefore made up of charged particles, should be subject to the force from Saturn's magnetic field. Since the charged particles would be coupled to the magnetic field lines, and the magnetic field is bound to Saturn's rotation, logically it seemed reasonable that the plasma should be corotating with Saturn. This effect is well known, and one says that the plasma in Saturn's magnetosphere is *frozen into* the magnetic field. From Ohm's law

$$\mathbf{j} = \sigma\left(\mathbf{E} + \mathbf{v} \times \mathbf{B}\right) \tag{4.4}$$

one can for $\sigma \rightarrow 0$ see that an electric field is induced, $\mathbf{E} = -\mathbf{v} \times \mathbf{B}$, such that the plasma moves with the magnetic field according to

$$\mathbf{v} = \frac{\mathbf{E} \times \mathbf{B}}{|\mathbf{B}|^2} \tag{4.5}$$

In any case, to try and find the problem a list of possible error sources for LP was compiled and then excluded one by one as a possibility. In the end, none of the possible error sources were found to be the cause of the observations. This seemed to suggest that either there was another possible source of error which had not been thought of, or that the results from LP were indeed correct. The problem with this was that the CAPS team also searched for possible error sources, but none could be identified there either, so CAPS also seemed to be correct!

4.2.2 Introducing the Arbiter

As both instruments gave opposite results there came the need for a third, independent measurement method to act as arbiter. This led to the decision of using *$\delta n/n$ interferometry*, where two 10 m RPWS antenna elements were used in concert with the Langmuir probe (these can be seen in Figure 4.1) in current sampling mode (see section 5.4), to give up to 7000 samples/s. The measurement took place on 2005-10-30 during a period of 1 hour and 40 minutes. (Note: Another 2 h run was made later on 2006-07-23, which just confirmed the first measurements.)

By using the phase difference, $\Delta\varphi$, between the antennas when measuring the plasma, the speed can be calculated according to

$$v_s = \cos\theta_{sd}\, d\, \Delta f\, \frac{2\pi}{\Delta\varphi\,[rad]} \tag{4.6}$$

The results from the interferometry measurement showed *two* distinct slopes in $\varphi(f)$, which means that there must be *two* ion populations present in the inner magnetosphere of Saturn; one hotter corotating and one colder moving at close to Keplerian speed. What Figure 4.2 shows, is that both CAPS and LP were, in fact, correct. As expected, the presence of a corotating ion population suggested by CAPS was now confirmed, which came as no surprise to anyone. However, what was surprising is that the interferometry result also confirmed the findings from LP; that not all ions were corotating – some of them were in fact moving at much slower speeds!

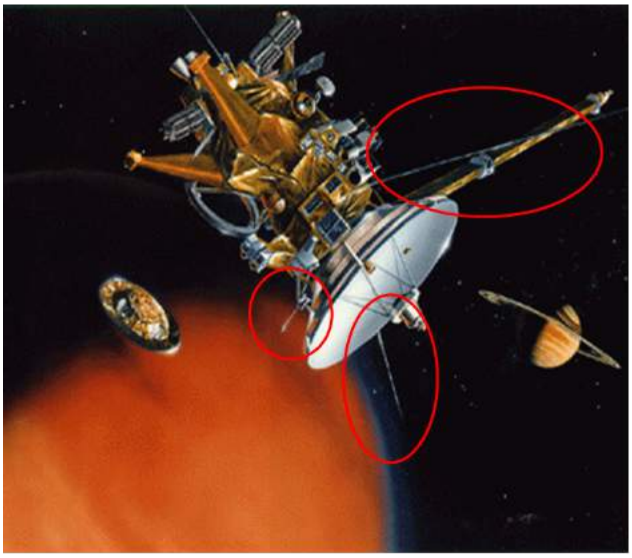

Figure 4.1: The Cassini spacecraft with the interferometry antennas and the Langmuir probe in focus

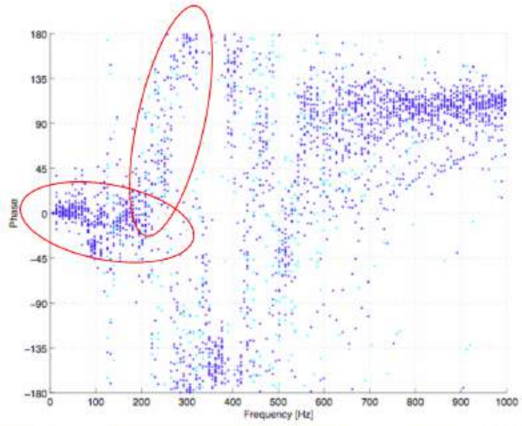

Figure 4.2: E- vs E+ phase from the interferometry measurement. The lower left area marked in red shows the corotating population, and the upper right area marked in red shows the population moving at close to Keplerian speeds. Figure courtesy of Jan-Erik Wahlund.

4.3 A New Power is Rising . . .

The presence of this colder ion population immediately sparked the wonder about what could be causing this effect. There had to be some kind of braking force present that could slow down the ions and, since Keplerian speeds were not directly applicable for ions (since the gravitational forces involved are negligible for the plasma compared to electric forces), there had to be something that *was* moving at Keplerian speed grabbing hold of some of the ions, and by a drag effect slowing them down.

4.4 . . . Dust — Plasma Interaction?

One possible reason for the presence of this colder ion population is the interaction between low energy ions in the plasma and charged dust particles in the E-ring. These dust particles are mainly ice grains which are negatively charged by a few volts. Being negatively charged, they will try to attract the positively charged ions from the surrounding plasma. Ions which are hot enough – i.e. have a high enough energy – will not be affected by the dust grains; they will simply continue along their path. However, the colder ions (with low energies) will be trapped in a *potential well* by the dust grains, as can be seen in Figure 4.3.

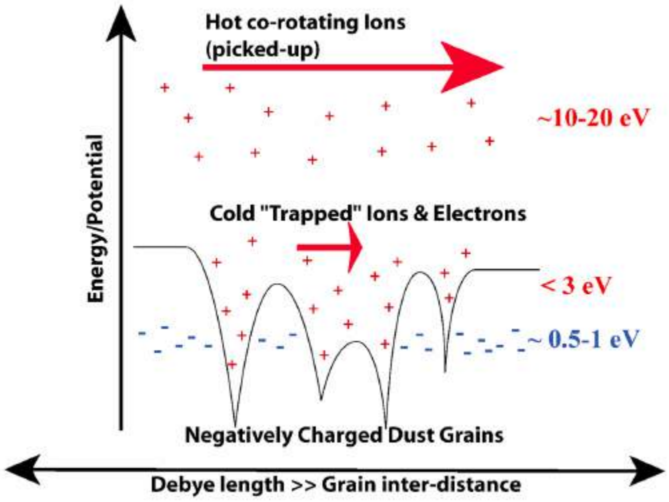

Figure 4.3: Ion pickup and the trapping of colder ions. Courtesy: Jan-Erik Wahlund

This coupling will affect the dynamics of the plasma in such a way that, when some of the ions get coupled to the ice grains, the inertia of these dust grains will act as a drag effect upon all the ions that are trapped. What this means is that part of the previously corotating ions will now be forced down to near Keplerian speeds by the dust particles in the E-ring.

4.5 The Stage is Set

In this report it will be shown that the mechanism of dust—plasma interaction can contribute significantly to explain the observations put forth based on the measurements. Further to this, an estimation will be made of how large a part of the total ion density belongs to that subset which is trapped by dust particles and is slowed down in speed. This estimation will be done in the E-ring as a function of distance from Saturn, to highlight an increased coupling effect in certain regions of high interest, e.g. near the icy moons in the E-ring. As the results proposed will show, some interesting effects have been discovered; some of which may confirm previous hunches, and yet some may spark new ideas . . . .

5

The Langmuir Probe

The Langmuir probe is an instrument used on many spacecraft for measuring several physical quantities of a space plasma. One might call it a whole plasma laboratory all rolled into one single instrument. The probe itself might not look like much from the outside; in most cases a small metal ball attached to a metal rod. But what looks like simplicity itself, is actually incredibly useful when combined with sophisticated electronics.

Depending on how the Langmuir probe is operated, it measures different parameters and, by combining several operation modes, one is able to combine all the parameters into a pretty complete and accurate representation of the plasma that was measured. The knowledge gained from the behaviour of the plasma furthers the understanding of how the plasma interacts with its environment, and why.

A further description of what the Langmuir probe on board Cassini looks like and how it is used, is discussed in section 5.5. But first, we start with the basics and discuss briefly the theory behind Langmuir probes.

This chapter is based on lecture notes from Jan-Erik Wahlund. Much of the text found here is summarised in [Behlke et al., 2000].

5.1 Basic Theory

5.1.1 Uncharged Body in Plasma

Plasma is referred to as the fourth state of matter. A plasma is an ionised gas, which means that it is a gas consisting of ions and (free) electrons. If we take an uncharged body of any given material and insert it into the plasma, the electrons in the plasma will hit the body more frequently than will the ions at the same temperature. The reason for this is, quite simply, that the ions are much heavier which results in the electrons moving at higher speeds. This will give the body a *negative* charge, when no other charging effects are present.

Since the body has attained a negative charge, the electrons are naturally repelled. When this repelling effect becomes large enough to equate the effect from the higher electron speeds, these effects cancel out and the body approaches an equilibrium state. This state will in the end see the body obtain a slight negative charge with a potential on the order of a few volts negative, and holds true for *any uncharged body* inserted into a plasma[1], in absence of other charging mechanisms. This is the simplest physical situation, and an example of when this occurs is a satellite in eclipse (without any energetic radiation present).

5.1.2 Point(-like) Charge in Plasma

If we instead put a point charge into the plasma, plasma particles of *opposite charge* will be attracted to it. These will then form a cloud around the point charge which acts as a shield, screening out the influence of the point charge from the surrounding plasma. This effect is known as *Debye shielding.* The potential from a point charge in a plasma is defined as

$$V(r) = \frac{q}{4\pi\,\varepsilon_0\,r}\,e^{-r/\lambda_D} \tag{5.1}$$

with λ_{D} being known as the *Debye length* and given by

$$\lambda_{\mathrm{D}} = \sqrt{\frac{\varepsilon_0\,k_{\mathrm{B}}\,T_{\mathrm{e}}}{n\,q^2}} \tag{5.2}$$

where T_e is the plasma electron temperature, n the plasma density[2], q the charge of the point charge and r the radial distance from the point charge.

The Debye length is the characteristic length scale for the shielding effect described above, and as such provides an estimate of the distance over which the plasma is influenced by the point charge. It is here important to note that the Debye length increases when the temperature increases, and decreases when the density increases. This means that we will find the largest Debye length in a plasma that is hot and tenuous.

The cloud of plasma particles, which is delimited by the Debye length and surrounding every charged object immersed in the plasma, is known as the *Debye sheath.* This is the layer of the plasma which is influenced by the vicinity of the object through the above described effect. If the plasma is cold, the shielding outside this cloud will be perfect. For warmer plasmas however, the small potentials at the boundary of the cloud will not be able to prevent the particles from escaping out into the surrounding plasma.

---

[1] It is important to note that this is under the assumption that the plasma is "simple", meaning that there is no photoemission, and the relative velocity with respect to the body is negligible. Other factors influencing this is higher plasma density (meaning more electrons hitting the body and thus more negative charge), and electron temperature T_{e} which can give rise to as much as -100 V.

[2] Expressed in number of particles per unit volume.

From this it is easy to understand that to do plasma measurements from a spacecraft, we must first make sure that the instrument is situated outside the Debye sheath of the spacecraft. Otherwise, the measurements would be tainted by the influence of the spacecraft itself. This fact is just one of several reasons why Langmuir probes are attached at the end of long booms.

5.1.3 Conductor in Plasma

It is known that, for a plasma in thermal equilibrium, the particle distribution functions are Maxwellian. This means that the thermal velocity $v_{\mathrm{th},j}$, of the particle species j, is given by

$$v_{\mathrm{th},j} = \sqrt{\frac{k_{\mathrm{B}}\,T_j}{m_j}} \tag{5.3}$$

where m_j is the mass of particle species j. From this it can clearly be seen that, for the same temperature, the lighter particles have a higher speed.

If we take a conductor, connected to a voltage source at a certain potential[3], and insert it into the plasma, the conductor will start to collect a current. If the conductor is then disconnected from the voltage source, it will build up a negative charge – due to the excess of electrons hitting it – until reaching a potential at which no more current will flow to the conductor. This potential is called the *floating potential*, V_{float}, and at the floating potential the electron current and the ion current balance each other[4], which means we have no net current.

5.2 Probe Currents

5.2.1 Two Different Theories

A Langmuir probe is a conductor that is immersed in a (space) plasma and, as such, the basic principles behind its operation have been described. However, in order to make estimates about the various properties of the plasma from the Langmuir probe measurements, we need to look at the different currents between the plasma and the probe. When the probe is at the floating potential V_{float} it receives no current, but we now need to look at how the current is dependent on the potential the probe has *with respect to the plasma*.

---

[3] In fact, this is the *space potential*, which is not covered here and left as a study for the interested reader.

[4] There are a few other currents involved in this balance as well, and they will be discussed in the following section.

Consider a spherical probe. We now make the following assumptions, for simplicity:

- The plasma is collisionless
- The plasma is isotropic
- There is no external magnetic field
- The surface properties of the probe are homogeneous

In reality, the theory for the probe currents is actually somewhat complex, since the probe itself affects the plasma through the effect of Debye shielding, as has been previously mentioned.

Let us denote the radius of the Langmuir probe as r_p. This allows us to distinguish between two extreme cases.

When $r_\mathrm{p} \ll \lambda_\mathrm{D}$, the screening effect from the Debye sheath is weak. This means that the motion of a single particle is independent of the motion of other particles, and thus mainly governed by the probe potential. In this case, the collection of particles by the probe is said to be *Orbital Motion Limited* (OML). This theory, first quantified by Mott-Smith and Langmuir in 1926, is not based on plasma physics, but regards a distribution of particles moving in the vacuum field from the probe, thus obtaining trajectories determined only by conservation of energy and angular momentum.

On the other hand, if $r_\mathrm{p} \gg \lambda_\mathrm{D}$, the Debye screening effect becomes important, which means that the properties of the Debye sheath will change with the charge accumulation. This case is called the *Sheath Limited* (SL) regime of particle collection. The SL-theory is rather involved, and since it only becomes an issue in a really dense plasma[5] – which most often does not come into play within the scope of this thesis – it will not be discussed further.

There is also the case when r_p is close to λ_D. Here we have a mix of OML and SL, which is even more complicated and will also be omitted.

5.2.2 Currents from Bias Voltage

By using an OML approach, we are able to obtain expressions for the electron and ion currents as functions of the probe bias voltage, U_B, delivered by the instrument, which we will define as

$$U_\mathrm{B} = V_\mathrm{probe} - V_\mathrm{plasma} - V_\mathrm{float} \tag{5.4}$$

In the original work by Mott-Smith and Langmuir [1926], they find – for spherical probes – that the electron current and the ion current are, in the case where

---

[5] For example, in the ionosphere of Titan, where a typical value for $\lambda_\mathrm{D} \approx 8$ cm ($n_\mathrm{e} \approx 1000$ cm^{-3}, $T_\mathrm{e} \approx 0.1$ eV).

$U_{\mathrm{B}} + V_{\mathrm{float}} > 0$, given by

$$I_{\mathrm{e}} = I_{\mathrm{e0}}\,(1 - \chi_{\mathrm{e}}) \tag{5.5a}$$

$$I_{\mathrm{i}} = I_{\mathrm{i0}}\,e^{-\chi_{\mathrm{i}}} \tag{5.5b}$$

and in the case where $U_{\mathrm{B}} + V_{\mathrm{float}} < 0$ they are given by

$$I_{\mathrm{e}} = I_{\mathrm{e0}}\,e^{-\chi_{\mathrm{e}}} \tag{5.6a}$$

$$I_{\mathrm{i}} = I_{\mathrm{i0}}\,(1 - \chi_{\mathrm{i}}) \tag{5.6b}$$

where

$$\chi_j = \frac{q_j\,(U_{\mathrm{B}} + V_{\mathrm{float}})}{k_{\mathrm{B}}\,T_j} \tag{5.7}$$

and

$$I_{j0} = -A_{\mathrm{LP}}\,n_j\,q_j\sqrt{\frac{k_{\mathrm{B}}\,T_j}{2\pi\,m_j}} \tag{5.8}$$

Here, for particle species j, n_j is the number density, q_j the charge, T_j the temperature and m_j the mass of that particle species. A_{LP} is the area of the Langmuir probe; that is $A_{\mathrm{LP}} = 4\pi\,r_{\mathrm{p}}^2$. The minus sign is there to reflect that we take the current *from* the probe *to* the plasma as the positive direction. From these equations it is easy to see, that simply by looking at the currents to the probe, it is possible to estimate the temperature and density of the different particle species in the plasma.

5.2.3 Voltage-Current Characteristics

Let the total current, I, to the probe be defined as the sum of the electron current and the ion current

$$I = I_{\mathrm{e}} + I_{\mathrm{i}} \tag{5.9}$$

If we now plot the dependence of this total current upon the bias voltage, U_{B}, we find that the behaviour will have the general shape presented in Figure 5.1, which is an example of a typical *U-I* curve obtained using the above equations. The *voltage-current characteristics* (*U-I* characteristics) is one of the most important tools when using Langmuir probes for measuring properties of space plasma. Note also that, for high positive or negative values of U_{B}, the relationship is *linear*.

It is important to keep in mind that there is a limit on how much current can be collected by a Langmuir probe. The upper theoretical limit is reached when the probe collects every *available* electron, meaning every electron that enters the Debye sheath surrounding the probe. For a perfect OML-plasma however, this limit does not exist, since in that case the Debye sheath has *infinite* extension.

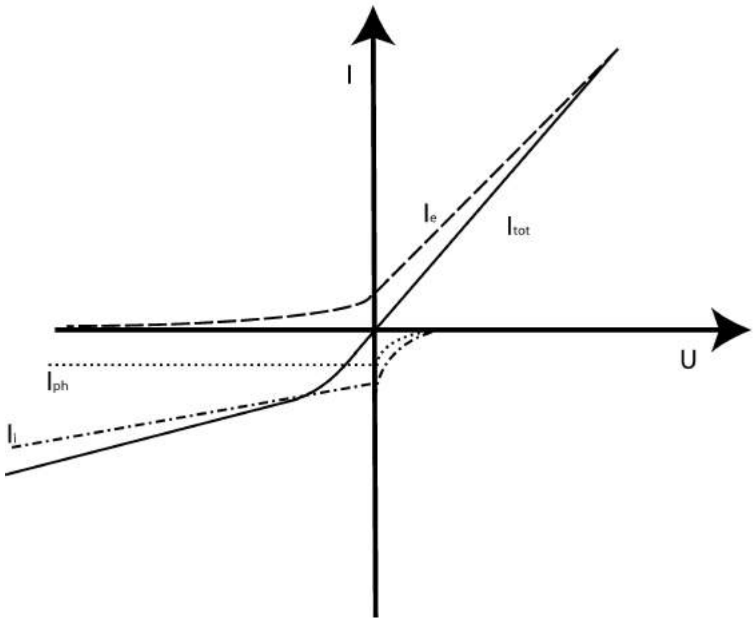

Figure 5.1: A sketch showing the voltage-current characteristics of the Langmuir probe. The dashed, dotted and dash-dotted lines represent the current contribution from electrons (I_{e}), photoelectrons (I_{ph}) and ions (I_{i}) respectively. These add together to form the solid line, which represents the total current (I_{tot}) to the probe.

5.3 Ion Side Currents

5.3.1 The Ion Side

The *ion side* is defined as being the part of the U-I characteristic where the potential is negative; that is, where $U = U_{\mathrm{B}} + V_{\mathrm{float}} < 0$. It is called the ion side because, for a negative relative potential, ions from the plasma are being attracted to the probe, and it is the current sampled from them that is dominating. Also, for a negative potential, all photoelectrons emitted from the probe escape, which will constitute a constant photoelectron current[6].

5.3.2 Plasma Drift Velocity

Up until now we have been working under the assumption that the probe is at rest with respect to the plasma surrounding it. Generally, this is not the case at all; in fact, it is a rare ocurrence indeed. The relative velocity between spacecraft and plasma usually lies in the range 5–30 km/s in the

---

[6] Constant in the sense that it is not varying for a certain solar EUV flux and a fixed spacecraft attitude (which will be discussed in chapter 6).

inner magnetosphere of Saturn (can go as high as several hundred km/s in the solar wind).

It becomes clear that we need to treat the imposed drift velocity of the plasma, since the relative velocity between spacecraft and plasma is so high that it becomes significant. Thus, the previously given OML expressions for the current are no longer applicable in their current form; they need to be extended to account for the drift velocity.

From the original work of Mott-Smith and Langmuir [1926], the extension with the Langmuir probe moving through a Maxwellian plasma was done by Fahleson [1967], where he arrived at the expression

$$I_\mathrm{i} \approx \pi\, r^2\, n\, e\, \sqrt{\frac{8 k_\mathrm{B}\, T_\mathrm{i}}{\pi\, m_\mathrm{i}} + v^2} \tag{5.10}$$

This means that the ion current will be larger if the probe moves through the plasma. By slightly rewriting the above equation, we obtain

$$I_\mathrm{i0} \approx A_\mathrm{LP}\, n_\mathrm{i}\, q_\mathrm{i}\, \sqrt{\frac{k_\mathrm{B}\, T_\mathrm{i}}{2\pi\, m_\mathrm{i}} + \frac{v_\mathrm{i}^2}{16}} \tag{5.11}$$

which is the *random ion current* compensated for the plasma drift velocity. In this equation A_LP is the surface area of the (spherical) Langmuir probe, n_i the ion (number) density, q_i the ion charge, T_i the ion temperature [K], m_i the ion mass and v_i the ion speed. This is the main contribution to the current on the ion side.

For the ions, we also get a kinetic energy contribution when moving through the plasma

$$\chi_\mathrm{i} = \frac{q_\mathrm{i}\, U}{\frac{m_\mathrm{i}\, v_\mathrm{i}^2}{2} + k_\mathrm{B}\, T_\mathrm{i}} \tag{5.12}$$

where $U = U_\mathrm{B} + V_\mathrm{float}$ as before. For the electrons we have

$$k_\mathrm{B}\, T_\mathrm{e} \approx \frac{m_\mathrm{e}\, v_\mathrm{th,e}^2}{2} \quad \gg \quad \frac{m_\mathrm{e}\, v_\mathrm{ram,e}^2}{2} \tag{5.13}$$

or one could also say $v_\mathrm{th,e}^2 \gg v_\mathrm{ram,e}^2$. This means that for electrons the kinetic energy is negligible compared to the thermal energy, but for ions this is not the case. There we have to take the kinetic energy into account as well, since it is on the same order as the thermal energy of the ions. This is due to the larger mass of the ions compared to the electrons, since $v_\mathrm{ram,e} \approx v_\mathrm{ram,i}$.

5.3.3 Current Components

The current on the ion side is comprised of several components. The main contribution is from the total ion current, I_i, compensated for the plasma drift velocity. But, also present are: I_ph, the contribution from escaping photoelectrons; I_dust, the contribution from dust grain impacts on the probe; and

$I^*_{\text{energetic}}$, the current from high energetic (> keV) particles (mainly electrons but also ions) hitting the probe. When adding together all the components, the total current on the ion side becomes

$$I_- = I_\text{i} + I_\text{ph} + I_\text{dust} + I^*_\text{energetic} \tag{5.14}$$

It is important to understand that when measuring the ion side[7] current, it is the total of all these components that is being sampled. Most times one is only interested in the pure ion current, I_i, which means that correction needs to be made for the other terms. In doing this, they are all assumed to be constant, which can in fact be shown but will be omitted here. Furthermore, I_dust and $I^*_\text{energetic}$ are both assumed to be small[8] in most cases, which only leaves I_ph to be corrected for.

5.4 Probe Measurements and Methods

The Langmuir probe is used for measuring general physical quantities. When talking about the various types of measurements that are being done, one says that the probe is *operated in different modes.* The most common modes of operation are

Voltage sweeps: measurements of electron and ion temperatures and densities, spacecraft potential, and relative UV-intensity.

Current sweeps: measuring basically the same quantities as the voltage sweeps.

δn/n: looking at plasma density fluctuations, and plasma flow velocity (sometimes with and sometimes without direction)

Dust detection: where estimates are made of impact rate, mass and size of micrometer sized dust grains

A figure summarising these modes graphically can be seen in Figure 5.2 below.

5.4.1 Voltage Sweeps

In this mode of operation the probe bias voltage, U_B, is swept over an interval from negative to positive bias (usually −32 V to +32 V) and the current is measured. This mode is shown in Figures 5.2a and 5.2b where, depending on the bias voltage being either positive or negative[9], either the electron current or the ion current is measured, respectively.

---

[7] This is in fact also true for the electron side, but negligible there however.

[8] This is not exactly true; they can have a significant impact on the total ion side current when they occur. However, their sporadic nature make their contribution negligible over time compared to the first term.

[9] With regard to the surrounding plasma.

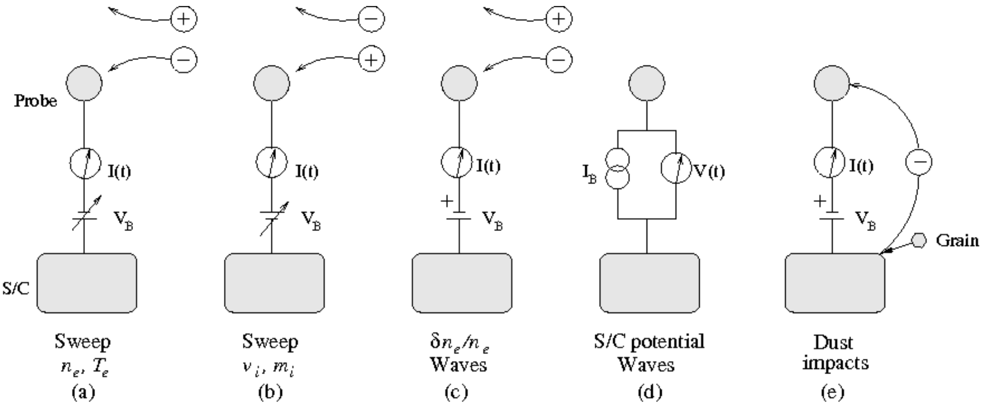

Figure 5.2: Illustration of the various basic modes of operation for a Langmuir probe. The first two cases, (a) and (b) correspond to a voltage sweep, where the potential is varied while the current is sampled. A constant positive bias potential is applied in (c) and the current fluctuations collected are assumed proportional to density fluctuations. In (d) a constant current is applied and the measured potential gives an estimate of the electric field. Finally, in (e) the impact of a micrometer sized dust particle produces a pulse in the sampled current. [Eriksson et al., 2006]

The analysis is using a non-linear least squares technique, which is a simultaneous fit of particle density n_j, temperature T_j and floating potential V_{float}.

To illustrate this mode, a voltage sweep from the Langmuir probe on board Cassini is shown in Figure 5.3 below. Note that this plot also shows the magnitude of the collected current in logarithmic scale. The blue dots represent real data points, while the solid red curve is a fit of the data points to the sum of the theoretical expressions for the currents, (5.5) and (5.6).

It can here be noted that this mode is relatively independent of the floating potential, V_{float}, hence, relatively insensitive to spacecraft charging. In fact, V_{float} can rather be determined from analysis of the sweep!

5.4.2 Density Interferometry ($\delta n/n$) Measurement

Estimations on the relative plasma density fluctuations, $\delta n/n$, can be done by biasing the probe to a (fixed) positive voltage U_{B} relative to the spacecraft and measuring the sampled current by the probe, see Figure 5.2c. Here, the probe is made sensitive to current fluctuations in the plasma, which are coupled to density fluctuations as

$$\frac{\delta I}{I} = \frac{\delta n}{n} \tag{5.15}$$

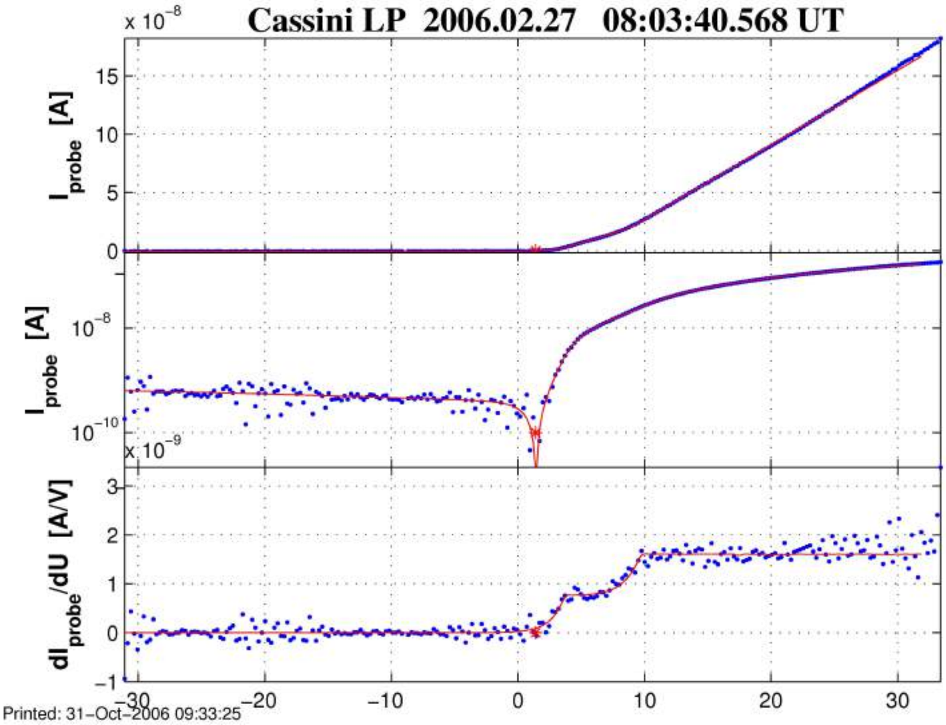

Figure 5.3: A sample of a Langmuir probe bias voltage sweep from the Cassini spacecraft. The figure shows the current as a function of bias voltage, in linear and logarithmic scale, as well as the derivative.

Note however that current fluctuations in the plasma are not *solely* caused by variations in the density of the plasma, but can also be caused by fluctuations in the electric field and/or electron temperature, as well as U_{SC}!

By using a pair of antennas, e.g. Langmuir probes (or, as in the case for the Cassini spacecraft; two 10 m RPWS antennas in concert with the Langmuir probe[10]), separated by a distance d, we are able to deduce information about the propagation properties of waves and solitary structures, or the extension of spatial irregularities in the plasma, by regarding the double antennas as a simple *interferometer*.

The simplest interferometer uses only two $\delta n/n$ sensors, which corresponds to measuring scalar quantities. The temporal difference between two signals, or phase difference in an incident wave, is used to estimate the speed of a perturbed density structure, see Figure 5.4, since

$$v_{\mathrm{plasma}} = \frac{L}{\Delta t} \tag{5.16}$$

---

[10] See Figure 4.1

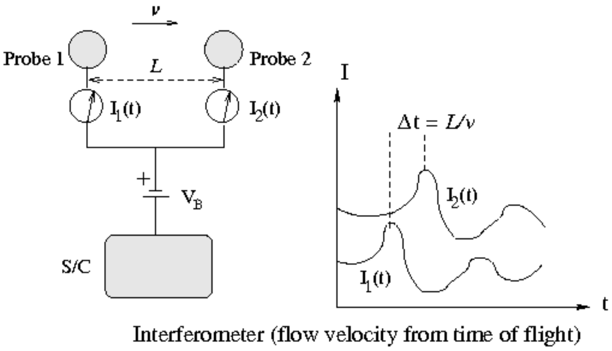

Figure 5.4: Basic model illustrating a simple $\delta n/n$ interferometer. The time delay between the signal received by the antennas are used to derive the plasma flow speed, and sometimes also the direction of the flow. [Eriksson et al., 2006]

where L is the effective distance between the sensors and Δt the time shift in the signal. In these measurements one must also consider the effects of short wavelengths and Doppler shift, as well as Doppler broadening.

5.4.3 Dust Detection

A Langmuir probe can also be used to infer impact rate and possibly mass and size of micrometer-sized dust grains.

Let us consider a micron-sized dust particle hitting the hull of a spacecraft at a relative velocity of a few kilometers per second. At the impact, the large kinetic energy released completely vapourises the dust grain. The effect this has is that charged dust, like any negatively charged component, will contribute to the total sampled current.

Assuming $T_{\text{dust}} \ll \frac{1}{2}\, m_{\text{dust}}\, v_{\text{dust}}^2$, we obtain for the dust current component to the probe

$$I_{0,\text{dust}} = -A_{\text{LP}}\, q_{\text{dust}}\, n_{\text{dust}}\, \frac{|v_{\text{dust}}|}{4} \tag{5.17a}$$

$$\chi_{\text{dust}} = \frac{2e\,(U_{\text{B}} + V_{\text{float}})}{m_{\text{dust}}\, v_{\text{dust}}^2} \ll 1 \tag{5.17b}$$

$$e^{(-\chi_{\text{dust}})} \approx 1 \tag{5.17c}$$

This means that charged dust will not affect the gradient of the current, but will instead give a *constant ram flux*

$$I_{\text{dust}} = -A_{\text{LP}}\, q_{\text{dust}}\, n_{\text{dust}}\, \frac{|v_{\text{dust}}|}{4} \qquad \textit{for all } U \tag{5.18}$$

Normally, this gives a negligible contribution. However, the yield from escaping secondary electrons is *not* negligible

$$I_{\text{dust,sec}} = -Y_{\text{yield}} \cdot I_{\text{dust}} \tag{5.19}$$

where $I_{\mathrm{dust,sec}} \approx$ -(0.1–0.3) nA from observations. This is of the same order as other fluctuations in the current (e.g. photoelectrons), which means that dust impacts can sometimes significantly affect the sampled current.

5.4.4 Wake Effects

Another effect resulting in erroneous measurements, is the formation of a wake behind a moving satellite. This is due to the high velocity of the satellite ($v_{\mathrm{sc}} \sim$ 10 km/s) compared to the thermal speed of the ions ($v_{\mathrm{th,i}} \sim$ 1 km/s). A wake appears when

$$\Delta v_{\mathrm{sc}} = |v_{\mathrm{sc}} - v_{\mathrm{plasma}}| \geq C_{\mathrm{s}} = \sqrt{\frac{e\,(T_{\mathrm{e}} + T_{\mathrm{i}})[\mathrm{eV}]}{m_{\mathrm{i}} + m_{\mathrm{e}}}} \approx v_{\mathrm{th,i}} \tag{5.20}$$

One way to think of this is the satellite moving through the plasma and ploughing away the ions. Thus, the concentration of ions (and electrons, since electrons follow the motion of the ions) will be smaller behind the satellite. However, the size of the wake cone is different for electrons and ions; since electrons move faster[11] than ions, they will re-enter the wake sooner behind the spacecraft than the ions will (see [Engwall, 2006]). Furthermore, a shock wave may develop in front of the satellite. Inside the shock front the electron density can increase significantly.

The strength of the wake effect depends on the ion composition and the ion temperature T_{i} of the ambient plasma, since different ion species have different thermal energies. It also depends on the electron temperature T_{e} for the same reason.

5.5 The Langmuir Probe on board Cassini

The Langmuir probe used in the Cassini mission consists of three parts; the actual probe itself, which is a titanium sphere ~5 cm in diameter, a ~1.5 m long boom assembly attaching it to the spacecraft and, between the probe and the boom, a short stub ~10 cm in length. A picture of the Langmuir probe on board Cassini, showing its different parts, is presented below in Figure 5.5.

As mentioned, the probe is a titanium sphere, with a titanium nitride (TiN) coating. This substance is chemically inert and durable; a very important prerequisite for missions that have a long duration, such as Cassini.

5.5.1 Three Electron Component Analysis

The analysis of the voltage sweeps from the Cassini Langmuir probe utilises three electron components. In certain regions there are three significant electron populations present, e.g. in the ionosphere of Titan or the inner magnetosphere of Saturn.

---

[11] At the same temperature.

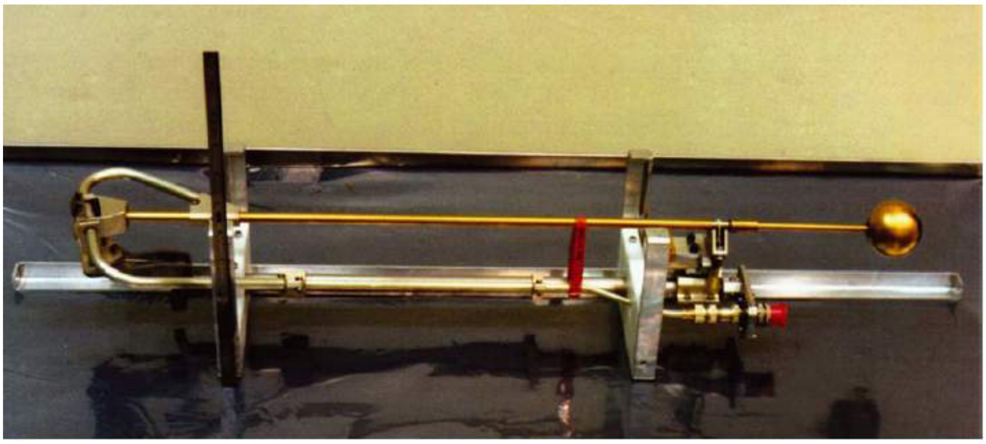

Figure 5.5: The Langmuir probe on board the Cassini spacecraft. The probe itself is the sphere on the end, the stub is the thinner rod (whose length is twice the diameter of the sphere) between the probe and the boom, and the boom is the remaining part (here folded before deployment).

To get accurate results, the analysis needs to take into account the effect of all three populations simultaneously. The three populations correspond to photoelectrons, cold electrons and also hot electrons which come into play mainly in regions of high density (which is the case in Titan's ionosphere).

The maximum number of electron populations – which significantly affect the response – is three, wherein a three component analysis is sufficient to handle the probe response in any region in the Saturnian system. Naturally, this works well also when there are only two, or one, (significant) electron population(s) present. In Figure 5.6 below, we see the analysis fitting a three component curve.

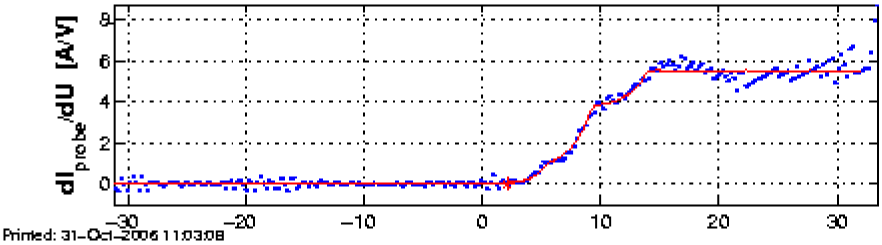

Figure 5.6: The gradient of a Langmuir probe bias voltage sweep from the Cassini spacecraft, showing the three electron component curve fit of the data during a Titan passage.

5.5.2 Output Parameters

We have the theoretical equations (5.5) and (5.6) for $U_\mathrm{B} + V_\mathrm{float} > 0$ and $U_\mathrm{B} + V_\mathrm{float} < 0$ respectively, where

$$I_{\mathrm{i}0} = -A_\mathrm{LP}\, n_\mathrm{i}\, q_\mathrm{i} \sqrt{\frac{v_\mathrm{i}^2}{16} + \frac{k_\mathrm{B}\, T_\mathrm{i}}{2\pi\, m_\mathrm{i}}} \tag{5.21a}$$

$$\chi_\mathrm{i} = \frac{q_\mathrm{i}\,(U_\mathrm{B} + V_\mathrm{float})}{\frac{m_\mathrm{i}\, v_\mathrm{i}^2}{2} + k_\mathrm{B}\, T_\mathrm{i}} \tag{5.21b}$$

and

$$I_{\mathrm{e}0} = -A_\mathrm{LP}\, n_\mathrm{e}\, q_\mathrm{e} \sqrt{\frac{k_\mathrm{B}\, T_\mathrm{e}}{2\pi\, m_\mathrm{e}}} \tag{5.22a}$$

$$\chi_\mathrm{e} = \frac{q_\mathrm{e}\,(U_\mathrm{B} + V_\mathrm{float})}{k_\mathrm{B}\, T_\mathrm{e}} \tag{5.22b}$$

Let $U = U_\mathrm{B} + V_\mathrm{float}$. The analysis does a curve fit of each voltage sweep in a least squared sense according to

$$U > 0: \qquad I_+ = c\,(1 + d\,U) + a\,\exp(-\frac{b}{a}\,U) \tag{5.23a}$$

$$U < 0: \qquad I_- = a - b\,U + c\,\exp(d\,U) + f \tag{5.23b}$$

We are, in this report, interested only in the ion side ($U < 0$), where $I_\mathrm{e} \ll I_\mathrm{i}$, so (5.23b) becomes

$$I_- = a - b\,U + f \tag{5.24}$$

By identifying the parameters we see that a corresponds to a *DC-level* and b corresponds to the *slope* of the U-I characteristic on the ion side; f represents photoelectrons. However, since photoelectrons are also a DC-level they cannot immediately be distinguished from the random current (which would be a), so the analysis instead gives as output parameters b and m, where

$$m = I_- + b\,U_\mathrm{B} \tag{5.25}$$

which can be rewritten into

$$m = a + f - b\,V_\mathrm{float} \tag{5.26}$$

Thus, m represents the mean offset of the points of the sweep from the (fitted) slope of the U-I characteristic on the ion side. Both b and m are extremely well determined (in fact, the best determined paramaters we have from the probe) which make them a very good starting point for deriving other parameters from. Knowing b and m, we can rewrite (5.26) as

$$af = a + f = m + b\,V_\mathrm{float} \tag{5.27}$$

which gives us the parameter af; the single most important parameter for the study in this report. It is the combination of the ion current and the photoelectron current. This is the parameter that needs to be corrected for the photoelectrons, so that the pure ion current can be obtained and further analysis conducted from there on.

6

Photoelectrons & Spacecraft Attitude

6.1 What Are Photoelectrons?

Photoelectrons are electrons emitted from a surface when it is illuminated by light. Photons incident upon a surface will – if the frequency of the radiation is above a threshold frequency specific to the type of surface and material – be absorbed and give rise to a current. The energy carried by the photon, $E = h\,\nu$, is absorbed by an electron, by conservation of energy, and the electron can then overcome the electrostatic barrier of the material and escape. Since the energy from a photon can be absorbed by only one electron, it follows logically that a single photon can only cause the ejection of a single electron. The above described effect is known as the *photoelectric effect*, and this is why the emitted electrons are called photoelectrons. An illustration of the photoelectric effect can be seen in Figure 6.1

The primary source driving the generation of photoelectrons on spacecraft in space is UV (or, more common, EUV) radiation (light) from the Sun. For a deeper understanding of what parts of the solar spectrum are more, or less, involved in the creation of photoelectrons, and what part different materials play, the reader is encouraged to read [Winkler, 2007].

6.2 Photoelectron Current

6.2.1 Probe Potential

When the Langmuir probe is sunlit, it will emit photoelectrons due to the photoelectric effect described above. The flux of photoelectrons leaving the surface is directly related to the potential of the probe, and the energies of escaping photoelectrons. Depending on the probe potential, $U = U_{\mathrm{B}} + V_{\mathrm{float}}$ as before, with regard to the surrounding plasma, we get two cases for the photoelectrons as well. On the electron side (that is, for a positive relative potential), lower-energy photoelectrons emitted may find themselves returning

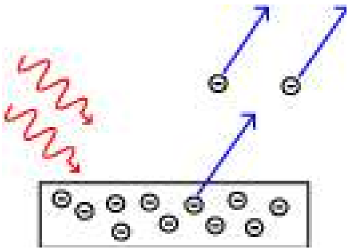

Figure 6.1: Small sketch showing the photoelectric effect. Illustration from Wikipedia.

to the probe, whilst those with a high enough energy to overcome the barrier will escape and give rise to a photoelectron current contribution. On the ion side however, all photoelectrons being emitted from the probe can (and will) escape, leading to a photoelectron current that is saturated at a constant value

$$I_{\mathrm{ph}} = I^0_{\mathrm{ph}} = A_{\mathrm{p}}\, j^0_{\mathrm{ph}} \qquad U < 0 \tag{6.1}$$

where j^0_{ph} is the photoelectron current density[1], which is estimated from satellite data. $A_{\mathrm{p}} = \pi\, r_{\mathrm{p}}^2$ is the projected area of the probe to the Sun.

It is worthwhile to note here, that regardless of the two cases above, the photoelectric effect will always give rise to a *negative* current contribution. Negative, because it is a current *to* the probe, and we define currents *away* from the probe as being positive.

6.2.2 Plasma Density

When dealing with photoelectrons, not only do we need to treat the cases of positive or negative U separately, but we must also distinguish between two cases regarding plasma density; namely dense and tenuous plasma. In a dense plasma, such as the inner magnetosphere of Saturn or the ionosphere of Titan, the currents to the probe are totally dominated by I_{i} and I_{e}, in which case I_{ph} is negligible by comparison.

On the other hand, in a tenuous plasma – e.g. a (outer) magnetospheric plasma or solar wind – the plasma density is often very low. This leads to an ion current which is so small that I_{ph} becomes significant and must be taken into account on the ion side. Here, I_{ph} can also be used to estimate the Solar EUV flux (using equation (6.2)), which is done in [Winkler, 2007] and [Isaksson, 2005].

One can here also note that, if the probe is in a magnetospheric plasma at $U = 0$, it will obtain a *positive* potential from the photoelectric effect. This is easy to understand since electrons are escaping, taking a negative charge away with them, thus leaving the source more positive.

---

[1] Usually in the range of about 1.5–8 nA cm^{-2} near Earth, see e.g. Laakso et al. [1995] (At Saturn, this is about 90 times less).

6.2.3 Spacecraft Source

The theory for the photoelectric effect, as it applies to objects in space, says that any sunlit object will emit photoelectrons. This, of course, holds true for the spacecraft itself as well. However, the spacecraft body is normally not charged with a bias potential, which means that the photoelectric effect will here cause it to obtain a positive charge, in a tenuous plasma. Thus, some photoelectrons can – in this case – escape and, since the body of the spacecraft is most often quite large, this means that there is a huge amount of photoelectrons escaping. One can look at this as the satellite being surrounded by a large sunward oriented cloud of photoelectrons (see [Cully et al., 2007]).

The escaping photoelectrons from the spacecraft body can easily interfere with nearby instruments by giving rise to a – here *positive* – photoelectron current contribution. This is yet another reason why instruments such as the Langmuir probe are mounted on booms that extend away from the rest of the spacecraft. The further away from the spacecraft body, the smaller the amount of photoelectrons from the body hitting the instrument, and thus the smaller the photoelectron current contribution. To further minimise this so called *photoelectron conduction current*, i.e. the current flowing directly from satellite to probe (and not via the ambient plasma), negatively biased guards are often attached along the booms between probe and satellite, which naturally repel electrons.

On Cassini, however, there are no real guards on the boom. Instead, there is the solution of a stub (see Figure 5.5), which is used to separate the probe from the boom; both electrically and spatially. The stub is given the same potential as the probe, which means that photoelectrons from the spacecraft can severely affect the probe current, on the electron side in a tenuous plasma.

6.3 Photoelectron Current Variation

The photoelectron current can, in a more general form (see [Brace et al., 1988]), be written as

$$I_{\mathrm{ph}} = e\,A_{\mathrm{p}} \int\limits_{0}^{\lambda_{\mathrm{T}} < 220\ \mathrm{nm}} \Phi(\lambda)\,Y(\lambda)\,d\lambda \tag{6.2}$$

where e is the electron charge, A_{p} the projected probe area as before, $\Phi(\lambda)$ is the solar emission spectrum flux, $Y(\lambda)$ is the photoelectron yield function[2] and λ_{T} is the threshold wavelength. As can be seen from this equation, the photoelectron current is all but constant apart from the variation in the solar flux. The yield function, $Y(\lambda)$, is a property that depends on the material and coating – as well as their degradation – for the surface (spacecraft or probe).

---

[2] For a more in-depth treatment of several yield functions variation over wavelength for different materials, and how it relates to the solar flux at different wavelengths, see [Winkler, 2007]. See also [Westerberg, 2007] for Cassini-specific coverage of this.

6.3.1 Solar Flux Variation

Winkler [2007] mentions three distinct periodic variations in the solar flux; the shortest of which is a 27-day period originating from the Sun's synodic rotation[3], in which the photosaturation current variation is on the order of ~5 %. However, with the Cassini Langmuir probe in the Saturnian system, variations in solar flux of ~10–12 % have been observed [Isaksson, 2005], related to solar synodic rotation.

With the photoelectron current we usually measure from the probe on Cassini being ~0.6–0.7 nA, the short-period variation in the solar flux translates to variations in the photoelectron current in the range 0.03–0.1 nA. This is rather close to the limit in the measurement capabilities of the Langmuir probe, but it is still detected. However, this area is outside the intended operating range of the probe, and the error in the readings is here unknown and can be as large as 200 %, which needs to be taken into consideration. This all means that, during a measurement period of a month or less, the solar flux can be seen as almost constant.

The other two variations mentioned in Winkler [2007] are related to the Earth's orbit around the Sun, and the 11-year solar cycle, respectively. Both of these are longer period variations which are of little consequence to the time frames involved in this study.

It is however important to note that there are non-periodic variations as well, in the solar flux. These include – among others – solar flares, coronal mass ejections and other types of solar events. Variations such as these can be very short, but still have a significant effect; variations with time periods < 1 minute, but still having amplitude variations > 100 %, have been obeserved. Such a variation is easily identified in the data though, and can then be filtered away.

6.3.2 Shadowing Effects

A much greater variation in the photoelectron current – as well as being over a much shorter time scale – is the effect of shadowing on the probe. Since the photoelectron current is proportional to the sunlit area, if part of the surface is shadowed the current will be lower. This happens for instance when the probe enters (and exits) a region of eclipse from sunlight in space. In this case, the variation is large and brief when it occurs and it can be a relatively long period of time before the next event.

Another very common cause for the probe being in shadow – and therefore for variance in photoelectron current – is varying spacecraft attitude. This is

---

[3] The synodic rotation period is the time for a fixed feature on the Sun to rotate to the same apparent position as viewed from Earth. The true rotation period is known as the sidereal rotation period, and is 25.38 days. Due to the fact that the Earth is moving along its orbit around the Sun, the Sun has to rotate a sidereal period plus a little extra to get to the same apparent position seen from the Earth.

a short period variation that is more gradual than the above case. Depending on the probe geometry, when the spacecraft orientation changes relative to the direction of the Sun, the projected area being sunlit may change. This is one of the reasons why Langmuir probes with spherical geometry are most commonly used; spherical symmetry entails a directional independence, since the projected area is the same in any direction, and is therefore insensitive to variations in photoelectron current from the probe due to spacecraft attitude.

There is, of course, the case of the probe being shadowed by the spacecraft itself, regardless of probe geometry. But on Cassini, we can see evidence of a variation in photoelectron current that is linked to spacecraft attitude (see chapter 7), but not due to Cassini itself shadowing the probe.

6.3.3 Stub Contribution

The variation with attitude we see in the photoelectron current for the Langmuir probe on Cassini, is most probably due to the *stub* between the probe and the boom (see Figure 5.5). The stub is at the same potential as the probe, and it is also giving off photoelectrons depending on its sunlit (projected) area. So, the same rules and regimes as for the probe, also apply to the stub; on the ion side, all photoelectrons from the stub escape and contributes to the total photoelectron current. What we get is a higher photoelectron current than we would normally get from the probe alone.

With the stub involved, we get a much more complex treatment of photoelectron variation with spacecraft attitude. We can no longer simplify things by relying solely on spherical symmetry for the probe; we must also take into account the shadow that may be cast on the stub by the, much larger, probe, as well as the actual decrease of projected probe area, due to the area occupied by the stub and the associated insulator.

Depending on the solar incidence angle the probe may with its shadow partially, or fully, occlude the stub, causing it to emit fewer photoelectrons. When the sunlight comes in perpendicular to the boom, both the probe and the stub are fully exposed and will emit a maximum number of photoelectrons. If instead the direction of solar incidence is parallel to the boom, or at a relatively low angle to the boom, the probe will be fully exposed while, at the same time, the stub will be completely veiled in shadow and thus not contributing to the photoelectron current.

The interested reader is encouraged to have a look at [Jacobsen, 2006, Appendix A]. Presented there is a full geometric derivation of incident sunlight upon the Cassini Langmuir probe and stub.

It is important to note that the probe and the stub are almost *electrically linked* – save for a thin insulator between them – which is why they have the same potential (within 1-2 mV). The boom, however, is electrically isolated from the stub, so its potential is different from the stub and probe; in fact, the boom is at the same potential as the spacecraft.

Another thing worth noting is that the probe and the stub are both made up of the same materials, which means that they will emit an equal number of photoelectrons per unit area, when illuminated. This in turn means that a joint treatment of the illumination of probe and stub is a purely geometric problem; all that needs to be considered is the solar incidence angle with respect to boom direction. For this, we first need the concept of *spacecraft attitude*; to understand what it is, and its involvement with the photoelectron current.

6.4 Spacecraft Attitude

Spacecraft attitude is the term used to describe how the spacecraft is oriented in space. To determine the orientation, a spacecraft has a coordinate system where one usually finds a regular cartesian system of three orthogonal coordinate axes. But in order for the spacecraft to determine its attitude and position in space, it must express its coordinates relative to some *reference system*, e.g. a coordinate system fixed in the Sun or some planet.

Explained below are some coordinate systems that come into play when working with the Cassini spacecraft. Also, a part about how this pertains to the Langmuir probe on Cassini and photoelectron generation, is included.

6.4.1 Coordinate Systems

The Cassini spacecraft itself has a coordinate system with three orthogonal axes, denoted $\mathbf{X}_{S/C}$, $\mathbf{Y}_{S/C}$ and $\mathbf{Z}_{S/C}$. How these are defined is shown below in Figure 6.2. From this figure we also see that the boom connecting the Langmuir probe is approximately aligned along the $-\mathbf{X}_{S/C}$ axis.

In order to determine the spacecraft attitude we must relate the spacecraft axes to some reference system, and for this study the *Saturn Solar Equatorial* reference system was chosen. It is a coordinate system centered in Saturn and defined in the following way:

$\mathbf{Z}_{SSQ}$ – Northward spin axis of Saturn.

$\mathbf{Y}_{SSQ}$ – $\mathbf{Z}_{SSQ} \times \mathbf{X}_{SSQ}$.

$\mathbf{X}_{SSQ}$ – In the plane spanned by $\mathbf{Z}_{SSQ}$ and the Saturn → Sun line ($\mathbf{S}$). Positive towards the Sun, and orthogonal to $\mathbf{Z}_{SSQ}$.

This coordinate system will not be fixed in space however; it will change as Saturn moves in orbit around the Sun. Because of the axial tilt, $\alpha = 26.73°$, of Saturn's spin axis to its ecliptic, the angle between the axis $\mathbf{X}_{SSQ}$ and the vector $\mathbf{S}$ will vary periodically in the interval $[-\alpha, \alpha]$ during an orbit.

Figure 6.2: The picture shows the Cassini spacecraft and some of its instruments. The spacecraft axes are defined as shown in the bottom.

Another reference system that could be used is *Saturn Solar Ecliptic*, which is also centered in Saturn, but defined in another way:

$\mathbf{Z}_{SSE}$ – Parallel to the upward normal of the Saturn orbital plane.

$\mathbf{Y}_{SSE}$ – $\mathbf{Z}_{SSE} \times \mathbf{X}_{SSE}$, meaning it is tangent to Saturn's orbit around the Sun, positive in Saturn's wake

$\mathbf{X}_{SSE}$ – Along the Saturn → Sun line, positive towards the Sun.

This reference system could perhaps have been a better choice for this study than the chosen system, SSQ. This because the incident photons from the Sun would always be along $-\mathbf{X}_{SSE}$, which would probably give a more accurate result in the photoelectron corrections. However, the difference turned out to be small; more on this in section 10.1.

6.4.2 Photoelectron Dependency

As previously discussed, the generation of photoelectrons from the Langmuir probe and its stub is highly dependent on the direction of sunlight incidence upon the probe and stub. It is therefore of great importance to develop a mathematical model for exactly how the photoelectron current depends on the attitude of the spacecraft, at any given time.

The problem is geometric in nature, and should be possible to solve both theoretically and empirically; in this report the empiric path was chosen[4]. Once a dependency model has been found, only then is it possible to apply a correction for the photoelectron current. This correction is the first step in this thesis project – a vital step in order to perform actual analysis on the pure ion data – and is the focus of the following chapter.

---

[4] An extension of the work with photoelectron current done by Westerberg [2007] will provide the theoretical solution. See also [Jacobsen, 2006, Appendix A]

7

Photoelectron Corrections

7.1 Obtaining the Dependency Model

7.1.1 How to Get the Photoelectron Data

In order to obtain a model for how the photoelectron current varies with spacecraft attitude, one must first try to suppress other varying parameters, or make sure they are constant or close to constant. For example, since the photoelectrons are not very energetic, the current they give rise to in the probe sample can easily be drowned out by the real sample being taken from the plasma. Therefore, to get an accurate reading of pure photoelectron behaviour, we have to focus on the period of an orbit when the spacecraft is out in the solar wind or outer magnetosphere. There the plasma is tenuous enough that the photoelectrons will be the dominating part of the current being sampled by the probe. We also need to filter away any spurious peaks that may be present.

7.1.2 Calculating the Angles

To get the incident angle of the photons on the Langmuir probe, the first step is to choose a reference coordinate system. For this study, the Saturn Solar Equatorial (SSQ) system was chosen.

We now need to express the three spacecraft axes of Cassini in SSQ coordinates. For this, we do a coordinate transform, where each of the three vectors $\{\mathbf{X}, \mathbf{Y}, \mathbf{Z}\}_{S/C}$ have three SSQ components, resulting in a 3×3 coordinate matrix[1].

The incident photons are assumed to be coming in along $-\mathbf{X}_{SSQ}$, and this is subsequently taken as the reference vector for the calculations. In reality this is not true; what we really have is incidence along $-\mathbf{X}_{SSE}$ (where *SSE* means Saturn-Solar Ecliptic) and the angle between these vectors varies periodically in the interval $[-26.73°, 26.73°]$ i.e. ± the axial tilt of Saturn. This, however, has little to no bearing on the correction method chosen in this work. It is

---

[1] See Terry's Cassini Utilities, http://www-pw.physics.uiowa.edu/~tfa/cassatt.html

an empirical method, making no assumptions whatsoever on the source(s) of the problem and instead using purely generic corrections, which will be shown later in this chapter.

The next step is to calculate the angles between each of these three transformed spacecraft axes and the reference vector, $\mathbf{X}_{SSQ}$. These angles are obtained from the definition of the scalar product between two vectors

$$\mathbf{u} \cdot \mathbf{v} = |\mathbf{u}||\mathbf{v}| \cos \alpha \tag{7.1}$$

where α is the angle between the vectors. Since the Langmuir probe – and its stub – is aligned parallel to the $-\mathbf{X}_{S/C}$ axis (not really true either; there is an unknown angle between them [Jacobsen, 2006], but this is also irrelevant, for the reason mentioned above), we are really only interested in the angle between that axis and the reference vector. And since it was transformed as

$$\mathbf{X}_{S/C} = (a\,\hat{\mathbf{x}}_{SSQ},\, b\,\hat{\mathbf{y}}_{SSQ},\, c\,\hat{\mathbf{z}}_{SSQ})$$

the result of the scalar product will be $-a$, i.e. only the first component of the transformed spacecraft vector. This takes care of the left hand side of equation 7.1. Now, for the right hand side of the equation, both vectors are normalised to unit length and, therefore, the right hand side is reduced to $\cos \alpha$. This means that the angle we seek is obtained from

$$\alpha = \arccos(-a) \tag{7.2}$$

and similarly for angles β and γ for $\mathbf{Y}_{S/C}$ and $\mathbf{Z}_{S/C}$, respectively.

7.1.3 Angular Dependency

Now that we have calculated the angle of photon incidence it is time to plot the sampled current as a function of time, and the three angles versus time as well, to look for any correspondence in the variation of the current and a variation in one (or more) of the angles, over time. For this to give an accurate representation of the photoelectron variations with attitude, only the data points mentioned in section 7.1.1 should be used in analysis, modeling and correction of photoelectrons.

As can be seen in Figure 7.1 there appears to be a connection between angular variations in the $\mathbf{X}_{S/C}$ axis and the variations in the current. This is not at all surprising, considering the stub connecting the Langmuir probe is approximately aligned along that axis. Also, at first glance, there appears to be no correlation between variations in β, γ and variations in the current, but this needs to be checked in more detail in order to be certain. To do this we instead plot the current against each of the three angles, in order to see if there really is a dependency and, if so, exactly what it looks like.

From the Figures 7.2–7.4 it can be seen that there is no dependency on neither β nor γ. The dependency on α, however, can be clearly seen here. It takes the general form of an *arctan* curve.

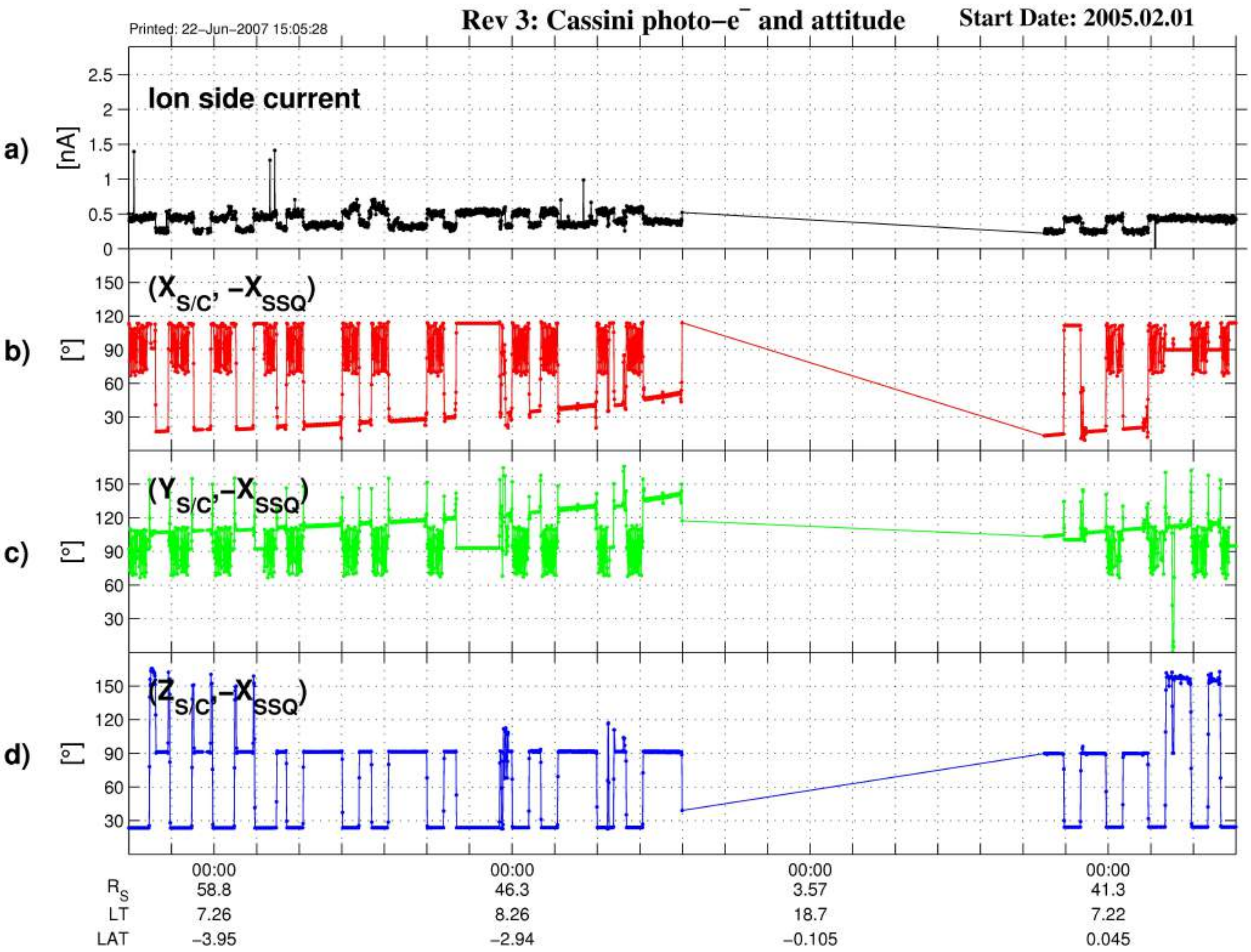

Figure 7.1: Plot showing the variation of the sampled current (panel a), as well as the three angles α (panel b), β (panel c) and γ (panel d), over time.

7.2 Correcting for the Photoelectrons

7.2.1 Curve Fitting

The first step in correcting the current for the photoelectrons is to fit a curve to the data using the obtained dependency model. Since we now know that the general behaviour of the dependency is an *arctan* shape, we construct a generic *arctan* function in the form of

$$y = k_y \arctan(k_x x + \phi) + m \tag{7.3}$$

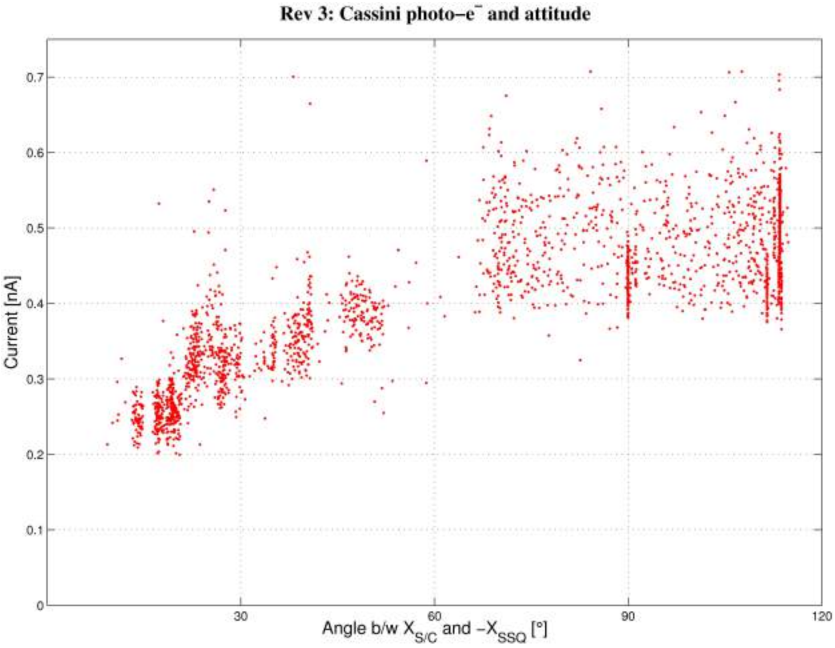

Figure 7.2: The ion side current plotted as a function of α.

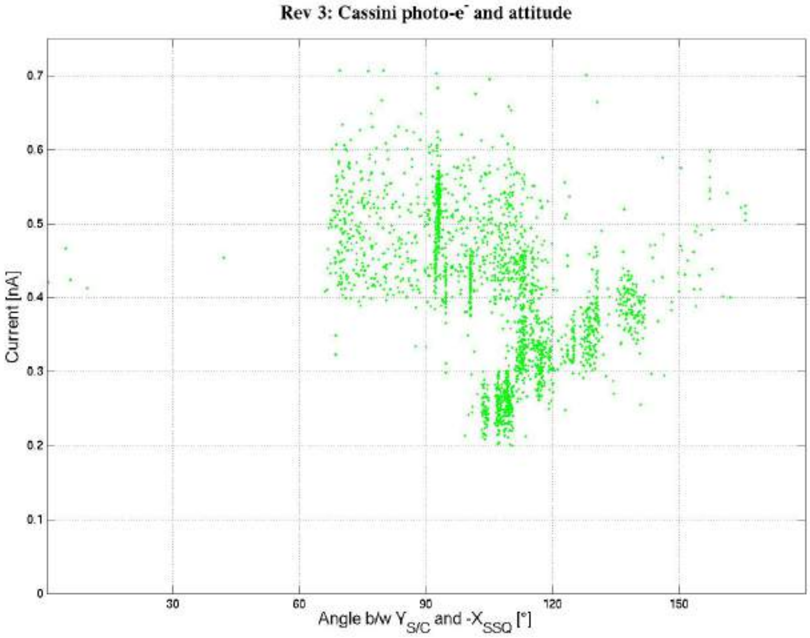

Figure 7.3: The ion side current plotted as a function of β.

where x is the angle, k_x, k_y are the scale factors in x, y direction respectively, ϕ is the phase shift of the angle and m is the y-shift or, in this case, the DC

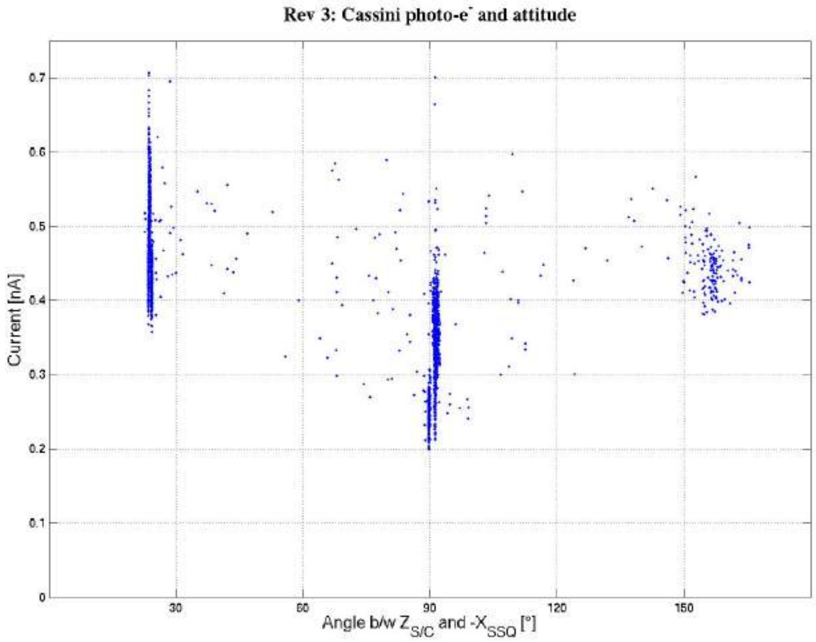

Figure 7.4: The ion side current plotted as a function of γ.

level.

The curve fitting of the function is done in a least squared sense using the MATLAB function `lsqcurvefit`. Since x and y are the actual data points we want to fit a curve to, this leaves four parameters for the function to determine. To get a faster convergence and a more accurate result – or even convergence at all – we need a fair initial guess for all parameters. As seen in Figure 7.2 the angle varies between 0° and 120°, so in order to get a full range (360°), a factor 3 should be used. This means that the curve will also be phase shifted 180°. The DC level is easily seen, being the approximate center of the data points, around 0.45 nA. The last parameter should bring the curve from $[-\pi, \pi] \rightarrow [-1, 1]$. Therefore, starting guesses for the curve fitting are chosen as:

$$k_x = 3$$

$$k_y = \frac{1}{\pi}$$

$$\phi = -180^\circ$$

$$m = 0.45$$

These four parameters are adjusted by `lsqcurvefit` in order to best fit the data in a least squared sense. The four corrected coefficients being output by the function are next used as input for the function `feval`, along with the angle data in order to get the actual fitted curve. See Figure 7.5.

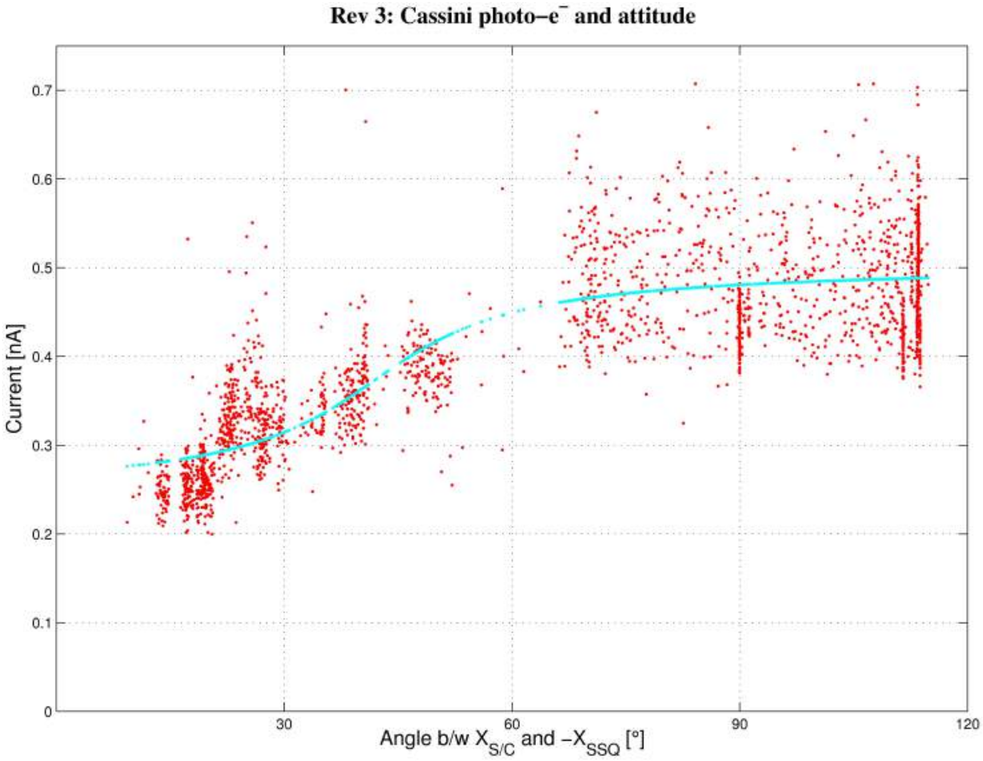

Figure 7.5: Current versus α, with arctan curve fit overlayed.

7.2.2 Correcting the Current

Now that we have a curve fit that approximates the photoelectron behaviour, it is time to correct for it in the current. The fitted curve output from `feval` gives us the data points for the photoelectron current, for each measured point in time during the orbit. To apply the correction, we simply subtract this from the current measured by the probe. This is applied not only in the region out in the solar wind, but over the whole orbit, with the exception of certain eclipse regions which are left unchanged. Below are figures showing an example of the correction for an orbit, both before and after.

From Figures 7.6–7.7 it can be seen that the current is now smooth, and that the variations have gone down and are now on the order of 0.1 nA.

In order to validate this correction process, and to check that it did not introduce any angular dependencies in β nor γ, the current is plotted both before and after correction against all three angles (see Figure 7.8). As can be seen in the second column of this figure, the correction of the current only for dependency on α has affected the current as a function of β and γ as well. The current is now centered around zero for all three angles, which shows that there really was no angular dependency on β or γ. Thus, the assumption that the current only has an arctan shaped dependency on α is valid.

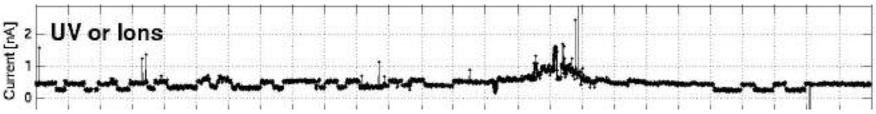

Figure 7.6: The uncorrected ion current for Rev3.

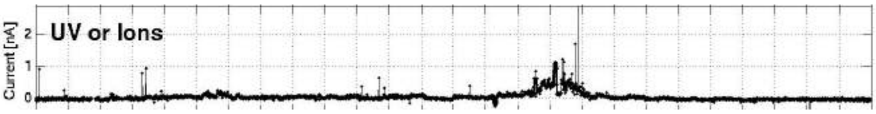

Figure 7.7: The ion current for Rev3, corrected for photoelectrons.

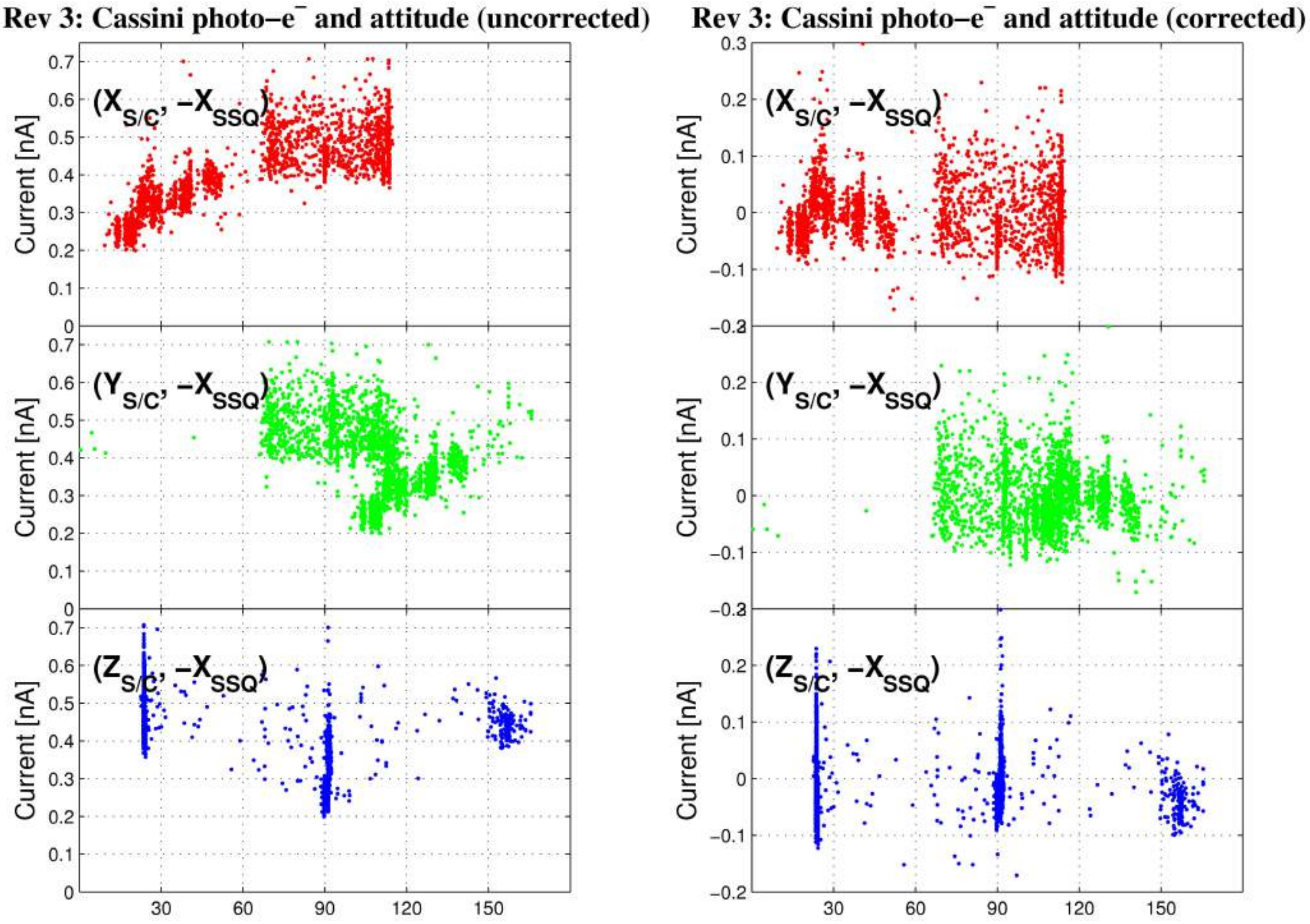

Figure 7.8: The left hand side shows the uncorrected – and the right hand side the corrected – current as a function of all three angles.

8

Plasma Ion Speed Calculations

8.1 The Ion Side Current

On the ion side, i.e. for negative U, the total current sampled by the probe is given by

$$I_- = \sum_{\substack{ion\\species}} \left(q_i n_i A_{\mathrm{LP}} \sqrt{\frac{v_i^2}{16} + \frac{e\,T_i[\mathrm{eV}]}{2\pi\, m_i}} \left(1 + \frac{U_{\mathrm{B}} + V_{\mathrm{float}}}{\frac{m_i v_i^2}{2e} + T_i} \right) \right) + \tag{8.1}$$

$$+ I_{\mathrm{ph}} + I_{\mathrm{dust}} + I^*_{\mathrm{energetic}}$$

where I_{ph} is the photoelectron current from the probe and the stub, I_{dust} is the current generated by dust particles hitting the probe surface and $I^*_{\mathrm{energetic}}$ is the current from high energetic particles ($>$ keV). Other parameters as defined in chapter 5.

Equation (8.1) can be rewritten in a simpler form as

$$I_- = \sum_{\substack{ion\\species}} \left(I_{i0} \left(1 + \frac{1}{W_i} (U_{\mathrm{B}} + V_{\mathrm{float}}) \right) \right) + I_{\mathrm{ph}} + I_{\mathrm{dust}} + I^*_{\mathrm{energetic}} \tag{8.2}$$

where W_{i} is the ion energy and I_{i0} is called the *random current* for the ions. I_{ph}, I_{dust} and $I^*_{\mathrm{energetic}}$ are all assumed to be constant; I_{ph} was corrected for in section 7.2, and the other two are assumed to be small (negligible compared to the first term, see section 5.3.3).

We also make some further assumptions:

- There is only one ion species present
- The ions are singly charged (i.e. only ionised one time)
- That $\frac{m_\mathrm{i}\, v_\mathrm{i}^2}{2e} \gg T_\mathrm{i}$ [eV] i.e. that ram dominates
- Quasineutrality ($n_\mathrm{e} \approx n_\mathrm{i}$)

which mean that the equation now becomes

$$I_- = e\, n_\mathrm{i}\, A_\mathrm{LP} \frac{v_\mathrm{i}}{4} \left(1 + \frac{2e}{m_\mathrm{i}\, v_\mathrm{i}^2}(U_\mathrm{B} + V_\mathrm{float})\right) \tag{8.3}$$

8.2 Obtaining the Ion Speed

There are two ways of deriving v_i. One is from the DC level of the current, using all the assumptions in the previous section. The other is to derive it from the slope of the current-voltage characteristic.

8.2.1 Ion Speed from DC Level

The sweep analysis fits a curve to the data, from which one recieves parameters a and b according to

$$I_- = a - b(U_\mathrm{B} + V_\mathrm{float}) \tag{8.4}$$

where one can see that $a = -I_{\mathrm{i}0}$ and $b = \frac{dI}{dU}$. Identification gives

$$a = e\, n_\mathrm{i}\, v_\mathrm{i}\, \pi r_\mathrm{LP}^2 \propto n_\mathrm{i}\, v_i$$

which is the *flux* of ions to the probe. With the assumption of quasineutrality, we get

$$v_\mathrm{i} = \frac{I_{\mathrm{i}0}}{n_\mathrm{e}\, e\, \pi r_\mathrm{LP}^2} \equiv v_{\mathrm{i},I_0} \tag{8.5}$$

8.2.2 Ion Speed from Slope

We can see from comparing equations (8.2) and (8.4) that

$$W_\mathrm{i} = \frac{a}{b} = \frac{m_\mathrm{i}\, v_\mathrm{i}^2}{2e} \tag{8.6}$$

under the assumption that

$$\frac{m_\mathrm{i}\, v_\mathrm{i}^2}{2e} \gg T_\mathrm{i}\, [\mathrm{eV}]$$

which is to say that ram dominates.

In order to get the ion speed from equation (8.6) we must make some assumption about the *ion mass*, which means we have to estimate what type of ion species is present. By assuming either hydrogen ions or water ions, that is assuming an ion mass of either $m_\mathrm{i} = 1\,\mathrm{amu}$ or $m_\mathrm{i} = 18\,\mathrm{amu}$ we get two ion speeds

$$v_{\mathrm{i,H^+}} = \sqrt{\frac{2e}{m_\mathrm{H}}\, I_{\mathrm{i0}}\, \frac{dU}{dI}}$$

$$v_{\mathrm{i,H_2O^+}} = \sqrt{\frac{2e}{18 m_\mathrm{H}}\, I_{\mathrm{i0}}\, \frac{dU}{dI}}$$

which will serve as upper and lower boundaries, respectively, for the ion speed.

8.3 Ion Speed Comparison

The speed v_{i,I_0} can now be compared with the ion speeds derived from the slope of the current-voltage characteristic. The ram speed v_{i,I_0} should lie between $v_{\mathrm{i,H^+}}$ and $v_{\mathrm{i,H_2O^+}}$ over the whole orbit; out in the outer magnetosphere or in the solar wind it should coincide with $v_{\mathrm{i,H^+}}$, and in the inner magnetosphere it should be close to $v_{\mathrm{i,H_2O^+}}$. The following figure illustrates how the ion speed varies over the orbit. From Figure 8.1, depicting a Saturn passage within 10 $\mathrm{R_S}$ during high resolution mode, it can be clearly seen that v_{i,I_0} goes down to $v_{\mathrm{i,H_2O^+}}$ close to Saturn. This indicates that H_2O^+ ions are the dominating species in this region.

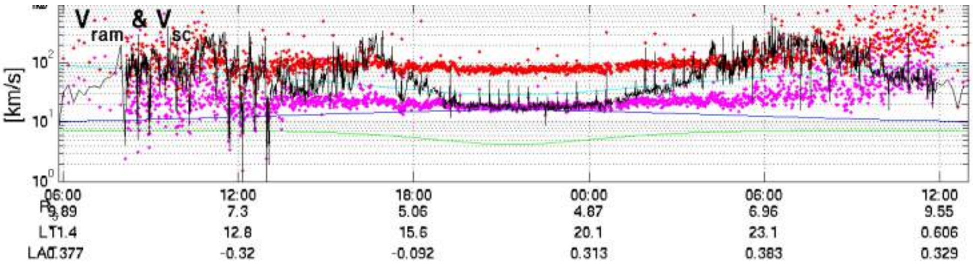

Figure 8.1: Speeds as seen in the spacecraft frame for Rev19 within 10 R_S*. The black is the ion speed from the DC level; the red and magenta the ion speed from the slope, for* H^+ *and* H_2O^+*, respectively. The cyan line is the co-rotation speed, the green is the Keplerian speed and the blue is the spacecraft speed in Saturn's frame of reference.*

The calculation of v_{i,I_0} is a necessary step in the investigation of the ratio of ions that are being trapped by dust particles. The intimation that the ion speed is decreased almost to Keplerian speed in the inner part of the E-ring, is a good early indicator for a large extent of plasma–dust interaction going on.

9

Dust Ratio Estimations

9.1 Regions of Interest

We are interested in examining the dust—plasma interaction in certain regions of high interest in the E-ring; e.g. the flybys of the icy moons and, possibly, their wake as well. We want to investigate whether a higher number density of dust particles gives rise to a higher ratio of dust—plasma coupling.

With that in mind, mapping the fraction of ions in the plasma that were coupled to dust, compared to the total number of ions in the plasma, was begun; both as a function of space, or rather, as a function of (radial) distance from Saturn (in $\mathrm{R_S}$).

To look at regions of interest, a total of eight orbits were chosen, for various reasons, and these are listed in Table 9.1 below. Enceladus has been thought of as the primary source for ion and icy dust particle production in the E-ring for quite a while. However, recently suspicions have been raised that Tethys and perhaps both Dione and Rhea are also contributing to the E-ring. By observing dust concentrations in the orbits of these moons, as well as what happens during close flybys, the hope is to gain knowledge of not only the dust–plasma interaction and how it relates to varying dust concentration, but

Orbit (Rev #)	Reason for interest
3	Enceladus flyby (E0)
4	Enceladus flyby (E1)
11	Enceladus flyby (E2)
15	Hyperion flyby (H1)
16	Dione flyby (D1)
17	First interferometry measurement
18	Rhea flyby (R1)
19	16-hour continuous high-resolution sweep

Table 9.1: Orbits of interest chosen for dust ratio estimations.

also what or which process(es) fuel the production of particles in the E-ring.

9.2 Approximating the Ion Mass

The first step in our goal to find the ratio of ions that are trapped by dust particles, is to somehow estimate the mass of these ions. This is necessary since the ion mass comes into play in the thermal energy, which is part of the equations involved (see e.g. equation (8.1)).

In estimating the ion mass, we know we have two boundaries; in the inner magnetosphere (and thus the inner part of the E-ring) we should predominantly have water ions, while in the outermost part of the E-ring and further out, hydrogen ions should dominate. What this means is, that somewhere in the E-ring we should have some form of transition curve for the ion mass, between the limits of water ions and hydrogen ions.

To get an idea of what this transition looks like, we use the following formula to calculate m_i (from equation (8.2)):

$$m_\mathrm{i} = \frac{2e\,W_\mathrm{i}}{v_{\mathrm{i},I_0}^2} \tag{9.1}$$

The ion mass is calculated for the 8 orbits which have been chosen. Now, we restrict ourselves to distances < 10 $\mathrm{R_S}$ and plot m_i as a function of $\mathrm{R_S}$. If we plot this data for all 8 orbits into the same plot, we get the result shown in Figure 9.1 below. From this, we can see that there is a clear transition somewhere around 5-7 $\mathrm{R_S}$. We can also see that further out there is a huge spread in a region which should be dominated by $\mathrm{H^+}$ and $\mathrm{H_2^+}$ ions, and the reason for this is unclear (most probably data errors due to photoelectron clouds around the spacecraft).

By drawing in the transition slope which has presented itself in the figure, and connecting it with the two boundaries, we obtain the result shown in Figure 9.2 below. Here we can see that we actually get two distinct slopes. The dashed slope comes from the Dione flyby in Rev16, which suggests that there is something additional going on there. This may indicate a source of water from Dione! Disregarding that orbit, all the others follow the behaviour of the solid slope.

We now use the following logarithmic equation

$$R_\mathrm{S} = C_1 \,\log_{10} m_\mathrm{i} + C_2 \tag{9.2}$$

to obtain a formula for the approximation of m_i. From the endpoints of the slope (marked in dashed green), the boundary conditions for use in the equation is obtained from

$$\left\{ \begin{array}{rcl} 5 & = & C_1 \,\log_{10}(18) + C_2 \\ 6.7 & = & C_1 \,\log_{10}(1) + C_2 \end{array} \right.$$

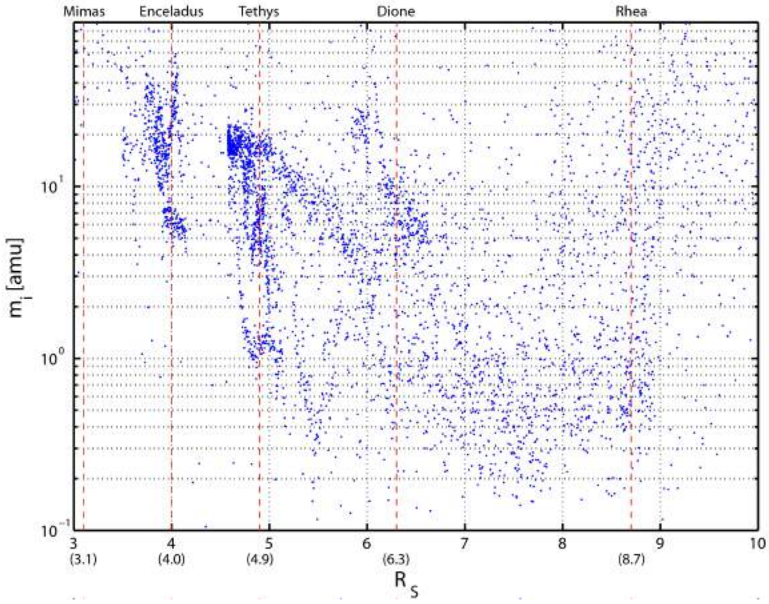

Figure 9.1: A plot showing the ion mass as a function of distance from Saturn, for the eight orbits in Table 9.1. The dashed red lines show where the orbits of the icy moons in the E-ring are located.

Solving this equation system, we obtain the final result:

$$m_{\mathrm{i}} = \begin{cases} 18 & , \quad R_{\mathrm{S}} \leq 5 \\ 1 & , \quad R_{\mathrm{S}} \geq 6.7 \\ 10^{\left(\frac{6.7-R_{\mathrm{S}}}{1.35}\right)} & , \quad 5 < R_{\mathrm{S}} < 6.7 \end{cases} \tag{9.3}$$

Now, we have a mathematical model for m_{i} as a function of R_{S} and can move on to the next stage.

9.3 Coordinate Transformations

Here we come to a slight problem; namely the dilemma of different variables being defined in different reference frames. All measurements of course take place on the spacecraft, so therefore all those variables are in the spacecraft frame. Among the variables are the spacecraft speed, expressed in three components $v_{\mathrm{sc,x}}$, $v_{\mathrm{sc,y}}$ and $v_{\mathrm{sc,z}}$ for each of the three SSQ-axes, respectively.

We are working under the assumption that there are two ion populations; one moving with co-rotational velocity $\mathbf{v}_{\mathrm{rot}}$ under the influence of Saturns magnetic field, and one moving with Keplerian velocity $\mathbf{v}_{\mathrm{grav}}$ under gravitational influence. These velocities, however, are in the Saturn reference frame. To be able to calculate the fraction of ions moving at the different speeds, one

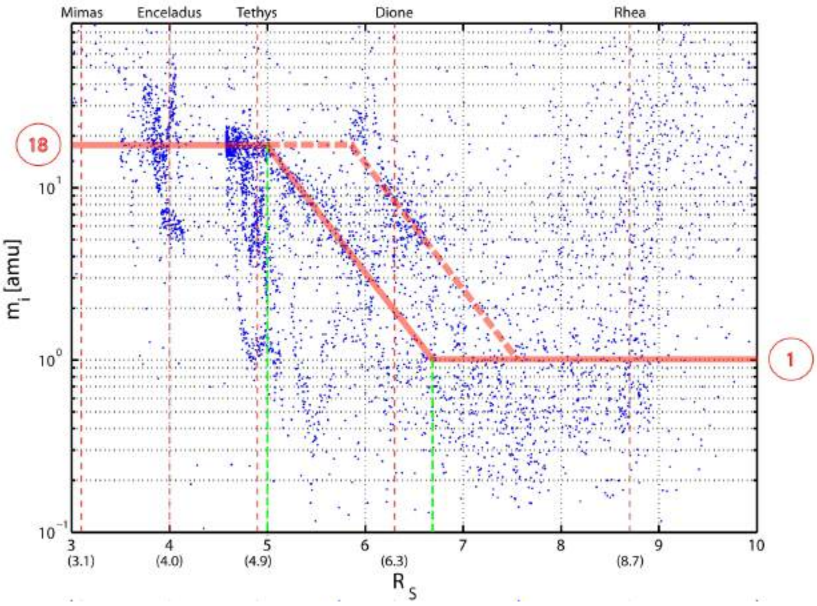

Figure 9.2: Same as Figure 9.1 but with a mathematical model for the ion mass as a function of distance from Saturn overlayed on the data points. The dashed green lines mark the endpoints of the slope and the breakpoints of the model curve.

must do the calculation in one system of reference – meaning all parameters must be in the same reference frame. Therefore, these two velocities must be transformed from the Saturn reference frame to the spacecraft reference frame.

To do this, we first make the transformation from a cartesian coordinate system to a cylindrical coordinate system, fixed in Saturn. This is expressed, in general form, as

$$\begin{bmatrix} v_\mathrm{r} \\ v_\theta \\ v_\mathrm{z} \end{bmatrix} = M \begin{bmatrix} v_\mathrm{x} \\ v_\mathrm{y} \\ v_\mathrm{z} \end{bmatrix} \tag{9.4}$$

where M is the *coordinate transformation matrix* from cartesian to polar coordinates, and is defined as

$$M = \begin{bmatrix} \cos\theta & \sin\theta & 0 \\ -\sin\theta & \cos\theta & 0 \\ 0 & 0 & 1 \end{bmatrix} \tag{9.5}$$

What we thus get is the following set of equations

$$v_\mathrm{sc,r} = v_\mathrm{sc,x}\,\cos\theta + v_\mathrm{sc,y}\,\sin\theta \tag{9.6a}$$

$$v_{\mathrm{sc},\theta} = -v_\mathrm{sc,x}\,\sin\theta + v_\mathrm{sc,y}\,\cos\theta \tag{9.6b}$$

$$v_\mathrm{sc,z} = v_\mathrm{sc,z} \tag{9.6c}$$

What now needs to be done is to transform $\mathbf{v}_{\mathrm{grav}}$ and $\mathbf{v}_{\mathrm{rot}}$ to the spacecraft frame. We know (or, at least, it is a fairly safe assumption) that:

$$\mathbf{v}_{\mathrm{grav}} = v_{\mathrm{grav}}\,\hat{\theta} \tag{9.7a}$$

$$\mathbf{v}_{\mathrm{rot}} = v_{\mathrm{rot}}\,\hat{\theta} \tag{9.7b}$$

To express these velocities in the spacecraft frame – which is to say, obtain the velocites observed from the spacecraft – the velocity of the spacecraft needs to be subtracted from each of these, respectively. We denote these velocities as Δv_{grav} and Δv_{rot} respectively, and we obtain

$$\Delta v_{\mathrm{grav}}^2 = |v_{\mathrm{grav}} - v_{\mathrm{sc},\theta}|^2 + v_{\mathrm{sc,r}}^2 + v_{\mathrm{sc,z}}^2 \tag{9.8a}$$

$$\Delta v_{\mathrm{rot}}^2 = |v_{\mathrm{rot}} - v_{\mathrm{sc},\theta}|^2 + v_{\mathrm{sc,r}}^2 + v_{\mathrm{sc,z}}^2 \tag{9.8b}$$

and with these two new parameters, everything is now expressed in the same frame of reference.

9.4 Calculating $n_{\mathrm{i,dust}}$

We start with the OML expression for current sampling by the Langmuir probe on the ion side ($U < 0$), neglecting electron contributions

$$I_{-} = \sum_{\substack{ion\\species}} \left(q_{\mathrm{i}} n_{\mathrm{i}} A_{\mathrm{LP}} \sqrt{\frac{v_{\mathrm{i}}^2}{16} + \frac{e\,T_{\mathrm{i}}[\mathrm{eV}]}{2\pi\, m_{\mathrm{i}}}} \left(1 + \frac{U_{\mathrm{B}} + V_{\mathrm{float}}}{\frac{m_{\mathrm{i}} v_{\mathrm{i}}^2}{2e} + T_{\mathrm{i}}} \right) \right) + \tag{9.9}$$

$$+\, I_{\mathrm{ph}} + I_{\mathrm{dust}} + I_{\mathrm{energetic}}^{*}$$

where we have previously determined that

$$\begin{cases} I_{\mathrm{ph}} & = \mathrm{const} \\ I_{\mathrm{dust}} & = \mathrm{const} \\ I_{\mathrm{energetic}}^{*} & = \mathrm{const} \end{cases}$$

and

$$A_{\mathrm{LP}} = 4\pi\, r_{\mathrm{LP}}^2 = \mathrm{const}$$

as before. Also, note that all speeds in equation (9.9) are squared, which means that they will be strictly positive in the calculated end result, i.e. $v_{\mathrm{i}} = |v_{\mathrm{i}}| \geq 0$.

Next, we consider the *gradient* of the current response, assuming two singly charged ion populations. If we do this, we will get rid of the other (constant) current terms.

$$\begin{aligned}\frac{dI}{dU} &= e\,A_{\mathrm{LP}}\left(\frac{n_{\mathrm{grav}}\sqrt{\frac{v_{\mathrm{grav}}^2}{16}+\frac{e\,T_{\mathrm{grav}}}{2\pi\,m_{\mathrm{i}}}}}{\frac{m_{\mathrm{i}}\,v_{\mathrm{grav}}^2}{2e}+T_{\mathrm{grav}}}+\frac{n_{\mathrm{rot}}\sqrt{\frac{v_{\mathrm{rot}}^2}{16}+\frac{e\,T_{\mathrm{rot}}}{2\pi\,m_{\mathrm{i}}}}}{\frac{m_{\mathrm{i}}\,v_{\mathrm{rot}}^2}{2e}+T_{\mathrm{rot}}}\right)\\ &= \frac{2e^2\,A_{\mathrm{LP}}}{m_{\mathrm{i}}}\left(\frac{n_{\mathrm{grav}}\sqrt{\frac{v_{\mathrm{grav}}^2}{16}+\frac{e\,T_{\mathrm{grav}}}{2\pi\,m_{\mathrm{i}}}}}{v_{\mathrm{grav}}^2+\frac{2e}{mi}T_{\mathrm{grav}}}+\frac{n_{\mathrm{rot}}\sqrt{\frac{v_{\mathrm{rot}}^2}{16}+\frac{e\,T_{\mathrm{rot}}}{2\pi\,m_{\mathrm{i}}}}}{v_{\mathrm{rot}}^2+\frac{2e}{mi}T_{\mathrm{rot}}}\right)\end{aligned} \tag{9.10}$$

The watchful reader also notices that $\frac{dI}{dU} = |b|$, the slope as before, which is a very accurately determined parameter.

Now, we consider quasineutrality (for singly charged ion populations n_{grav} and n_{rot}):

$$e\,(n_{\mathrm{grav}} + n_{\mathrm{rot}}) = q_{\mathrm{d}}\,n_{\mathrm{d}} + e\,n_{\mathrm{e}} \tag{9.11a}$$

$$\iff n_{\mathrm{grav}} + n_{\mathrm{rot}} = \left(\frac{q_{\mathrm{d}}}{e}\right) n_{\mathrm{d}} + n_{\mathrm{e}} \tag{9.11b}$$

$$\iff n_{\mathrm{rot}} = \left(\frac{q_{\mathrm{d}}}{e}\right) n_{\mathrm{d}} + n_{\mathrm{e}} - n_{\mathrm{grav}} \tag{9.11c}$$

where n_{e} is the total electron density, n_{d} the total dust density, n_{grav} is the ion population which is trapped by dust, n_{rot} is the ion population which is co-rotating and q_{d} is the dust charge.

However, we can assume that the trapped ion population can balance the negative charges on the dust. What remain are

$$n_{\mathrm{rot}} \approx n_{\mathrm{e}} \tag{9.12a}$$

$$n_{\mathrm{grav}} \approx \left(\frac{q_{\mathrm{d}}}{e}\right) n_{\mathrm{d}} \tag{9.12b}$$

and we have the following rationale:

> Ions that need not be trapped will after some time be picked-up. Assume short time.

We now also introduce the velocity transformations to the spacecraft frame, and obtain

$$\begin{aligned}&\left(\frac{m_{\mathrm{i}}\,|b|}{2e^2\,A_{\mathrm{LP}}}\right)-\frac{n_{\mathrm{e}}\sqrt{\frac{\Delta v_{\mathrm{rot}}^2}{16}+\frac{e\,T_{\mathrm{rot}}}{2\pi\,m_{\mathrm{i}}}}}{\Delta v_{\mathrm{rot}}^2+\frac{2e}{mi}T_{\mathrm{rot}}} = \\ &\frac{n_{\mathrm{grav}}\sqrt{\frac{\Delta v_{\mathrm{grav}}^2}{16}+\frac{e\,T_{\mathrm{grav}}}{2\pi\,m_{\mathrm{i}}}}}{\Delta v_{\mathrm{grav}}^2+\frac{2e}{mi}T_{\mathrm{grav}}}+\frac{\overbrace{\left(\left(\frac{q_{\mathrm{d}}}{e}\right)n_{\mathrm{d}}-n_{\mathrm{grav}}\right)}^{\approx 0}\sqrt{\frac{\Delta v_{\mathrm{rot}}^2}{16}+\frac{e\,T_{\mathrm{rot}}}{2\pi\,m_{\mathrm{i}}}}}{\Delta v_{\mathrm{rot}}^2+\frac{2e}{mi}T_{\mathrm{rot}}}\end{aligned} \tag{9.13}$$

where, according to our assumption, the last term disappears. Solving for n_{grav} we obtain

$$n_{\mathrm{grav}} = \frac{|ConstTerm - n_{\mathrm{e}}\,RotTerm|}{GravTerm} \equiv n_{\mathrm{i,dust}} \tag{9.14}$$

where

$$ConstTerm = \frac{m_\mathrm{i}\,|b|}{2e^2\,A_\mathrm{LP}} \tag{9.15a}$$

$$RotTerm = \frac{\sqrt{\frac{\Delta v_\mathrm{rot}^2}{16} + \frac{e\,T_\mathrm{rot}}{2\pi\,m_\mathrm{i}}}}{\Delta v_\mathrm{rot}^2 + \frac{2e}{m_\mathrm{i}}T_\mathrm{rot}} \tag{9.15b}$$

$$GravTerm = \frac{\sqrt{\frac{\Delta v_\mathrm{grav}^2}{16} + \frac{e\,T_\mathrm{grav}}{2\pi\,m_\mathrm{i}}}}{\Delta v_\mathrm{grav}^2 + \frac{2e}{m_\mathrm{i}}T_\mathrm{grav}} \tag{9.15c}$$

We now have an expression for how large a population of ions are coupled to dust and slowed to Keplerian speed. All parameters are known except for the two ion temperatures, T_grav and T_rot. For the colder population, T_grav should be < 3 eV, but for the hotter population, however, an interpolation of the plasma model for the inner magnetosphere from [Richardson, 1995] was used. This will give T_rot in the range [10, 235] eV.

9.5 Dust Regions

Now, it is time to look at the dust concentration in the E-ring. Is the dust uniform throughout the whole E-ring, or are there regions of higher dust concentration? And, if so, where are they?

9.5.1 The Inner Magnetosphere

To begin with, as previously mentioned, we know that the inner part of Saturn's magnetosphere – and the inner part of the E-ring as well – is populated by a much denser plasma than in the outer magnetosphere. Therefore, it is reasonable to assume that the amount of ions coupled to dust would also be higher there, and this is indeed what is seen in Figure 9.3.

As can be seen, Rev19 is an orbit with a high resolution scan of pretty much the entire part of the orbit spent in the E-ring. As such, it is a very good orbit for reference and comparison. With no special events – like, for instance, moon flybys – taking place during Rev19, it makes for a good example of a general case passage through the E-ring.

Note the measured ion speed $v_{\mathrm{i,I_0}}$ (black line) in Figure 9.3d). At about 5.5 $\mathrm{R_S}$ on the inbound side, the ion speed clearly goes from the hydrogen line (red) down to the water line (magenta), indicating a change in ion composition in the inner part of the E-ring (and the inner magnetosphere). On the outbound side, the transition in ion composition and ion speed is again noticeable at about 5 $\mathrm{R_S}$.

At the same time we see in panel c) that the electron density (black) increases, and so does the density of the ion–dust population (red), by a much larger amount, which means that the *dust ratio* – the ratio between number

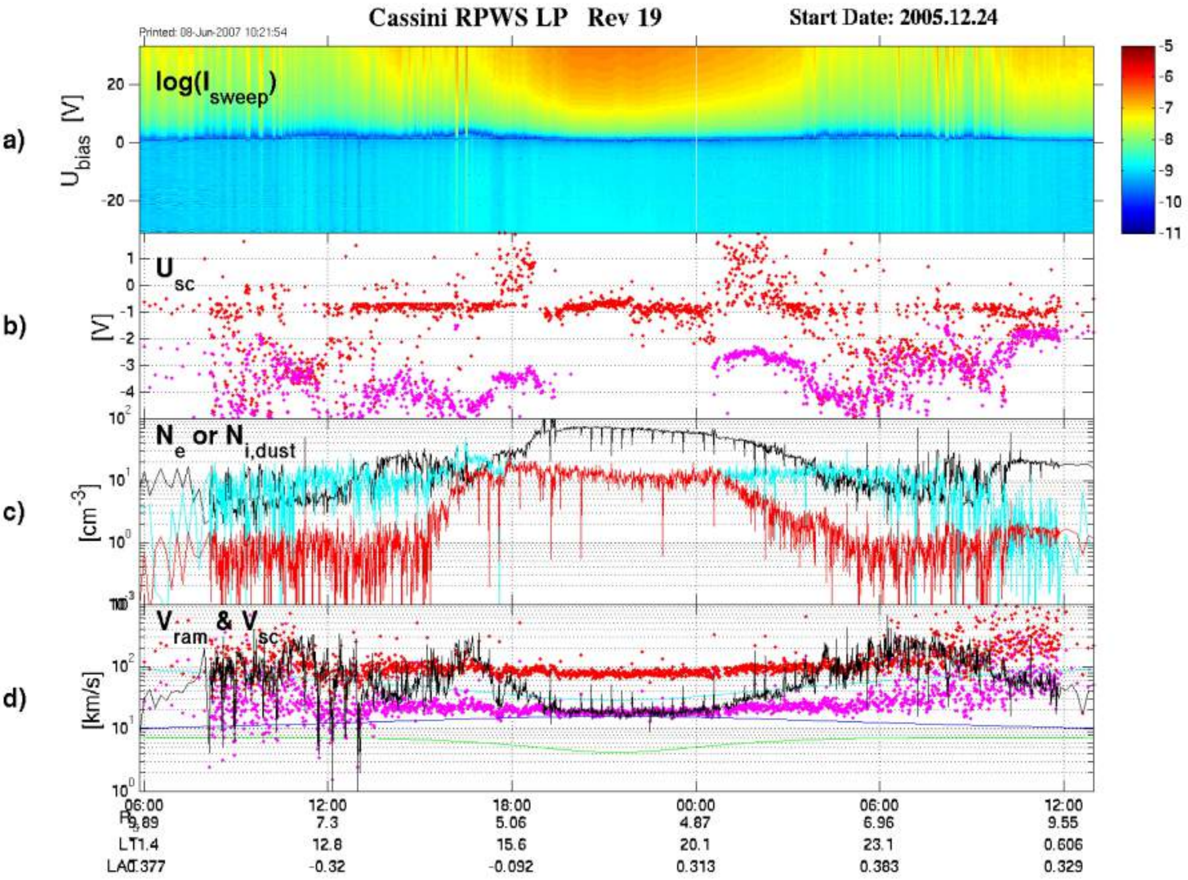

Figure 9.3: A plot of Rev19 within 10 $R_{\rm S}$ *(the E- ring). Panel a) shows the Langmuir probe voltage sweeps where the upper half of the panel is the electron side current and the lower half is the ion side current. Panel b) is the spacecraft potential for electron components 1(red) and 2(magenta) from the LP analysis. Panel c) shows the total electron number density(black) and the density of ions coupled to dust(*$n_{\rm i,dust}$*), assuming an ion mass of 18 amu (cyan) or varying according to Eq.* (9.3) *(red). Panel d) contains the calculated ion speed* $v_{\rm i,I_0}$ *(black) compared to asymptotic speeds of* H^+ *(red) and* H_2O^+ *(magenta). The cyan line is* $\Delta v_{\rm rot}$*, green is* $\Delta v_{\rm grav}$ *and blue is* $v_{\rm SC}$*.*

of ions coupled to dust and number of electrons (which is about the same as the number of ions) – increases in the inner part of the E-ring.

9.5.2 Moon Flybys

Among the types of regions of high interest when it comes to dust are the flybys of the icy moons. It is known from previous observations that some of these – Enceladus in particular, without dispute – in a high degree contribute to the dust in the E-ring, by ejecting ice particles and neutral gas out into the ring.

Following this reasoning, we should be able to see an added increase in dust ratio at and closely around a flyby of the moons. It should be an increase which is unrelated to the already increased dust ratio in the inner part of the magnetosphere.

Presented in Figure 9.4 is a plot of the E-ring passage of Rev3 which includes the flyby E0. Again, by looking at panel d) we see a decrease in ion speed in the inner part (∼6 R_S inbound and ∼5.5 R_S outbound), related to a change in ion composition from H^+ to H_2O^+. And similarly, we see the electron density, dust coupling density ($n_{i,dust}$) and dust ratio going up in panel c), in the same area.

However, at the actual flyby of Enceladus we can see an increase in the ion side current in panel a) (marked in red), and at the same time increases in panel c) and d). What is actually seen there, is the result of the south pole of Enceladus spewing out huge amounts of water ice into the E-ring. This added increase in $n_{i,dust}$ has the effect that, when the Langmuir probe moves through this region, a large amount of ice particles slams into the probe and also knocks out secondary electrons (see section 5.4.3). The increase in ion side current is thus coupled to the increases we see in the ion speed in panel d), i.e. it is not a real ion speed increase. The increase in $n_{i,dust}$ in panel c) is real though, since it does not depend on the DC-level increase in the ion side current in panel a), but is derived from the gradient of the current response.

From this, one can draw the conclusion that the icy moons feeding the E-ring has a significant impact on the dust in the E-ring, in every aspect. The moons affect not only the dust density and concentration, but also the degree of how much coupling between dust and plasma is taking place in a certain region.

9.5.3 Icy Dust Hailstorms

Another very interesting type of region, that has presented itself as a result during the dust investigations in this thesis, is something I have named *hailstorms*. Hailstorms are, as the name suggests, a region of intense snow (micrometer sized ice grains) in space, almost to the point of a blizzard. We have already seen a small example of this phenomenon in Figure 9.4 (the region marked in red). At that time, the Langmuir probe was bombarded by ice from Enceladus during a close flyby of the moon.

Although, while the presence of a hailstorm during an Enceladus flyby

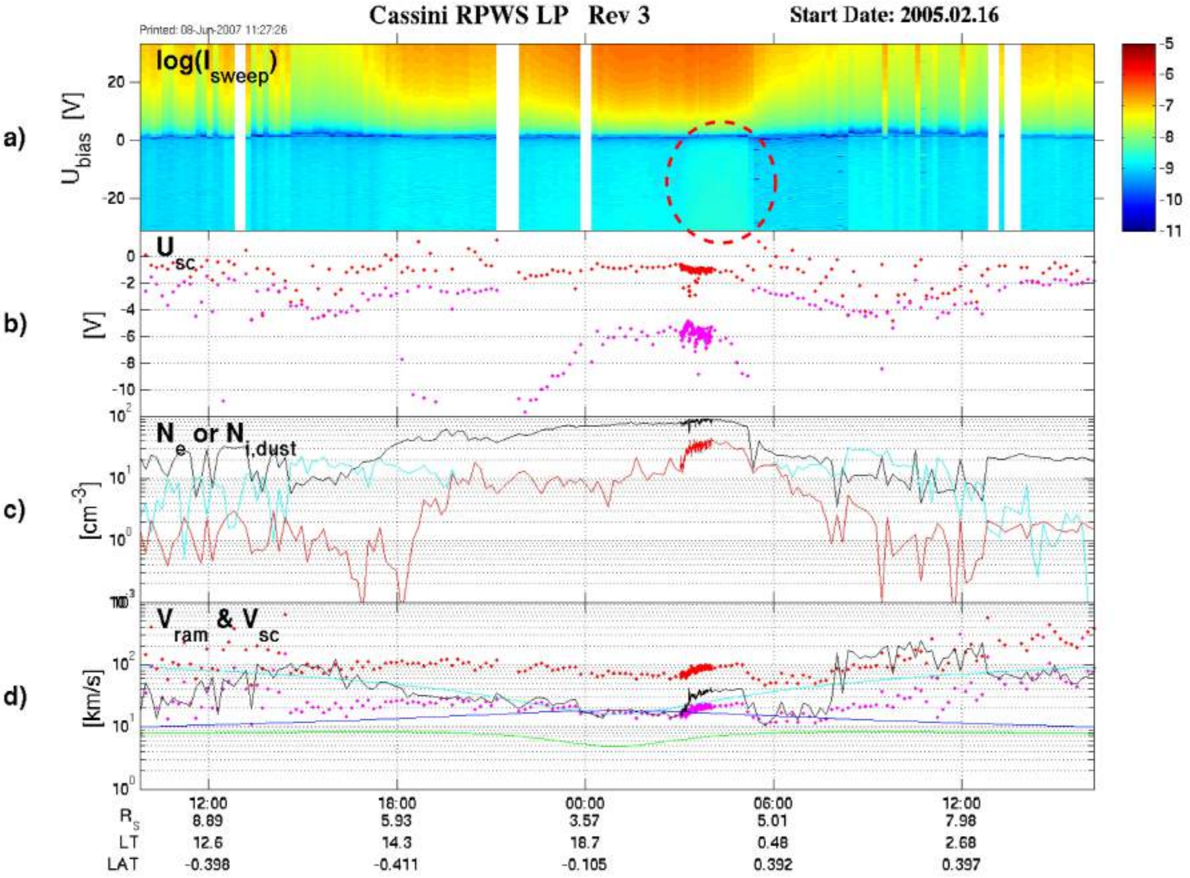

Figure 9.4: Plot of Rev3 in the E-ring (< 10 R_S). Panels and parameters are the same as in Figure 9.3. The E0 flyby is visible during the time period marked in red (a hailstorm) in panel a). This dashed region is a clear indication of the presence of large concentrations of dust. The spikes visible in panel a) between approximately 08:00-11:00 are believed to be energetic particles hitting the probe, probably from Saturn's radiation belt.

would probably come as little to no surprise, I have found evidence of hailstorms that are *not* during flybys of any moons. Looking more closely at the orbit with the first interferometry measurement, Rev17 revealed a very nice and clear hailstorm region, which is marked in Figure 9.5. Looking at this, we see in panel a) that a hailstorm region has very sharp and distinct boundaries; flying into this is basically to hit a sudden wall of ice particles. In panel c) we can see that $n_{\mathrm{i,dust}}$ more than doubles in a matter of minutes and, at the end of the interferometry measurement (the high-resolution part) and an hour or

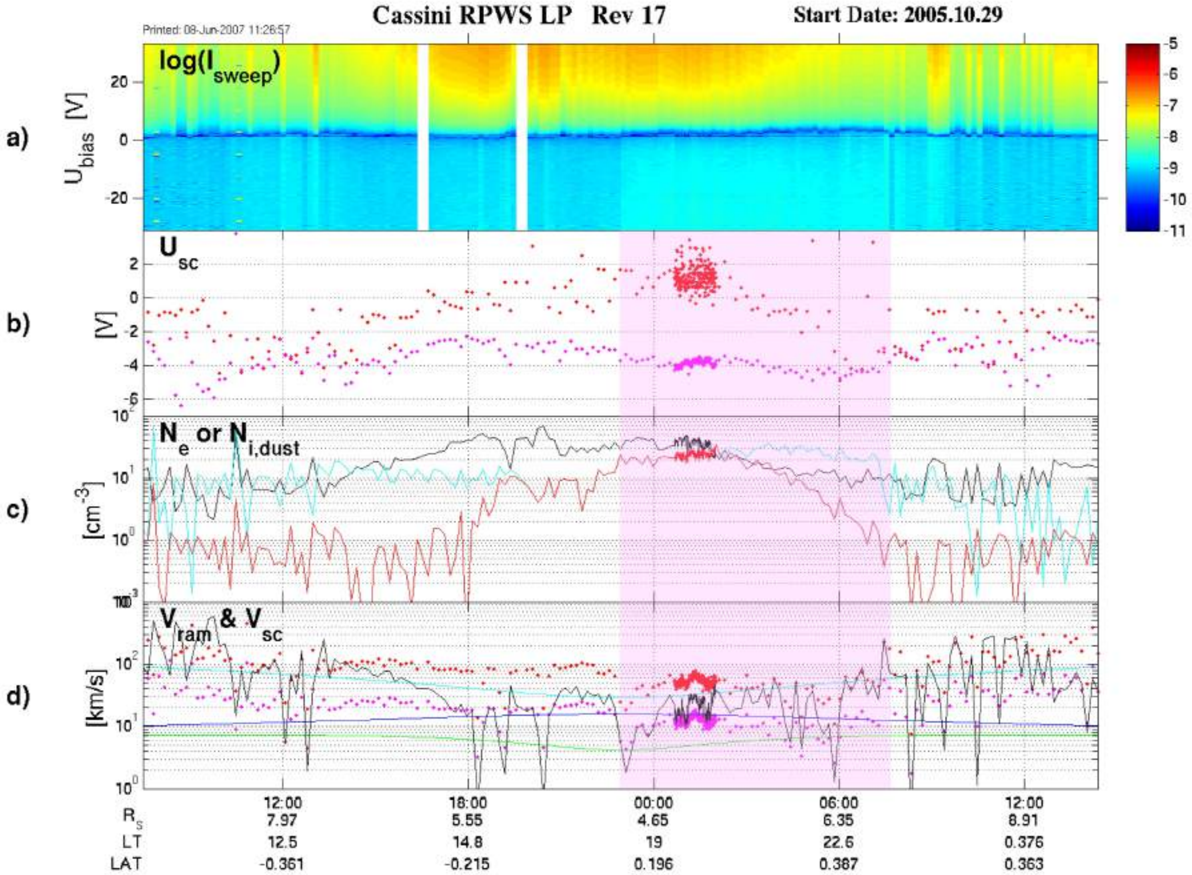

Figure 9.5: Plot of the E-ring passage during Rev17, containing the first interferometry measurement (high-resolution part). Panels and parameters are the same as in Figure 9.3. The marked region denotes a hailstorm clearly noticeable with distinct boundaries on the ion side in panel a).

so beyond, $n_{\mathrm{i,dust}}$ is actually on par with – or even slightly *larger* than (which is unphysical) – the total electron density!

We can also see that the hailstorm is quite broad; extending from ∼4 $\mathrm{R_S}$ to ∼7 $\mathrm{R_S}$ distance. It is also worthwile to note that this hailstorm is only present during the outbound part of the orbit; only a very tiny part of it – which seems to be a short transition region – extends to the inbound side of Rev17.

A hailstorm such as this, which is not present during a flyby, still has to come from somewhere. Most likely they originate from the icy moons and are the trail left behind in the wake by the moons when they spew out particles into the ring, much the same way as the (dust) tail of a comet.

The fact that this hailstorm is so broad, also seems to suggest that Enceladus – while most likely being (one of) the main source(s) of new ice/dust particles – most probably is not the only (major) source of particle production for the E-ring. Other likely and interesting candidates include both *Tethys* (at 4.9 R_S distance) and *Dione* (at 6.3 R_S distance). More on this later in section 11.3.

Reports are also coming in about a *dust halo* around *Rhea* (and the possibility of rings around the moon)[1], in the outermost part of the E-ring (at 8.7 R_S distance). This is certainly an interesting phenomenon and would be worthy of further investigation (see chapter 12).

---

[1] See [Jones et al., 2007]

10

Results & Discussion

10.1 Photoelectron Corrections

Using data from tenuous plasma only (outer magnetosphere or solar wind), a model for photoelectron current variation with spacecraft attitude was constructed, and correction with regard to a chosen reference vector was applied.

The model that was implemented was proven quite successful. However, some orbits still show a slight artificial variation, which correlates with the attitude pointing of the spacecraft. It is left for future studies to investigate this remaining feature. The small error involved (about 0.1 nA) does not significantly affect the results in this study.

By using the SSE coordinate system instead of SSQ, some of the noise in the result would have been reduced. However, it would not have affected the general behaviour of the correction model. The reason for this is because the algorithm I have written calculates angles between the spacecraft axes and a general (fairly arbitrary) reference vector. Then, the photoelectron variation is analysed in dependency of variation in these angles, and correction is applied based on this.

The further the chosen reference vector is from the true vector of photon incidence, the higher the noise in the result will be. The variation still follows an arctan behaviour related to the spacecraft X-axis, but the spread will be larger.

10.2 Ion Speed Calculations

Starting from the ion side current, the ion speed was derived in two ways; from the slope of the U-I characteristic, ion speeds for H^+ and H_2O^+ were calculated using their respective ion masses, and these were used as boundaries when comparing with the ion speed, v_{i,I_0}, calculated from the DC level.

The calculations of the plasma ion speed, v_{i,I_0}, give a fairly accurate result in the E-ring. Outside 10 $\mathrm{R_S}$ the calculated values become unrealistic in most cases. The reason for this is that, as can be seen in equation (8.5), the calculation of the ion speed is dependent on the electron density, n_e. The obtained values for n_e seem to be consistently giving lower values compared with values calculated from the upper hybrid frequency, f_UH.

A correction for n_e – based on a comparison between ELS and LP data – was applied. However, this is only valid in a tenuous plasma, which restricts it to outside 10 $\mathrm{R_S}$. This correction is not yet fully optimised and, when applied, will affect the ion speed. However, since these doubtful values are outside the E-ring, they are not taken into account within the scope of this thesis.

10.3 Dust Ratio Estimations

The parts within 10 $\mathrm{R_S}$ from a total of eight orbits, containing events or regions of high interest, were chosen. For these, a model for how the ion mass in the E-ring varies with distance from Saturn was derived and, using this, an estimation of the fraction of ions coupled to icy dust particles was calculated. The result was then organised into three main categories of regions; inner magnetosphere, moon flybys and hailstorms not during flybys.

With the results obtained here, it is clear that dust—plasma interaction is, in fact, taking place, and to quite a large degree at that. The degree of coupling varies with the concentration of both dust and ions in the plasma; in a higher density plasma like the inner part of the E-ring, or in a region of higher density of dust, the amount of ions coupled to the dust increases significantly.

The fact that an increase in the amount of dust gives rise to such a huge increase in the dust ratio, is explained by the fact that the dust charge is negative enough to couple several (thousand) ions. Thus, a variation in the charge on each dust would also give a huge variation in the dust ratio.

The phenomenon of the hailstorms is an interesting new discovery. One difficulty they bring, though, is the fact that the increase they give rise to is a combination of several effects; increased dust coupling, dust impact & vapourisation, and the knock-out of secondary electrons from the probe surface. Only the dust ratio increase is of interest for the results in this thesis, which is easily obtained by using the gradient of the current response, which disregards the DC level coupled to the other effects.

11

Conclusions

The main objectives of this study was to first investigate the presence of two ion populations in the E-ring, to confirm the findings from the interferometry measurement(s). When this had been confirmed, the next objective was to examine if we do in fact have dust–plasma interaction in the E-ring, to explain why we have more than one ion population and why we get different inferred velocities from different instruments. The last main objective was: if dust–plasma interaction is found, then estimate how large a part of the total number of ions are coupled to the dust and map this as a function of distance from Saturn in the equatorial plane. This to see *where* this coupling was present, *what factors* where involved in its origin, and *how much* interaction was going on in different regions in space.

This chapter summarises the conclusions I have drawn, based on the findings from my analysis. Not only have the questions from the project objectives found answers, but new and previously unknown facts have come to light, which may have a significant impact upon the direction and focus of future investigations of the Saturnian system.

11.1 Ion Populations

I have confirmed that (at least) two ion populations can be consistent with the data from the Langmuir probe in the inner magnetosphere of Saturn.

The two populations found are one hotter co-rotating, and one colder moving at close to Keplerian speed. This finding is supported by the result of the ion speed being calculated in two independent ways and then compared. A clear drop from co-rotational speed to Keplerian speed can be easily seen in the inner magnetosphere.

The results also seem to give some indications to the possible presence of a third ion population as well. Such a population would also be consistent with the Langmuir probe data, and while the current analysis model is not designed to handle this case, it does not negate the possibility. Whether or not a third ion population actually exists is at this point speculation, and warrants further investigation. It is probable that the smaller dust are accelerated by the co-rotating electric field, and produce a velocity distribution (with trapped ions) with a peak around the Keplerian speed.

11.2 Dust—Plasma Interaction

From the findings I have confirmed that dust–plasma interaction is in fact taking place. A coupling ratio of 20 % or more (out of the total number of ions) can be commonly found, for example all the time in the innermost part of the E-ring and the inner magnetosphere. This is also in agreement with the ion populations found in the region.

The results indicate, that the dust–plasma interaction ratio is highly dependent on the amount of dust present in a given region; the more the dust, the higher the ratio of ions that are coupled to dust. The increase is exponential, since the negative charge on the dust is such that several thousand ions can be coupled to each dust grain before the grain becomes neutral enough to no longer attract nearby ions.

The dust–plasma interaction goes up near the icy moons in the E-ring. Given the finding of the above relationship, this effect was expected near Enceladus; the huge increase in dust particles near Enceladus from the ejections near its south pole, caused one of the highest number of ions coupled to dust seen yet (upwards of 40 cm^{-3}, see Figure 9.4). However, since Enceladus also ejects neutral gas which later becomes ionised, the total amount of ions in the region is also high, which causes the coupling ratio to be ∼40 %.

More surprisingly was the fact that a higher dust–plasma interaction could be seen during the flybys of the other icy moons as well; in particular Tethys and Dione. This suggests that there is an ejection of dust particles from these moons as well, and/or a change in ion composition to predominantly water, to account for this increase in coupling ratio. The results in Figure 9.2 suggest that there is more going on at Tethys and Dione than we currently know, and support the theory of an ion composition change near these moons. Also, in the left half of Figure 9.3d), a change in ion speed at ∼6.3 $\mathrm{R_S}$ distance (the orbit of Dione) is further support of this hypothesis.

The phenomenon of the hailstorms, being regions in space with a high density of ice grains, naturally also give rise to a large increase in coupling ratio. With the sharp boundaries inherent to the hailstorms, the effect on dust–plasma coupling is also distinct and immediate.

The hailstorms are confirmed to be present both near flybys of the icy moons as well as in the trail left behind in their orbits. The full effect of the hailstorms can be more clearly seen in the trail, where there is no moon flyby and the total ion density is thus lower, in which the coupling approaches 100 % (see Figure 9.5)! But, even near the moon flybys a ratio of 40-50 % or more is common.

I have also concluded that the hailstorms give rise to effects in measurements which may or may not be unwanted. Ice grain collisions with the Langmuir probe at high relative velocities lead to dust vapourisation on probe impact and secondary electron emissions from probe surface. This can significantly affect the current response, and needs to be taken into account.

In any case, the hailstorms are clearly an interesting phenomenon with impacts on a wide variety of effects in the region. I believe they would be worthy of further close investigation.

11.3 E-ring Particle Production

As an additional finding from the results obtained during my analysis, I have also reached the conclusion that Enceladus is a major source of the particle production that sustains the E-ring. However, in contrast to popular belief today, I believe it very likely that *several* of the icy moons in the E-ring are feeding it – and to a significant degree. While Enceladus without question is a main source, it is probably not the only main source.

My conclusion is supported by the results of the ion speed calculations, which show a change in ion composition near the orbits of Tethys and Dione as well as Enceladus. This ion composition change is again supported by the estimation of the ion mass as a function of distance from Saturn, showing clear variations near Tethys and Dione.

I have also shown that contribution from the moons leads to an increase in dust–plasma coupling – an increase which is unrelated to the coupling already present in the inner magnetosphere, which is seen in the inner part of the E-ring. This is further evidence of particles being ejected from the moons.

Among the strongest evidence for my conclusion, is the broad hailstorm seen in Figure 9.5. I believe such a broad hailstorm cannot come from Enceladus alone; if that were the case, it would not still have such sharp boundaries. And also, the hailstorm seems to peak near the orbit of Tethys – not Enceladus! It is more likely that the hailstorm seen in the figure is a *superposition* of (two or) three hailstorms; one from each of Enceladus, Tethys and (possibly also) Dione. Although it drops off between Tethys and Dione, there is a sudden peak across the board at around the orbit of Dione.

Putting all the evidence together, I believe it is clear that both Tethys and Dione are very much involved in the particle production which is sustaining the E-ring. However, further investigation with a more in-depth focus on these moons should be done.

Also, it is still unclear what role Rhea plays in the mystery of the E-ring.

With the discovery of a dust halo and possibly rings around Rhea (see [Jones et al., 2007]), this moon might also be involved in sustaining the E-ring to some extent, even if such conclusions could not be drawn within this thesis.

12

Outlook

This chapter will look at possible future extensions to the work done within this thesis. Some of them more imminent and some more natural, others more important and, regrettably, more distant. However, all of the extensions would most likely provide valuable information in their own way, which would further increase the benefit of this thesis.

A first natural step will be to compare my results with data from the Cosmic Dust Analyzer (CDA) on board Cassini. With CDA being more specifically designed for dust detection and analysis, compared to the Langmuir probe which has to rely on secondary effects to draw conclusions about the dust, if the CDA results are in agreement with my findings it would strengthen their validity.

To further validate the findings presented here, a study should be done which would take a look *outside* the ring plane (at high latitudes[1]), where we do not expect to find any dust. If the findings from the analysis model I have implemented would there be in agreement with this hypothesis, then this result would in turn confirm my findings about the ring plane.

Within this thesis I have focused the study of dust–plasma interaction on eight orbits that looked to be of particular interest. Another natural extension of my work would be to extend the derived analysis to cover *all* remaining available orbits. By doing this, a database of dust data can be built up, which would give a more complete picture of how the ratio of dust coupling varies as a function of space.

Another thing to consider is the situation of the Langmuir probe being in the spacecraft wake. This case should also be investigated.

Finally, one would also hope for new satellite missions to the Saturnian sys-

---

[1] Inclinations to the equatorial plane.

tem, with a primary objective to examine the icy moons in the E-ring in great detail. There still seems to be very little known about these highly interesting moons, and new knowledge may very well find many of the current theories to be completely wrong. Already, the accepted theory of what is sustaining the E-ring seems to be incorrect – or at least incomplete.

There is also the matter of future studies which may be seen as more indirect extensions of this thesis. One example of this is the discovery of a dust halo around Rhea, and the subsequent theory of possible rings around that moon. This is as yet unconfirmed, but further investigation of this would probably be, not only very interesting, but most likely also a valuable piece of the puzzle that is the E-ring.

A

MATLAB Routines

Presented here are the MATLAB routines that have been developed to carry out the different parts of this thesis work, in order to investigate the dust–plasma interaction in Saturn's inner magnetosphere. It should however be noted that these routines are not meant to – nor can they – be run independently. They are dependent on the prior running of other programs at IRFU, to calibrate the Langmuir probe data in its various modes and to load data sets of parameters into variables in MATLAB. For a good overview of many of these prerequisite programs, see [Westerberg, 2007, Appendix A]. Only the routines that have been developed by me for this thesis work, are presented here.

Section A.1 contains programs for reading the spacecraft attitude data and correcting the ion current for photoelectrons depending on the attitude. After the correction has been applied, the ion speed is also calculated here.

The routines in section A.2 are the ones used for doing the actual curve fitting to, and correction for, the photoelectron impact on the sampled current. In the case of eclipse conditions, the negative eclipse values are raised to zero level.

The estimation of the ratio of ions coupled to dust is calculated in section A.3, using a model for the ion mass in the E-ring. The temperature for the corotating population, T_{rot}, is obtained from [Richardson, 1995].

The last section, A.4, contains a couple of utility functions to better facilitate the handling of MATLAB figure windows on servers at IRFU.

A.1 Spacecraft Attitude

A.1.1 Read_SA.m

```
%%%%%%%%%%%%%%%%%%%%%%%%%%%%%%%%%%%%%%%%%%%%%%%%%%%%%%%%%%%%%%%%%%%%%%%%%%%%%%%%%%%%%%%%
% Read_SA.m                                                                            %
%                                                                                      %
% Reads the Spacecraft Attitude data from data file aquired from the CASSINI           %
% Spacecraft Attitude Tool at                                                          %
%    http://www—pw.physics.uiowa.edu/¬tfa/cassatt.html                                 %
%                                                                                      %
% Copyright Mikael Lundberg, Swedish Institute of Space Physics, Uppsala, 2006         %
%%%%%%%%%%%%%%%%%%%%%%%%%%%%%%%%%%%%%%%%%%%%%%%%%%%%%%%%%%%%%%%%%%%%%%%%%%%%%%%%%%%%%%%%


%% Spacecraft Attitude data %%
%%%%%%%%%%%%%%%%%%%%%%%%%%%%%%

   % The filename of the attitude data file
   filename = input('Enter name of attitude data file [return=SA_Rev_12.dat]: ', 's');
   if(isempty(filename)), filename = 'SA_Rev_12.dat'; end

    % First, count the number of lines to get correct vector—length
    num_lines = 0;
    fid = fopen(filename, 'r');
   while true
      t_line = fgetl(fid);
      if ¬ischar(t_line), break, end
      num_lines = num_lines+1;
   end
   num_rows = floor(num_lines / 4);    % The number of actual data points


   % Create vectors to store the attitude data and the time information
   %    x, y, z are in the SSQ reference system
   %    X, Y, Z are in the S/C reference system
   [tab_xZ, tab_yZ, tab_zZ, tab_xY, tab_yY, tab_zY, tab_xX, tab_yX, tab_zX] = ...
      deal(zeros(num_rows, 1));

   [tab_year, tab_dayofyear, tab_hrs, tab_mins, tab_secs] = ...
      deal(zeros(num_rows, 1));


   % Parse the file and read the data
   frewind(fid)   % Marker is at EOF from when we counted the lines!
   i=1;
   for j=1:num_lines
      t_line = fgetl(fid);
      if ¬ischar(t_line)   % EOF
         break
      else
         % len_t = length(t_line);
```

```
         if t_line(1) == '2'     % Find first data row (look for the year)
            [date_time_part, tab_xX(i), tab_xY(i), tab_xZ(i)] = ...
               strread(t_line, '%s %f %f %f %*s', 'delimiter', ' ');

            [tab_year(i), tab_dayofyear(i), tab_hrs(i), tab_mins(i), tab_secs(i)] = ...
               strread(char(date_time_part), '%d-%dT%02d:%02d:%6.3f');

            t_line = fgetl(fid);    % Read the second line of coordinates
            [tab_yX(i), tab_yY(i), tab_yZ(i)] = ...
               strread(t_line, '%f %f %f', 'delimiter', ' ');

            t_line = fgetl(fid);    % Read the third line of coordinates
            [tab_zX(i), tab_zY(i), tab_zZ(i)] = ...
               strread(t_line, '%f %f %f', 'delimiter', ' ');

           i = i + 1;
         end   % end of if t_line ...
     end   % end of if ¬ischar ...
   end   % end of for
   fclose(fid);


%% Time conversions %%
%%%%%%%%%%%%%%%%%%%%%%

   M_date = doy2date(tab_year, tab_dayofyear);
   YYYY = tab_year;     % tab_year == M_date(:,1)
   MM = M_date(:, 2);
   DD = M_date(:, 3);
   hh = tab_hrs;
   mm = tab_mins;
   ss = tab_secs;
   t_YMDhms = [YYYY MM DD hh mm ss];
   t_angle = toepoch(t_YMDhms);


%% Calculation of angles %%
%%%%%%%%%%%%%%%%%%%%%%%%%%%

   %%%%%%%%%%%%%%%%%%%%%%%%%%%%%%%%%%%%%%%%%%%%%%%%%%%%%%%%%%%%%%%%%%%%%%%%%%%%%%%%%%%%%%
   %  To get the angle between two vectors V1 and V2, use the relation:                 %
   %     dot(V1, V2) = norm(V1)*norm(V2)*cos(angle(V1, V2))                             %
   %                                                                                    %
   %  We are interested in the angles between -X_SSQ and the three S/C axes, which      %
   %  are all normalised vectors, so the expression collapses to:                       %
   %     cos(angle) = dot(-X_SSQ, V) = -V(1)                                            %
   %%%%%%%%%%%%%%%%%%%%%%%%%%%%%%%%%%%%%%%%%%%%%%%%%%%%%%%%%%%%%%%%%%%%%%%%%%%%%%%%%%%%%%

   % Calculate the angle (theta) between the +Z (S/C) axis and the
   % direction of sunlight (-x SSQ):
   angle_ZSun = acos(-tab_xZ)*180/pi;  % in degrees

   % Calculate the angle (phi) between the +Y (S/C) axis and the
   % direction of sunlight (-x SSQ):
```

```
   angle_YSun = acos(−tab_xY)*180/pi;  % in degrees

   % Calculate the angle (alfa) between the +X (S/C) axis and the
   % direction of sunlight (−x SSQ):
   angle_XSun = acos(−tab_xX)*180/pi;  % in degrees


%% Interpolation section %%
%%%%%%%%%%%%%%%%%%%%%%%%%%%

   % Interpolation of the angle, following the t_sweep data:
   %      (t_angle, angle_*Sun)   −−>   (t_sweep, sweep_*Sun)
   if t_angle(end) ≥ t_sweep(end)
      sweep_ZSun = interp1(t_angle, angle_ZSun, t_sweep);
      sweep_YSun = interp1(t_angle, angle_YSun, t_sweep);
      sweep_XSun = interp1(t_angle, angle_XSun, t_sweep);
   else
      sweep_ZSun = interp1(t_angle, angle_ZSun, t_sweep, 'linear', 'extrap');
      sweep_YSun = interp1(t_angle, angle_YSun, t_sweep, 'linear', 'extrap');
      sweep_XSun = interp1(t_angle, angle_XSun, t_sweep, 'linear', 'extrap');
   end

   % Interpolation of the angle following the t_20_in data
   if t_angle(end) ≥ t_Ne(end)
      ZSun20 = interp1(t_angle, angle_ZSun, t_Ne);
      XSun20 = interp1(t_angle, angle_XSun, t_Ne);
      YSun20 = interp1(t_angle, angle_YSun, t_Ne);
   else
      ZSun20 = interp1(t_angle, angle_ZSun, t_Ne, 'linear', 'extrap');
      XSun20 = interp1(t_angle, angle_XSun, t_Ne, 'linear', 'extrap');
      YSun20 = interp1(t_angle, angle_YSun, t_Ne, 'linear', 'extrap');
   end
```

A.1.2 Corr_SA.m

```
%%%%%%%%%%%%%%%%%%%%%%%%%%%%%%%%%%%%%%%%%%%%%%%%%%%%%%%%%%%%%%%%%%%%%%%%%%%%%%%%%%%%%%%%
% Corr_SA.m                                                                            %
%                                                                                      %
%     Script that corrects the ion current for photoelectrons and calculates ion       %
%     velocity and mass.                                                               %
%     Also corrects the electron densities and the spacecraft potential.               %
%                                                                                      %
% Copyright Mikael Lundberg, Swedish Institute of Space Physics, Uppsala, 2006         %
%%%%%%%%%%%%%%%%%%%%%%%%%%%%%%%%%%%%%%%%%%%%%%%%%%%%%%%%%%%%%%%%%%%%%%%%%%%%%%%%%%%%%%%%

%% Settings %%
%%%%%%%%%%%%%%

   t_start = t_sweep(1);
   t_end = t_sweep(end);
   index_interval = find(t_sweep ≥ t_start & t_sweep ≤ t_end);  % select vector indices

   if ¬exist('bool_attitude_loaded')
      bool_attitude_loaded   = 0;
   end
   if ¬exist('bool_data_fitted')
      bool_data_fitted   = 0;
   end

   bool_plot_corr = 0;


%% Data Cleaning (for af)%%
%%%%%%%%%%%%%%%%%%%%%%%%%%%

   t1 = toepoch([2005 10 20 00 00 00]);        % Start of sweep + leading photoelectrons
   t2 = toepoch([2005 10 25 00 00 00]);        % End of leading photoelectrons
   t3 = toepoch([2005 11 05 00 00 00]);        % Start of trailing photoelectrons
   t4 = toepoch([2005 11 13 00 00 00]);        % End of sweep
   af_cutoff = 0.75;                           % Remove all af data above this

   cleanup_list = find( ((t_sweep > t2) & (t_sweep < t3)) | ...
                        (t_sweep > t_start & t_sweep < t_end & abs(−af) > af_cutoff));

   t5 = toepoch([2005 10 28 04 00 00]);        % Just before eclipse
   t6 = toepoch([2005 10 28 05 00 00]);        % Just after eclipse
   eclipse_cutoff = 0.15;                      % Keep all data below this unchanged

   eclipse_list = find( (t_sweep > t5) & (t_sweep < t6) & (−af < eclipse_cutoff) );


%% Photoelectrons %%
%%%%%%%%%%%%%%%%%%%%

   % The photoelectrons are dependent on the S/C attitude.
```

```
    % So we must first read the attitude data:
    if ¬bool_attitude_loaded
       Read_SA;
       bool_attitude_loaded = 1;
    end

    % Now we have to compensate for the effect of the photoelectrons upon the ion current.
    % We do this by applying an arctan curve fit upon the data:
    if ¬bool_data_fitted
       af_out                 = correct_af(sweep_XSun, af, cleanup_list, eclipse_list);
       %af_out                 = correct_af(sweep_XSun, af, cleanup_list);
       Ne_out                 = Correct_Ne(Ne_tot, Usc, Rs);
       bool_data_fitted = 1;
    end

    af_corr     = af_out;      % This is the 'random ion current' (w/o photo-e (= a) )
    Ne_corr     = Ne_out;


%% Ion calculations %%
%%%%%%%%%%%%%%%%%%%%%%


    Ti_eff = abs(af_corr./b);

    % Ion speed, assuming ram dominates, corrected for probe photoelectrons
    Ni_vi  = -af_corr.*1e-9./(qe*pi*0.025^2);
    vi_I0  = Ni_vi ./ Ne_corr .*1e-6;
    vi_I0  = abs(vi_I0);

    % From slope (assuming fraction of H = const)
    vi_Tieff1    = sqrt( (2*qe/mH) .* Ti_eff );           % 100% Hydrogen
    vi_Tieff16   = sqrt( (2*qe/(16*mH)) .* Ti_eff );      % 100% Oxygen
    vi_Tieff18   = sqrt( (2*qe/(18*mH)) .* Ti_eff );      % 100% Water

    Ni_1   = Ni_vi ./ vi_Tieff1 ./ 1e6;   % cm^(-3)
    Ni_16  = Ni_vi ./ vi_Tieff16 ./ 1e6; % cm^(-3)
    Ni_18  = Ni_vi ./ vi_Tieff18 ./ 1e6; % cm^(-3)

    % Composition from combined results
    mi     = (2*qe/mH) .* Ti_eff ./ vi_I0.^2;
```

A.2 Photoelectron Corrections

A.2.1 correct_af.m

```
function [af_out] = correct_af( XSun, af_in, cleanup_list, eclipse_list );
%%%%%%%%%%%%%%%%%%%%%%%%%%%%%%%%%%%%%%%%%%%%%%%%%%%%%%%%%%%%%%%%%%%%%%%%%%%%%%%%%%%%%%%%%
%  Correlation between the spacecraft X axis and the direction of sunlight (−x SSQ)     %
%  by fitting an arctan curve to the ion current, to compensate for photoelectrons.     %
%                                                                                       %
%  Usage:                                                                               %
%     [af_out]    = correct_af(XSun, af_in)                                             %
%     [af_out]    = correct_af(XSun, af_in, cleanup_list)                               %
%     [af_out]    = correct_af(XSun, af_in, cleanup_list, eclipse_list)                 %
%                                                                                       %
%     where XSun follows the t_sweep data. The optional cleanup_list holds the          %
%     indicies for data in af_in which should NOT be used for the curve fitting of      %
%     the photoelectron current (i.e. ion parts).                                       %
%     If there are data in af that should NOT be corrected the indicies for these can   %
%     be given in eclipse_list. (Mainly to be used when in eclipse)                     %
%                                                                                       %
% Copyright Mikael Lundberg, Swedish Institute of Space Physics, Uppsala, 2006          %
%%%%%%%%%%%%%%%%%%%%%%%%%%%%%%%%%%%%%%%%%%%%%%%%%%%%%%%%%%%%%%%%%%%%%%%%%%%%%%%%%%%%%%%%%

   if nargin < 4
      eclipse_list = [];
      if nargin < 2
         error('Incorrect number of input arguments')
      elseif nargin < 3
         warning('Cleanup list not given!');
         cleanup_list   = [];
      end
   end

   % In case eclipse_list is given as an array of logical indicies instead of
   % index numbers, do the following to make sure the data type is 'logical array' !
   if max(eclipse_list) ≤ 1
      eclipse_list = logical(eclipse_list);
   end


%% Data cleaning %%
%%%%%%%%%%%%%%%%%%%

    % To 'remove' the values, set them to NaN
   af2 = af_in;
   af2(cleanup_list) = NaN;

   % Some functions do not want NaN's; select the elements that are 'valid'
   index_valid_af = find(¬isnan(−af2));
   af3 = af2(index_valid_af);
```

```matlab
%% arctan curve fit %%
%%%%%%%%%%%%%%%%%%%%%%
   angle_vector = 0:180;

   % Prepare non-linear least square fit procedure
   opt                = optimset('lsqcurvefit');
   opt.MaxFunEvals    = 4000;
   opt.MaxIter        = 5000;
   opt.TolFun         = 1e-14;
   opt.TolX           = 1e-13;

   %%%%%%%%%%%%%%%%%%%%%%%%%%%%%%%%%%%%%%%%%%%%%%%%%%%%%%%%%%%%%%%%%%%%%%%%%%%%%%%%%%%%%
   %  Starting parameter guesses for:  y = ky*arctan(kx*x + phi) + m                   %
   %%%%%%%%%%%%%%%%%%%%%%%%%%%%%%%%%%%%%%%%%%%%%%%%%%%%%%%%%%%%%%%%%%%%%%%%%%%%%%%%%%%%%
%                 ky    kx   phi    m
   par_in    =  [ 1/pi   3   -180   0.45];
   par_min   =  [                       ];
   par_max   =  [                       ];

   % Create the x- and y-data to use as input for the fit
   xdata = XSun(index_valid_af);
   ydata = af3;

   try
      [par_out, resnorm, residual, exitflag] = ...
         lsqcurvefit('PhotoFit', par_in, xdata, ydata, par_min, par_max, opt);
   catch
      disp(lasterr)
      return;
   end

   % Get the fitted coefficient from the output, and evaluate the function
   % in the chosen x-interval to get the fitted y-data
   %[k m c dx]  = deal(par_out(1), par_out(2), par_out(3), par_out(4));
   Y_tmp       = feval('PhotoFit', par_out, XSun);
   ind_pos     = find(abs(Y_tmp) > 0);
   Y1          = zeros(length(XSun), 1);
   Y1(ind_pos) = Y_tmp(ind_pos);


%% Correction %%
%%%%%%%%%%%%%%%%

   % To compensate for spacecraft attitude variations, subtract the fitted
   % data from the original data.
   af_new_1 = af_in - Y1;
   af_new_1(eclipse_list) = af_in(eclipse_list);   % Restore 'unchanged' values
   if min(-af_new_1(eclipse_list)) < 0       % We need to raise negative eclipse values
      af_new_1(eclipse_list) = af_new_1(eclipse_list) + min(-af_new_1(eclipse_list));
   end
   af_out   = af_new_1;
```

A.2.2 PhotoFit.m

```
%%%%%%%%%%%%%%%%%%%%%%%%%%%%%%%%%%%%%%%%%%%%%%%%%%%%%%%%%%%%%%%%%%%%%%%%%%%%%%%%%%%%%%%%%
%                                                                                       %
% PhotoFit.m                                                                            %
%                                                                                       %
%     Calculates current values for attitude angles of the Langmuir probe on Cassini    %
%     relative to direction of incoming sunlight, as an arctan function with given      %
%     coefficients.                                                                     %
%                                                                                       %
% Copyright Mikael Lundberg, Swedish Institute of Space Physics, Uppsala, 2006          %
%%%%%%%%%%%%%%%%%%%%%%%%%%%%%%%%%%%%%%%%%%%%%%%%%%%%%%%%%%%%%%%%%%%%%%%%%%%%%%%%%%%%%%%%%
function af_new = PhotoFit(params, theta)

   % Default values for parameters:
   ky    = 1;     % Amplitude (y-scaling)
   kx    = 1;     % x-scaling
   m     = 0;     % y-shift
   phi   = 0;     % Phase (x-shift)

   % Copy input values:
   args = length(params);
   if args > 0
      ky = params(1);
      if args > 1
         kx = params(2);
         if args > 2
            phi = params(3);
            if args > 3
               m = params(4);
            end
         end
      end
   end

   %  We need to map the angles in theta to the correct x-region
   %  which is the span [-pi, +pi] ( = [-180, +180]° )
   theta_mapped = deg2rad((kx * theta + phi));    % Map theta to cover [-180, +180]°

   % We now calculate the y-values (the new af)
   af_new = ky * atan(theta_mapped) + m;
```

A.3 Dust Ratio Estimations

A.3.1 correct_mi.m

```
%%%%%%%%%%%%%%%%%%%%%%%%%%%%%%%%%%%%%%%%%%%%%%%%%%%%%%%%%%%%%%%%%%%%%%%%%%%%%%%%%%%%%%%%
%                                                                                      %
% correct_mi.m                                                                         %
%                                                                                      %
%     Calculates a model for the ion mass in Saturn's E—ring depending on the radial   %
%     distance from Saturn (in Rs), based on observations from the following           %
%     Cassini orbits:                                                                  %
%     Rev3, Rev4, Rev11, Rev15, Rev16, Rev17, Rev18, Rev19                             %
%                                                                                      %
% Copyright Mikael Lundberg, Swedish Institute of Space Physics, Uppsala, 2007         %
%%%%%%%%%%%%%%%%%%%%%%%%%%%%%%%%%%%%%%%%%%%%%%%%%%%%%%%%%%%%%%%%%%%%%%%%%%%%%%%%%%%%%%%%
function mi = correct_mi(Rs)

   mi =  ones(size(Rs));

   mi(find(Rs ≤ 5)) =  18;

   ind   =  find(Rs > 5 & Rs < 6.7);

   mi(ind)  =  10 .^ ( (6.7 — Rs(ind))/1.35 );
```

A.3.2 DustRatio.m

```
%%%%%%%%%%%%%%%%%%%%%%%%%%%%%%%%%%%%%%%%%%%%%%%%%%%%%%%%%%%%%%%%%%%%%%%%%%%%%%%%%%%%%%%%
%                                                                                      %
% DustRatio.m                                                                          %
%                                                                                      %
%    Calculates the 'co-rotation to Keplerian' ratio of ions.                          %
%                                                                                      %
% Copyright Mikael Lundberg, Swedish Institute of Space Physics, Uppsala, 2007         %
%%%%%%%%%%%%%%%%%%%%%%%%%%%%%%%%%%%%%%%%%%%%%%%%%%%%%%%%%%%%%%%%%%%%%%%%%%%%%%%%%%%%%%%%

   file_save = input('Save parameters to file? 1=yes, 0=no : ');


% Input
   qe = 1.6e-19;
   mH = 1.67e-27;
   %mi = mH*18;
   %mi    = (2*qe/mH) .* Ti_eff ./ vi_I0.^2;
   mi    = (2*qe) .* Ti_eff ./ vi_I0.^2;
   mi_calc  =  correct_mi(Rs);
   mi    =  [mi 18*mH*ones(length(mi),1) mi_calc*mH];    % Calculate for 3 models for mi

   index = find(Rs < 10);

   v_rot    =  Vrot_sweep;       % [m/s]
   v_grav   =  Vgrav;            % [m/s]
   n_tot    =  Ne_tot;           % [cm^-3]
   T_grav   =  2;                % [eV]
   T_rot    =  20;               % [eV]
   dI_dU    =  abs(b)*1e-9;      % nA/V -> A/V
   A_LP     =  4*pi*0.025^2;     % [m^2]

   t_start  =  t_sweep(index(1));
   t_end    =  t_sweep(index(end));

   % Obtaining T_rot from John D. Richardson's Plasma Model:
   L_Rich   =  1.0:0.5:10.0;
   T_H      =  [10 10 10 10 13 28 40 60 80 90 100 110 120 140 180 200 220 230 235];
   T_rot2   =  interp1(L_Rich, T_H, Rs(index));
   T_rot3   =  interp1(L_Rich, T_H, Rs);


% Calculations

   % Transformation from cartesian coordinates (SSQ) to cylindrical coordinates
   %theta    =  atan(Y ./ X);
   %ind_X    =  find(X < 0);
   %theta(ind_X) = theta(ind_X) + pi;
   [theta, r] = cart2pol(X, Y);

   Vsc_r    =   Vx.*cos(theta) + Vy.*sin(theta);
```

```
   Vsc_th   =  -Vx.*sin(theta) + Vy.*cos(theta);
   Vsc_z    =  Vz;
   Vsc_rz   =  sqrt( Vsc_r.^2 + Vsc_z.^2 );

   v_ram    =  Vsc_r.^2 + Vsc_z.^2;

   dv_grav2 =  abs( v_grav - Vsc_th ).^2 + v_ram;
   dv_rot2  =  abs( v_rot - Vsc_th ).^2 + v_ram;

   dv_grav  =  sqrt(dv_grav2);
   dv_rot   =  sqrt(dv_rot2);


   % Do calculations for each of the 3 different models for mi:
   for col = 1:3
   grav_term(:,col)   = sqrt( dv_grav2./16 + qe*T_grav./(2*pi*mi(:,col)) ) ./ ...
                        (dv_grav2 + 2*qe*T_grav./mi(:,col));
   rot_term(:,col)    = sqrt( dv_rot2./16 + qe*T_rot./(2*pi*mi(:,col)) ) ./ ...
                        (dv_rot2 + 2*qe*T_rot./mi(:,col));  % Fixed T_rot
   rot_term_2(:,col)  = sqrt( dv_rot2./16 + qe*T_rot3./(2*pi*mi(:,col)) ) ./ ...
                        (dv_rot2 + 2*qe*T_rot3./mi(:,col)); % T_rot from Richardson
   const_term(:,col)  = mi(:,col).*dI_dU ./ (2*(qe^2)*A_LP);


   %n_grav_ratio = (2*mi.*dI_dU./((qe.^2)*A_LP)).*sqrt(dv_grav.^2+v_ram)./(n_tot*1e6) ...
   %               - (sqrt(dv_grav.^2 + v_ram) ./ sqrt(dv_rot.^2 + v_ram));

   %n_grav_ratio2  =  (const_term./(n_tot*1e6) - rot_term) ./ grav_term;
   %n_dust_2       =  (const_term - (n_tot*1e6).*rot_term) ./ grav_term; % Tg = Tr = 0
   n_dust_3(:,col)   =  abs((const_term(:,col) - (n_tot*1e6).*rot_term_2(:,col)) ./ ...
                            grav_term(:,col))/1e6;  % [cm^-3]
   end


% Plotting

   %figure
if 1              % Turn on internal (test/debug) plotting
   av_subplot(2, 1, -1);
      semilogy(t_sweep(index), dv_rot(index), 'r-', t_sweep(index), dv_grav(index), 'g-')
      hold on
         semilogy(t_sweep(index), Vsc_r(index), 'y-', t_sweep(index), Vsc_th(index), 'm-')
         semilogy(t_sweep(index), Vsc(index), 'c-')
         semilogy(t_sweep(index), vi_I0(index), 'k-')
         semilogy(t_sweep(index), Vsc_rz(index), 'b-')
         %semilogy(t_sweep(index), v_tot(index), 'b-')
         semilogy(t_sweep(index), v_grav(index), 'g--',t_sweep(index),v_rot(index), 'r--')
      hold off
      xlim([t_start t_end]);
      ylim([2e2 4e5])
      ylabel('\bf{[m/s]}')
      legend('\Deltav_{rot}', '\Deltav_{grav}', 'v_{sc,r}', 'v_{sc,\theta}', ...
             'v_{sc}', 'v_m', 'v_{sc,rz}', 'Location', 'SouthEast')
      grid on;
```

```
      add_empty_axis(gca);

      rev_str     =  textscan(filename, '%*s %s %s %*s', 'delimiter', '._');
      header_str  = sprintf('Dust ratio for %s %s', char(rev_str{1}), char(rev_str{2}));
      title(header_str, 'FontName', 'Times', 'FontWeight', 'bold', 'FontSize', 16)


   av_subplot(2, 1, -2);
      semilogy(t_sweep(index), n_tot(index), 'k')
      hold on
         %semilogy(t_sweep(index), n_dust_3(index, 1), 'm')
         semilogy(t_sweep(index), n_dust_3(index, 2), 'b')
         semilogy(t_sweep(index), n_dust_3(index, 3), 'r')
         %semilogy(t_sweep(index), n_dust_2(index), 'g')
         %semilogy(t_sweep(index), mi(index)/mH, 'g.')
      hold off
      xlim([t_start t_end]);
      ylim([1e-1 1e2]);
      ylabel('\bf{[cm^{-3}]}')
      legend_str1 = 'n_{dust} with T_{grav} = 0 eV, T_{rot} = 0 eV';
      legend_str2 = sprintf('n_{dust} with T_{grav} = %2d eV, T_{rot} = %2d eV', ...
                            T_grav, T_rot);
      %legend_str3 = sprintf(['n_{i,dust} with T_{grav} = %2d eV, T_{rot} from ', ...
      %                        'Richardson and m_i varying'], T_grav);
      %legend_str4 = 'n_{i,dust} same as above but with fixed m_i = 18m_H';
      %legend_str5 = 'n_{i,dust} same as above but m_i calculated from R_S';
      legend_str3 = sprintf('n_{i,dust} from Richardson and varying m_i');
      legend_str4 = 'n_{i,dust} with fixed m_i = 18m_H';
      legend_str5 = 'n_{i,dust} with from Richardson and m_i from R_S';
      legend('N_{e,tot}', legend_str4, legend_str5, 'Location', 'South')
      grid on;
      add_timeaxis( gca, 0, [t_sweep Rs Z LAT], {'R_S' 'Z' 'LAT'} );

else
   Plot_Main2     % Use external (normal) plotting instead
end

if file_save
   disp('Saving dust parameters to file...');
   status = Save_Dust( t_sweep, LONG, LAT, LT, Rs, X, Y, Z, L, Vsc_r/1e3, Vsc_th/1e3, ...
               Vsc_z/1e3, Vsc/1e3, v_grav/1e3, v_rot/1e3, vi_I0/1e3, ...
               vi_Tieff1/1e3, vi_Tieff18/1e3, b, Usc, mi(:,1)/mH, n_tot, n_dust_3(:,3) );
   if status == 0
      disp('Save complete...')
   else
      fprintf('Error saving! Status = %d', status);
   end
end
```

A.3.3 Save_Dust.m

```
%%%%%%%%%%%%%%%%%%%%%%%%%%%%%%%%%%%%%%%%%%%%%%%%%%%%%%%%%%%%%%%%%%%%%%%%%%%%%%%%%%%%%%%%
%                                                                                      %
% Save_Dust.m                                                                          %
%                                                                                      %
%    Saves parameters related to dust ratio estimations to file.                       %
%                                                                                      %
% Copyright Mikael Lundberg, Swedish Institute of Space Physics, Uppsala, 2007         %
%%%%%%%%%%%%%%%%%%%%%%%%%%%%%%%%%%%%%%%%%%%%%%%%%%%%%%%%%%%%%%%%%%%%%%%%%%%%%%%%%%%%%%%%
function status = Save_Dust( t_sweep, LONG, LAT, LT, Rs, X, Y, Z, L, V_r, V_th, V_z, ...
                             Vsc, Vgrav, Vrot, V_meas, vi_Tieff1, vi_Tieff18, b, Usc, ...
                             mi, Ne_tot, N_dust, filename )

  % Default filename if not given.
  if nargin < 24
     filename = 'Dust.dat';
  end

  % Open file for writing.
  [fid, message] = fopen( filename, 'w' );

  % Check file.
  if fid == −1
     disp( message );
     %disp( machineformat );
     status = −1;
     return;
  end

  % Interval
  ind = find(Rs ≤ 10);

  % Time
  YmdHms = fromepoch( t_sweep(ind) );

  % Arrange output data.
  position = [LONG(ind), LAT(ind), Rs(ind), X(ind), Y(ind), Z(ind), L(ind)];    % 7
  velocities = [V_r(ind), V_th(ind), V_z(ind), Vsc(ind), Vgrav(ind), Vrot(ind), ...
                V_meas(ind), vi_Tieff1(ind), vi_Tieff18(ind)];  % 9
  temp = [YmdHms, LT(ind), position, velocities, b(ind), Usc(ind), ...
          mi(ind), Ne_tot(ind), N_dust(ind)];   % 6 + 1 + 7 + 9 + 5  =  28
  out_data = transpose(temp);

  % Write to file.
  format_str   =  ['%4d %2d %2d %2d %2d %6.2f %8.3f %8.3f %8.3f %8.3f %8.3f %8.3f ', ...
                   '%8.3f %8.3f %8.3f %8.3f %8.3f %8.3f %8.3f %8.3f %8.3f %8.3f ', ...
                   '%8.3f %8.3f %8.3f %8.3f %8.3f %8.3f\n'];
  fprintf( fid, format_str, out_data );

  % Close file and return status.
  status = fclose( fid );
```

A.4 Utility Functions

A.4.1 figprint.m

```
function figprint(thisFig, whichPrinter, orientation)

   if nargin < 3
      orientation = 'landscape';
      if nargin < 2
         whichPrinter = 'hp4600';
         if nargin < 1
            thisFig = gca;
         end
      end
   end

   for k=1:length(thisFig)
      orient(thisFig(k), orientation);
      set(thisFig(k), 'PaperType', 'A4');
      print(thisFig(k), '−dpsc2', strcat('−P', whichPrinter))
      disp(sprintf('Figure %d sent to printer %s.', thisFig(k), whichPrinter))
   end
```

A.4.2 figsave.m

```
function figsave(thisFig, filename, fileformat, orientation)

   if nargin < 4
      orientation = 'landscape';
      if nargin < 3
         fileformat = 'psc2';
         if nargin < 2
            filename = input('Save figure to which file?: ', 's');
            if nargin < 1
               thisFig = gca;
            end
         end
      end
   end

   if length(thisFig) > 1
      warning('Only save of single figure supported. Using first figure given!')
   end

   orient(thisFig, orientation);
   set(thisFig, 'PaperType', 'A4');
   print(thisFig, strcat('−d', fileformat), filename)
   disp(sprintf('Figure %d saved as: %s', thisFig, filename))
```

Acknowledgements

First of all I would like to thank my supervisor Jan-Erik Wahlund for all the invaluable help he has given me during my time at the Swedish Institute of Space Physics (IRF-Uppsala): for introducing me to the subject; for letting me do the project at my own pace even though the end destination was not defined beforehand, but instead allowing the results to unfold, reshaping the path of the project and lighting the way ahead. I will also remember the fun we had during our disagreements – sometimes quite intense yet still amicable – over the way to solve certain aspects and problems that had arisen (most notably the velocity transformations during the change of reference frame, which gave rise to quite a few laughs in the end!).

I would also like to thank my assistant supervisor Ronan Modolo for guiding me through the first part of my work, and for always taking the time to answer all my questions and helping me out when Jan-Erik was away or busy. I am also grateful for his proofreading of this report, and for all his suggestions and comments on it. Merci pour toute l'aide, mon ami!

I am deeply grateful to Malin Westerberg for always being there as a friend and sounding board, helping me through this project mentally and generally brightening my day – every day! I will especially miss the time spent together during our not-so-short lunches (at weird hours) and tea breaks. I hope our friendship lasts a lifetime, and I miss you already!

Special thanks also go out to Erik Winkler – my cellmate as it were – for sharing a tiny office with me and putting up with my delirious rantings every day for nine months on every topic imaginable (as well as not, sometimes). Also, for having similar taste in music (or at least claiming to) – without which our small office would truly have been an agonising cell – and for being a good sounding board for my many crazy ideas. Cheers mate!

I also wish to thank all the personnel at IRF-U for making my time here really fun and enjoyable, with both good and bad jokes around the coffee table.

Special thanks go out to Anders Eriksson for reading through (and brutally slaughtering) my first attempt at the theory chapter on photoelectrons.

Last, but not least, I want to acknowledge all my fellow master thesis students for the time we have spent together, and for putting up a good fight and not making it easy for me to win our wiki contest! :-)

Bibliography

R. Behlke, D. Sundkvist, and A. Tjulin. *Sensors and Instruments for Space Exploration*, chapter 7. Langmuir Probes. Swedish Institute of Space Physics, Kiruna, 2 edition, 2000. Solveig H. Høymork, Editor.

L. H. Brace, W. R. Hoegy, and R. F. Theis. Solar EUV measurements at Venus based on photoelectron emission from the Pioneer Venus Langmuir probe. *J. Geophys. Res.*, 93:7282–7296, July 1988.

C. M. Cully, R. E. Ergun, and A. I. Eriksson. Electrostatic structure around spacecraft in tenuous plasmas. *J. Geophys. Res.*, in review, 2007.

E. Engwall. Cold magnetospheric plasma flows: Properties and interaction with spacecraft. Licentiate thesis, Department of Astronomy and Space Physics, Uppsala University, March 2006.

A. I. Eriksson, R. Boström, R. Gill, L. Åhlén, S.-E. Jansson, J.-E. Wahlund, M. André, A. Mälkki, J. A. Holtet, B. Lybekk, A. Pedersen, and L. G. Blomberg. RPC-LAP: The Rosetta Langmuir Probe Instrument. *Space Science Reviews*, pages 52–+, October 2006. doi: 10.1007/s11214-006-9003-3.

U. Fahleson. Theory of Electric Field Measurements conducted in the Magnetosphere with Electric Probes. *Space Science Reviews*, 7:238–262, 1967.

R. Isaksson. Solar UV (Ly-alpha) intensity from Cassini Langmuir probe data. Master's thesis, Department of Astronomy and Space Physics, Uppsala University, 2005.

K. S. Jacobsen. A Study of Low-Energy Plasma in the Inner Magnetosphere of Saturn. Master's thesis, Department of Physics, University of Oslo, 2006.

G. H. Jones, E. Roussos, N. Krupp, U. Beckmann, A. J. Coates, F. Crary, I. Dandouras, V. Dikarev, Dougherty M. K., P. Garnier, C. Hansen, A. Hansen, G. B. Hospodarsky, R. E. Johnson, S. Kempf, K. Khurana, S. M. Krimigis, H. Krüger, W. Kurth, A. Lagg, H. J. McAndrews, D. G. Mitchell, C. Paranicas, F. Postberg, C. T. Russell, J. Saur, F. Spahn, D. F. Strobel, R. Tokar, J.-E. Wahlund, R. J. Wilson, J. Woch, and D. Young. The dust halo of Saturn's largest icy moon: Evidence of rings at Rhea? *Nature*, in review, 2007.

S. W. Kieffer, X. Lu, C. M. Bethke, J. R. Spencer, S. Marshak, and A. Navrotsky. A Clathrate Reservoir Hypothesis for Enceladus' South Polar Plume. *Science*, 314:1764–, December 2006. doi: 10.1126/science.1133519.

H. Laakso, T. L. Aggson, and R. F. Pfaff, Jr. Plasma gradient effects on double-probe measurements in the magnetosphere. *Annales Geophysicae*, 13:130–146, February 1995.

H. M. Mott-Smith and I. Langmuir. The Theory of Collectors in Gaseous Discharges. *Physical Review*, 28:727–763, October 1926. doi: 10.1103/PhysRev.28.727.

J. D. Richardson. An extended plasma model for Saturn. *Geophysical Research Letters*, 22:1177–1180, May 1995.

J. R. Spencer, J. C. Pearl, M. Segura, F. M. Flasar, A. Mamoutkine, P. Romani, B. J. Buratti, A. R. Hendrix, L. J. Spilker, and R. M. C. Lopes. Cassini Encounters Enceladus: Background and the Discovery of a South Polar Hot Spot. *Science*, 311:1401–1405, March 2006. doi: 10.1126/science.1121661.

J. N. Spitale, R. A. Jacobson, C. C. Porco, and W. M. Owen, Jr. The Orbits of Saturn's Small Satellites Derived from Combined Historic and Cassini Imaging Observations. *The Astronomical Journal*, 132:692–710, August 2006. doi: 10.1086/505206.

J.-E. Wahlund, R. Boström, G. Gustafsson, D. A. Gurnett, W. S. Kurth, T. Averkamp, Hospodarsky G. B., A. M. Persoon, P. Canu, A. Pedersen, M. D. Desch, A. I. Eriksson, R. Gill, M. W. Morooka, and M. André. The inner magnetosphere of Saturn: Cassini RPWS cold plasma results from the first encounter. *Geophysical Research Letters*, 32:20–+, September 2005. doi: 10.1029/2005GL022699.

M. Westerberg. The Induced Magnetospheric Boundary at Titan. Master's thesis, Department of Astronomy and Space Physics, Uppsala University, 2007.

E. Winkler. Plasma Densities and Satellite Potentials. Master's thesis, Department of Astronomy and Space Physics, Uppsala University, 2007.